

# Dissertation

submitted to the  
Combined Faculties for the Natural Sciences and for Mathematics  
of the Ruperto-Carola University of Heidelberg, Germany  
for the degree of

**Doctor of Natural Sciences**

presented by

Martin Erich Kaiser, Master of Science  
Born in Halle/Saale  
Oral-examination: May 14th, 2018



# Formation and Modulation of Hippocampal Ensemble Activity

Referees:

Prof. Dr. Andreas Draguhn

Prof. Dr. Hilmar Bading



# Declaration of Authorship

Declarations according to § 8 (3) c) and d) of the doctoral degree regulations:

c) I hereby declare that I have written the submitted dissertation myself and in this process have used no other sources or materials than those explicitly indicated.

d) I hereby declare that I have not applied to be examined at any other institution, nor have I used the dissertation in this or any other form at any other institution as an examination paper, nor submitted it to any other faculty as a dissertation.

Heidelberg, May 17, 2018

.....  
Martin Erich Kaiser



# Acknowledgements

First and foremost, I would like to thank my thesis adviser Andreas Draguhn, who allowed me to be part of his research group. This thesis would not exist without his indispensable scientific guidance. Moreover, I would like to express my gratitude to him for being a resilient and calm leader, who feels accountable for his employees and creates a fruitful working atmosphere. Thank you!

I would like to thank my TAC members over the course of the SFB 636 graduate school. Hilmar Bading and Knut Schnell provided valuable advice, supporting me to have a smooth start into the work for this thesis. Thanks to the supportive research programs SFB 636, SFB 1134 as well as the IZN graduate school, which provided an excellent scientific environment.

During the course of this thesis, Martin Both closely supervised my scientific work. I would like to thank him for great many scientific discussions, for allowing me to take over regular personnel, project-specific and teaching responsibilities. This thesis would not have been possible without Martin's support, ideas and Matlab skills. His supervision did not only facilitate my scientific but also personal development. Thank you for being an understanding and down-to-earth supervisor.

I sincerely thank Susanne Bechtel, who is one of the most important people in the lab. Her support was vital for this thesis, helping with administrative struggles but more importantly for always having a friendly ear. Thank you Susanne!

Thanks to Pia Maier, Dimitri Hefter and my yearslong desk neighbor Pascal Geschwill. Together, we have pushed projects forward with elaborate efforts and great enthusiasm. We have spent early mornings and late evenings in the lab, doing recordings or reassembling the setup, again and again and again. Thanks for your great work, for sharing ideas and for all the scientific discussions.

Thanks to my fellow PhD students, who I have taken to my heart. I am grateful for all your support. I would like to acknowledge the "secrete nose" team. Thanks to the SFB 1134 that strongly supports young investigators, Federica Genovese, Jana Maurer, Antonio Yanez, the Master student Anna Huber and I had the chance to start a fascinating and wonderful collaboration. Thanks for your tremendous efforts and for all the bilateral motivation.

Thanks to Katja Lankisch, Nadine Zuber and Tina Sackmann for basically keeping the lab running, taking care of drug solutions, mice, viral injections and for openly sharing their wide experience in different techniques. Katja, Nadine and Tina, this thesis would not be that comprehensive without you. Thank you!

I would like to thank Lucie Landeck, who I had the change to supervise during her first months in lab. Her fascination and dedication for science acted as a catalyst, helping me to mobilize the reserves during the last months of my PhD. Thanks for being a marvelous colleague and for becoming a friend!

I am truly grateful for all the amazing colleagues in the Draguhn lab. I feel humbled to have worked with all of you over the last years. Thank you for everything! Without you, this PhD journey would not have been possible.

I would also like to acknowledge my colleagues from other research groups. Thanks to Shehabeldin Elzoheiry for great many discussion about and beyond science. My sincere thanks to Christina Mayer, Simone Schilling and Jan-Oliver Hollnagel who not only became close colleagues but also unique friends. Thanks for your vital support and for enriching this PhD experience. To quote Andrew Gold: "Your heart is true and you're a pal and a confidant. [...] I hope it always will stay this way. [...] Thank you for being a friend."

Generally, I would like to thank all my dear friends for so many things that enriched this experience - to just name a few, thanks for the relaxing wine and cooking evenings, for the heated debates about economics, politics and sociology, for riding the emotional rollercoaster during football games, for laughing about nonsense and for understanding my continuous absence during examination periods at the Fernuni.

Finally, thanks to my family, who encouraged me to leave a small village in Eastern Germany to follow my interests and drive. Thanks for your indulgent support. Particularly, I would like to thank my virtually half brother Daniel Helbig, who has been more than just a friend since my early childhood. A special thanks is due to my mother for her unquestionable support and for always believing in me. This thesis would not have been possible without you, not even to the slightest. Thank you mom!



*What I must stress here is that the brain's understanding of anything, whether factual or abstract, arises from our manipulations of the external world, by our moving within the world and thus from our sensory-derived experience of it.*

— Rodolfo Llinas



## Abstract

The extent to which advanced organisms can grasp and learn complex environmental patterns represents a fascinating feature. It is believed that memory is encoded by transiently co-active cells, so called neuronal ensembles, in which cells are temporally linked by underlying network oscillations. In the hippocampus, rhythms of oscillating neuronal networks are directly associated with behavioral states. For instance, gamma rhythms are linked to memory formation, whereas intermittent sharp wave-ripple oscillations are involved in memory consolidation.

During coordinated neuronal ensemble activity participating cells are selectively activated although they are scattered throughout neuronal tissue. This spatiotemporal specificity requires dynamic anatomical and physiological working principles. In this work, we aimed for a deeper understanding of the apparent complexity underlying neuronal ensemble formation. We studied the recruitment of single cells into neuronal ensembles during sharp wave-ripple oscillations *in vitro*. In our approach, we combined recent physiological and anatomical evidence about hippocampal principal cells. On the one hand, a subpopulation of principal cells elicits network-entrained action potentials that exhibit a characteristic ectopic waveform *in vitro*. On the other hand, a large number of cells feature a peculiar axon location. We discovered a relationship between these two findings, showing that only cells with axons originating from a dendrite were able to participate during sharp wave-ripple oscillations.

As specific network oscillations are associated with different behavioral states, we were interested in the modulation of network rhythms. It has been shown that enhanced levels of oxytocin affect the formation of long-lasting spatial memory. Here, we studied the effects of oxytocin on hippocampal network activity *in vitro*, showing that it selectively reduced sharp wave-ripples, while failing to modulate gamma oscillations.

Furthermore, we investigated the neuroprotective mechanism, which is enabled by the amyloid precursor protein. Although being strongly associated with Alzheimer's disease, its intracellular processing provides a basis for neuroprotection. We show that the harming impact of a hypoxic condition on hippocampal network oscillations was eased by fragments of the amyloid precursor protein through modulation of L-type calcium channels, *in vitro*.



## Zusammenfassung

Es ist eine faszinierende Besonderheit, in welchem Ausmaß hoch entwickelte Lebewesen in der Lage sind, komplexe Umweltstrukturen zu erfassen und zu erlernen. Aktuelle Erkenntnisse gehen davon aus, dass Gedächtnisinhalte von vorübergehend koaktiven Nervenzellen kodiert werden. In derartigen neuronalen Ensembles wird die Aktivität einzelner Zellen durch zugrundeliegende Netzwerkoszillationen kurzzeitig aufeinander abgestimmt. Im Hippokampus werden Rhythmen oszillierender Netzwerke direkt mit verschiedenen Verhaltenszuständen in Verbindung gebracht. Gamma-Oszillationen werden zum Beispiel mit der Generierung von Gedächtnisinhalten assoziiert, während sporadische Sharp-Wave-Ripple-Oszillationen bei der Gedächtniskonsolidierung eine wichtige Rolle spielen.

Während neuronaler Ensemble-Aktivität werden teilnehmende Zellen selektiv aktiviert, obwohl sie verstreut im neuronalen Gewebe liegen. Eine derartige räumliche als auch zeitliche Spezifität erfordert dynamische Funktionsmechanismen. Ziel dieser Dissertation war es unter anderem, die Komplexität der Ausbildung funktioneller neuronaler Ensembles anhand spontaner Sharp-Wave-Ripple-Oszillationen *in vitro* näher zu verstehen. Dabei kombinierten wir jüngste physiologische und anatomische Erkenntnisse über hippokampale Zellen. Einerseits sind Aktionspotentiale mit einer ektopischen Wellenform in einigen Zellen beobachtbar, andererseits weist eine Subpopulation von Neuronen eine eigenartige Positionierung des Axons auf. Wir konnten einen Zusammenhang zwischen beiden Beobachtungen herstellen. Einzig Zellen, deren Axone an einem Dendriten entspringen, waren in der Lage, an Sharp-Wave-Ripple-Oszillationen teilzunehmen.

Da hippokampale Netzwerkzustände mit spezifischen Verhaltensmustern assoziiert sind, untersuchten wir weiterhin die Modulation neuronaler Oszillationen. Es ist bekannt, dass Oxytocin die Bildung des räumlichen Langzeitgedächtnisses beeinflusst. Wir untersuchten deshalb den Effekt von Oxytocin auf hippokampale Netzwerkaktivitäten und konnten zeigen, dass Oxytocin Sharp-Wave-Ripple-Oszillationen selektiv dämpft, Gamma-Oszillationen dagegen nicht beeinflusst.

Weiterhin untersuchten wir einen neuroprotektiven Mechanismus, der auf dem Amyloid-Vorläuferprotein basiert. Dieses Protein wird zwar mit der Entwicklung von Alzheimer in Verbindung gebracht, allerdings bietet dessen intrazelluläre Prozessierung auch die Grundlage für Neuroprotektion. In dieser Arbeit konnten wir zeigen, dass ein Fragment des Amyloid-Vorläuferproteins schädigende Einflüsse von Sauerstoffmangel auf hippokampale Netzwerkoszillationen durch die Beeinflussung von L-Typ-Kalziumkanälen mindert.



# Contents

|   |             |
|---|-------------|
| <b>List of Figures</b>  | <b>XIII</b> |
| <b>List of Tables</b>   | <b>XIV</b>  |
| <b>List of Abbreviations</b>  | <b>XVII</b> |
| <b>1 Introduction</b>   | <b>1</b>    |
| 1.1 The Hippocampal Formation and Its Proposed Role in Memory . . . . .   | 1           |
| 1.1.1 Anatomy and Circuitry . . . . .   | 1           |
| 1.1.2 A Spatial Map in the Hippocampus . . . . .  | 3           |
| 1.2 Axon Initial Segment - The Action Potential Initiation Zone . . . . .   | 4           |
| 1.2.1 Structure and Function . . . . .  | 4           |
| 1.2.2 Plasticity and Location . . . . .   | 6           |
| 1.3 Hippocampal Network Oscillations . . . . .  | 7           |
| 1.3.1 Theta Rhythms ( $\sim 4\text{-}12\text{Hz}$ ) . . . . .   | 8           |
| 1.3.2 Gamma Rhythms ( $\sim 25\text{-}150\text{Hz}$ ) . . . . .   | 9           |
| 1.3.3 Sharp Wave-Ripple Oscillations ( $\sim 0.01\text{-}3\text{ Hz}$ / $\sim 110\text{-}250\text{ Hz}$ ) . . . . . | 11          |
| 1.4 The Potential of Endogenous Factors to Modulate and Protect Neuronal<br>Networks . . . . .                      | 16          |
| 1.4.1 The Hypothalamic Neuropeptide Oxytocin . . . . .  | 16          |
| 1.4.2 Amyloid Precursor Protein - A Fine Line Between Neurotoxicity and<br>Neuroprotection . . . . .                | 18          |
| <b>2 Aims of the Study</b>  | <b>21</b>   |
| <b>3 Materials and Methods</b>  | <b>23</b>   |
| 3.1 Applied Drugs . . . . .   | 23          |
| 3.2 Animal Handling and Slice Preparation . . . . .   | 24          |

|          |   |           |
|----------|---|-----------|
| 3.3      | Electrophysiology . . . . .   | 24        |
| 3.3.1    | Standard Local Field Potential Recordings . . . . .   | 24        |
| 3.3.2    | Single Cell Sharp Electrode Intracellular Recordings . . . . .  | 25        |
| 3.3.3    | Conductance Analysis and Statistics . . . . .   | 26        |
| 3.3.4    | Implementation of a Dynamic Clamp System . . . . .  | 29        |
| 3.3.5    | Microelectrode Array Recordings . . . . .   | 31        |
| 3.4      | Intracranial Injections of Viral Vectors . . . . .  | 32        |
| 3.5      | Illumination and Microscopy . . . . .   | 34        |
| 3.5.1    | Implementation of a Holographic Illumination and Imaging System   | 34        |
| 3.5.2    | Immunocytochemistry and Confocal Imaging . . . . .  | 36        |
| 3.5.3    | Calcium Imaging . . . . .   | 37        |
| <b>4</b> | <b>Results</b>  | <b>41</b> |
| 4.1      | Privileged Recruitment of AcD Pyramidal Cells in CA1 during SPW-Rs <i>in vitro</i> . . . . .                                | 41        |
| 4.1.1    | SPW-R-Entrained Spiking Behavior Correlated to Cellular Anatomy   | 41        |
| 4.1.2    | A Working Hypothesis for Selective Network-Entrained Pyramidal Cell Activation, Based on the Position of the Axon . . . . . | 54        |
| 4.1.3    | Reduction of Perisomatic Inhibition Turned Silent Pyramidal Cells Into Participating Ones . . . . .                         | 56        |
| 4.2      | Differential Modulation of Hippocampal Network Oscillations by Oxytocin <i>in vitro</i> . . . . .                           | 67        |
| 4.2.1    | Oxytocin Receptor Activation Resulted in Reduced SPW-R Oscillations . . . . .   | 67        |
| 4.2.2    | Oxytocin Receptor Activation Did Not Modulate Gamma Oscillations  | 71        |
| 4.3      | Amyloid Precursor Protein Protected Neuronal Networks against Hypoxia <i>in vitro</i> . . . . .                             | 78        |
| 4.3.1    | Block of L-type Calcium Channels Alleviated Posthypoxic Deficits in APP <sup>-/-</sup> Mice . . . . .                       | 78        |
| <b>5</b> | <b>Discussion</b>   | <b>83</b> |
| 5.1      | Selective Recruitment of CA1 Pyramidal Cells into SPW-R-Ensembles <i>in vitro</i> . . . . .                                 | 84        |
| 5.1.1    | Axon-Carrying Dendrite Cells Were Preferentially Recruited into SPW-R Oscillations . . . . .                                | 84        |



|          |   |            |
|----------|---|------------|
| 5.1.2    | Cellular Anatomy and Incident Perisomatic Inhibition Shaped Defined CA1 Pyramidal Cell Recruitment into Ensemble Activity . . . | 87         |
| 5.1.3    | Functional Consequences for the Information Processing in the Hippocampus . . . . .   | 89         |
| 5.1.4    | Potential Impact of the <i>in vitro</i> Condition on Observed Spiking Pyramidal Cells Behaviors . . . . .                       | 91         |
| 5.2      | Selective Neuromodulatory Effects of Oxytocin on Hippocampal Network Oscillations <i>in vitro</i> . . . . .                     | 92         |
| 5.2.1    | Oxytocin Receptor Activation Affected Spontaneous SPW-Rs . . .  | 92         |
| 5.2.2    | Oxytocin Receptor Activation Spared Induced Gamma Oscillations  | 94         |
| 5.3      | Neuroprotection by Amyloid Precursor Protein during Hypoxic Stress . . .  | 96         |
| 5.3.1    | Soluble Amyloid Precursor Protein Alpha Exerted a Neuroprotective Role through L-Type Calcium Channels . . . . .                | 96         |
| <b>6</b> | <b>Outlook</b>  | <b>98</b>  |
|          | <b>References</b>   | <b>103</b> |
|          | <b>List of Publications</b>   | <b>135</b> |



# List of Figures

|     |  |    |
|-----|--|----|
| 1.1 | Scheme of the rodent hippocampal formation and a representative CA1 pyramidal cell. . . . .  | 2  |
| 1.2 | Schematic field potentials of theta (black) and gamma (orange) rhythms in the hippocampus. . . . .   | 7  |
| 1.3 | Example <i>in vitro</i> sharp-wave ripple. . . . .   | 11 |
| 1.4 | Scheme of proposed models for hippocampal ripple generation mechanisms in CA1. . . . .   | 13 |
| 1.5 | Scheme of amyloid precursor protein metabolism. . . . .  | 18 |
| 3.1 | Example pyramidal cell recording during SPW-Rs and corresponding conductance changes. . . . .  | 26 |
| 3.2 | Scheme of the dynamic clamp recording principle. . . . .   | 30 |
| 3.3 | Scheme of the microelectrode array perfusion system. . . . .   | 31 |
| 3.4 | Cranial injections yielded consistent viral expression . . . . .   | 32 |
| 3.5 | Scheme of the holographic illumination and imaging system. . . . .   | 35 |
| 4.1 | Representative network-entrained spiking of a single CA1 pyramidal cell during SPW-R oscillations. . . . .                                     | 43 |
| 4.2 | Representative network-entrained hyperpolarization of a single CA1 pyramidal cell during SPW-R oscillations. . . . .                           | 44 |
| 4.3 | CA1 pyramidal cells constituted two distinct anatomical groups. . . . .  | 45 |
| 4.4 | Axon location indicated the SPW-R-entrained spiking behavior of targeted CA1 pyramidal cells. . . . .  | 46 |
| 4.5 | AcD and nonAcD CA1 pyramidal cells received similar SPW-R-entrained peak conductance inputs but at different peak excitation times. . . . .    | 48 |
| 4.6 | AcD and nonAcD CA1 pyramidal cells received similar SPW-R-entrained conductance time courses but with different inhibitory rise times. . . . . | 49 |

|      |   |    |
|------|---|----|
| 4.7  | AcD and nonAcD CA1 pyramidal cells received similar sharp wave- and ripple-entrained inputs. . . . .  | 51 |
| 4.8  | Working hypothesis for the selective AcD cell activation during hippocampal SPW-R oscillations. . . . .   | 55 |
| 4.9  | Intracellular application of picrotoxin (1mM) reduced the peak of SPW-R-entrained inhibitory conductance changes of CA1 pyramidal cells. . . . .      | 58 |
| 4.10 | Intracellular application of picrotoxin (1mM) diminished sharp wave- and ripple-entrained inhibitory conductances. . . . .                            | 59 |
| 4.11 | Intracellular application of picrotoxin (1mM) resulted in spontaneous firing of canonical APs of nonAcD CA1 pyramidal cells during SPW-Rs. . . . .    | 62 |
| 4.12 | Counteracting phasic inhibition with dynamic clamp resulted in canonical APs during SPW-Rs. . . . .   | 64 |
| 4.13 | Oxytocin receptor activation decreased SPW-R oscillations. . . . .  | 70 |
| 4.14 | TGOT marginally affected pharmacologically induced gamma oscillations. . . . .  | 73 |
| 4.15 | Oxytocin receptor activation left light-induced nested gamma oscillations unchanged. . . . .  | 76 |
| 4.16 | Increased calcium influx through LTCC reduced latency to hypoxia-induced spreading depression in APP <sup>-/-</sup> hippocampal brain slices. . . . . | 79 |

# List of Tables

|     |   |    |
|-----|---|----|
| 3.1 | <i>List of applied drugs</i> . . . . .                                    | 23 |
| 4.1 | SPW-R-entrained conductance features under baseline conditions . . . . .  | 52 |
| 4.2 | SPW-R-entrained conductance features during picrotoxin dialysis . . . . . | 60 |



# List of Abbreviations

|                   |  |
|-------------------|--|
| CA1               | Cornu Ammonis 1  |
| DG                | Dentate Gyrus  |
| HIL               | Hilus  |
| CA3               | Cornu Ammonis 3  |
| PV                | Parvalbumin  |
| HCN               | Hyperpolarization-activated cyclic nucleotide  |
| SPW-R             | Sharp wave-ripple complex  |
| EC                | Entorhinal Cortex  |
| sc                | Schaffer collaterals   |
| mf                | Mossy fibers   |
| REM               | Rapid eye movement   |
| GABA <sub>A</sub> | $\gamma$ -aminobutyric acid A  |
| AVP               | Arginine-vasopressin receptors   |
| OTRA              | DesGly-NH <sub>2</sub> -d(CH <sub>2</sub> ) <sub>5</sub> -[D-Tyr <sup>2</sup> , Thr <sup>4</sup> ]OVT            |
| V1ARA             | [Phenylacetyl <sup>1</sup> , O-Me-D-Tyr <sup>2</sup> , Arg <sup>6,8</sup> , Lys <sup>9</sup> ]-Vasopressin amide |
| MEA               | Microelectrode Array   |
| mAChR             | Acetylcholine receptors  |
| SLM               | Spatial light modulator  |

|                 |  |
|-----------------|--|
| ChR2            | Channelrhodopsin   |
| eYFP            | Enhanced yellow fluorescent protein  |
| AP              | Action potential   |
| ACSF            | Artificial cerebrospinal fluid   |
| PTX             | Picrotoxin   |
| DAPI            | 4',6-Diamidin-2-phenylindol  |
| FSI             | Fast-spiking interneurons  |
| OR              | Oxytocin receptor  |
| LTP             | Long-term potentiation   |
| LTCCs           | L-type voltage gated calcium channels  |
| NMDA            | N-methyl-D-aspartate   |
| WT              | Wild-type  |
| APV             | Antagonist D(-)-2-Amino-5-phosphonopentanoic acid  |
| Carbachol       | Carbamoylcholine chloride  |
| Kainate         | (2S,3S,4S)-Carboxy-4-(1-methylethenyl)-3-pyrrolidineacetic acid                                      |
| L-glutamic acid | L-Glutamic acid monosodium salt hydrate  |
| TGOT            | (Thr <sup>4</sup> ,Gly <sup>7</sup> )-Oxytocin H-Cys-Tyr-Ile-Thr-Asn-Cys-Gly-Leu-Gly-NH <sub>2</sub> |
| Vasopressin     | (Arg <sup>8</sup> )-Vasopressin (H-Cys-Tyr-Phe-Gln-Asn-Cys-Pro-Arg-Gly-NH <sub>2</sub>               |
| PFA             | Paraformaldehyde   |
| PBS             | Phosphate buffered saline  |
| OGB-1           | Oregon Green BAPTA 1-AM  |
| ROI             | Region of interest   |
| DNA             | Deoxyribonucleic acid  |



|                         |  |
|-------------------------|--|
| LCOS                    | Liquid crystals on silicon                                   |
| $g_{\text{excitatory}}$ | Excitatory conductance                                       |
| $g_{\text{inhibitory}}$ | Inhibitory conductance                                       |
| $g_{\text{synaptic}}$   | Synaptic conductance   |
| R                       | Electrical resistance  |
| $I_{\text{total}}$      | Total current flow across the membrane                       |
| $E_{\text{synaptic}}$   | Synaptic reversal potential                                  |
| $E_{\text{excitatory}}$ | Excitatory reversal potential                                |
| $E_{\text{inhibitory}}$ | Inhibitory reversal potential                                |
| $R_{\text{Input}}$      | Input resistance   |
| $V_{\text{measured}}$   | Measured voltage response                                    |
| $I_{\text{injected}}$   | Injected current   |
| NMDA                    | N-methyl-D-aspartate   |
| AMPA                    | $\alpha$ -amino-3-hydroxy-5-methyl-4-isoxazolepropionic acid |
| $A\beta$                | Amyloid- $\beta$   |
| APPs                    | Soluble amyloid precursor protein                            |
| APP                     | Amyloid precursor protein                                    |
| P3                      | P3 peptide   |



# 1 Introduction

## 1.1 The Hippocampal Formation and Its Proposed Role in Memory

### 1.1.1 Anatomy and Circuitry

The *hippocampal formation* is thought to be pivotal for spatial as well as declarative memory (Buzsaki, 1986; Csicsvari and Dupret, 2014; Ego-Stengel and Wilson, 2010; Kali and Dayan, 2004). Moreover, it is well known for its behavioral state-dependent neural oscillations (Buzsaki et al., 1983; O’Keefe, 1976; O’Keefe and Recce, 1993). Thus, it represents an ideal model system to complement current knowledge about mechanistic principles of brain rhythms.

As part of the archicortex, the mammalian hippocampal formation lies within the medial temporal lobe, bilaterally protruding into the lateral ventricles and belonging to the limbic system of the brain. The origin of the name lies in the structural similarities between the common seahorse (*hippocampus*) and the cerebral formation. The hippocampal formation comprises the dentate gyrus (DG), hippocampus proper, subiculum (Sub), presubiculum, parasubiculum and the entorhinal cortex (EC), as seen in figure 1.1 A.

The *hippocampus proper*, also simply called *hippocampus*, is a sub-area of the hip-

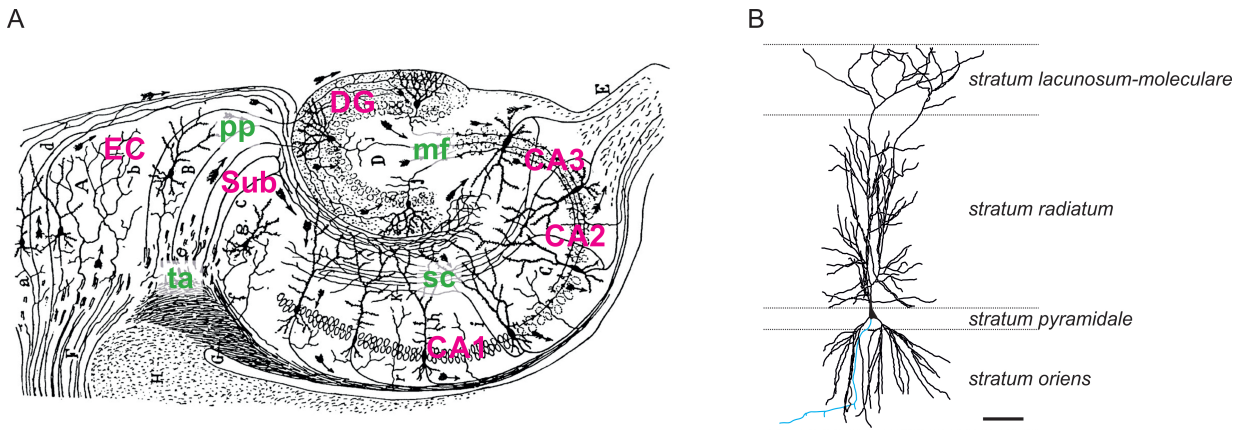


**Figure 1.1: Scheme of the rodent hippocampal formation and a representative CA1 pyramidal cell.**

**A. Drawing of the rodent hippocampal formation:** As indicated in rose, the hippocampal formation consists of the larger areas DG, CA3, CA2, CA1, Sub and EC. The EC projects to CA1 via the *temporoammonic pathway* (*ta*) and to the DG via the *perforant path* (*pp*). The DG provides inputs to CA3 through *mossy fibers* (*mf*). The CA1 region resembles the main output region of the hippocampus proper, receiving most of the excitatory inputs from CA3 via the *Schaffer collaterals* (*sc*). Adapted from Amaral et al. (2007), original drawing from Santiago Ramon y Cajal in *Histologie de Système Nerveux* from 1911. **B. CA1 pyramidal cell and indicated hippocampal layers.** Basal dendrites branch from the soma inside *stratum pyramidale* into *stratum oriens*. For the most part, Schaffer collaterals target apical dendrites in the *stratum radiatum*, albeit also reaching apical CA1 dendrites through the *stratum lacunosum-moleculare*, together with EC inputs. The axon is indicated in blue. Scale bar = 100  $\mu\text{m}$ . Adapted from Ishizuka et al. (1995).

hippocampal formation. Due to its macroscopic shape, ancient scholars coined the hippocampus *cornu ammonis*, which is Latin for horn of the ram. Thus, it is divided into the cornu ammonis (CA) regions CA3, CA2 and CA1 (figure 1.1 A). Evolutionary, the main structure and fiber connections of the hippocampus are preserved across mammals. The EC projects axons to the DG forming the perforant path (figure 1.1 A). CA3 receives three main excitatory inputs. Most prominently DG cells project their axons to CA3, forming the *mossy fibers* (figure, 1.1 A; Blackstad et al. 1970; Swanson et al. 1978). EC layer II neurons (Witter, 1993) as well as recurrent collateral CA3 inputs also target the CA3 region (Amaral and Lavenex, 2007). Due to its extensive recurrent connections CA3 is considered as an autoassociation network for pattern completion (Rolls, 1996, 2013).

CA1 on the other hand receives most of the excitatory input to basal and apical den-

### 1.1 The Hippocampal Formation and Its Proposed Role in Memory

drites via the *Schaffer collaterals* (sc; figure 1.1 A). Further, layer III medial EC neurons also provide excitatory inputs to CA1 through the *temporoammonic pathway* (ta; figure 1.1 A; Doller and Weight 1982), resembling the CA1-EC loop of information processing (Amaral and Witter, 1989; Witter et al., 2000). The hippocampal CA1 region represents the main output area of the hippocampus, playing a crucial role in the retrieval of context-dependent memory (Ji and Maren, 2008) as well as in the detection of novel environmental features (Fyhn et al., 2002; Hasselmo and Schnell, 1994; Lee et al., 2004).

The *hippocampus* is a layered structure (figure 1.1 B), in which principal cell somata are condensed into a single layer, called the *stratum pyramidale*. It comprises somata of pyramidal cells and inhibitory interneurons. However, interneurons of several subtypes are found in each hippocampal layer (Klausberger and Somogyi, 2008). In the CA sub-areas, basal dendrites from pyramidal cells reach into the *stratum oriens*, the deeper layer of the hippocampus. In the *stratum radiatum* bundled CA3 pyramidal cell axons, called Schaffer collateral fibers, project onto CA1 apical dendrites. In CA3 only, *stratum lucidum* is positioned between strata pyramidale and radiatum, containing mossy fibers from the DG. In the more superficial hippocampal layers, fibers from EC cells reach distal CA apical dendrites through *stratum lacunosum-moleculare* (figure 1.1 B; Amaral and Witter 1989; Witter et al. 2000).

In the hippocampal formation neurons are highly plastic and well interconnected, to allow integration of multimodal sensory information from the neocortex. According to a prominent model, the unidirectional flow of information partly follows the so-called trisynaptic loop (EC  $\xrightarrow{1.}$  DG  $\xrightarrow{2.}$  CA3  $\xrightarrow{3.}$  CA1; Amaral and Witter 1989; Andersen et al. 1971).

#### 1.1.2 A Spatial Map in the Hippocampus

As a structure of interest, the hippocampal formation caught the particular attention of scientists in the late 1950s. In the course of an epilepsy treatment, parts of the medial temporal lobe were surgically removed from patient H.M, who suffered from memory con-

## 1 INTRODUCTION

solidation deficits as a consequences. This indicated an essential role of the hippocampal formation in learning and memory.

The potential role of the hippocampus in memory was expanded by György Buzsáki. He postulated a consecutive "*two-stage model of memory trace formation*" (Buzsaki, 1989). Accordingly, in exploring animals, inputs to the hippocampus lead to differentiating synaptic potentiation, which results in specific neuronal activity and hence memory formation. Indeed, *in vivo* single cell recordings in rodents provided experimental evidence for a selective activation of individual pyramidal cells, depending on the local position of the respective animal (O'Keefe and Dostrovsky, 1971; Yartsev and Ulanovsky, 2013). These principal cells are therefore called *place cells* (O'Keefe, 1976). During immobility or slow wave sleep, these place cells are then reactivated, which leads to the consolidation of previously formed memory traces. Consequently, it is suggested that the hippocampus forms a cognitive map, rendering it to be an essential structure for spatial mapping (O'Keefe and Dostrovsky, 1971; O'Keefe and Nadel, 1978).

## 1.2 Axon Initial Segment - The Action Potential Initiation Zone

### 1.2.1 Structure and Function

In neurons, the axon initial segment (AIS) represents the key excitable domain that orchestrates AP initiation, propagation, and backpropagation. As part of the axon, it forms a 20-70  $\mu\text{m}$  unmyelinated and heterogeneous microdomain that separates the somatic from the axonal compartment (Clark et al., 2005; Palmer and Stuart, 2006; Peters et al., 1968). The AIS enables a rapid and defined membrane depolarization via expression of a variety of transient and persistent voltage-gated ion channels (Hodgkin and Huxley, 1952; Kole and Stuart, 2012). In general, APs are preferentially elicited at the distal AIS,

## 1.2 Axon Initial Segment - The Action Potential Initiation Zone

due to low-threshold sodium channels. (Meeks and Mennerick, 2007; Palmer and Stuart, 2006; Schmidt-Hieber et al., 2008).

Multiple sodium and potassium channels are expressed at the AIS, which are essential for axonal and thus cellular excitability. Experiments suggest that the AP voltage threshold is lower in the axon than at other neuronal structures, which enables a reliable AP generation (Kole and Stuart, 2008). Consequently, overall sodium channel density is found to be highest at the AIS in comparison to other neuronal compartments. The precise ratio is proposed to range from 5- to 40-fold, but is still under debate (Fleidervish et al., 2010; Kole and Stuart, 2008; Lorincz and Nusser, 2010; Schmidt-Hieber and Bischofberger, 2010).

Along the AIS there are multiple subtypes of sodium channel subunits ( $\text{Na}_v$ ). They vary with respect to localization, electrophysiological kinetic and activation properties. Hence, they fulfill distinct roles in AP generation. The subtype composition and positioning of ion conductances along the AIS has been shown to vary with cell type and age (Lorincz and Nusser, 2008). The two major sodium channel subtypes are  $\text{Na}_v1.2$  and  $\text{Na}_v1.6$ .  $\text{Na}_v1.2$  channels are positioned at the proximal end of pyramidal cells' AIS. Their biophysical properties facilitate AP backpropagation into the soma and dendrites.  $\text{Na}_v1.6$  conductances on the other hand are primarily expressed at the distal end of the AIS. They show a lowered activation voltage as compared to  $\text{Na}_v1.2$  channels and are crucial for initiation and orthodromic AP propagation (Hu et al., 2009).

Different subtypes of potassium channel subunits ( $\text{K}_v$ ) play an essential role in regulating the axonal voltage threshold and AP properties in the AIS (Alle and Geiger, 2006; Geiger and Jonas, 2000). Briefly,  $\text{K}_v1$  conductances at the distal AIS shape the axonal spike width (Kole et al., 2007; Shu et al., 2007), whereas axonal excitability is modulated by  $\text{K}_v7.2$  and  $\text{K}_v7.3$  (Johnston et al., 2010). They are the mediators of the so-called M-current, which lowers the spike threshold of the axon. However, some potassium channel types are less restricted to the AIS, like  $\text{K}_v3.1$  (Elezgarai et al., 2003; Wang et al., 1998).

Most ion channels are anchored to the AIS by the two co-localizing scaffolding proteins ankyrin-G and  $\beta$ -IV-spectrin. Both are commonly used as marker proteins for the AIS.

The expression of Ankyrin-G and  $\beta$ -IV-spectrin is restricted to the AIS as well as nodes of Ranvier (Kole and Stuart, 2012; Kordeli et al., 1995). They link the cellular cytoskeleton and the membrane proteins (Yang et al., 2007). Ankyrin-G fulfills a vital role in the AIS development whereas  $\beta$ -IV-spectrin is thought to be important for AIS maintenance and stabilization (Hedstrom et al., 2007; Ogawa and Rasband, 2008). Animals lacking  $\beta$ -IV-spectrin showed mislocalization of sodium channels (Komada and Soriano, 2002).

### 1.2.2 Plasticity and Location

The shape and location of the AIS is not as rigid as previously thought. Ion channels are not strictly fixed in the AIS (Kuba et al., 2014). Exceeding or deprived stimulation of neurons results in a translocation of sodium channels. Thereby, respective shortening (Grubb and Burrone, 2010) or distal shifting (Kuba et al., 2010, 2015) of the AIS modulates neuronal excitability. While abundant stimulation increases the AP initiation threshold, diminution of synaptic input reduces it (Grubb and Burrone, 2010; Kuba et al., 2014, 2010). In addition, the AIS is targeted by inhibitory interneurons, which control AP initiation and backpropagation (Zhu et al., 2004). Activity dependent adaption of the AIS are assumed to exhibit a homeostatic mechanism, sustaining the intrinsic excitability of a neuron. Although still largely unknown, AIS plasticity mechanisms are assumed to rely on intracellular calcium entry (Grubb et al., 2011).

Recent evidence shows a heterogeneity in the axon and thereby also AIS positioning. Apart from the somatic origin, axons can also derive from neuronal dendrites, being observed in neuroendocrine cells (Herde et al., 2013), dopaminergic substantia nigra neurons (Hausser et al., 1995), interneurons (Martina et al., 2000), neocortical pyramidal cells (Lorincz and Nusser, 2008) as well as hippocampal principal neurons (Thome et al., 2014). In the hippocampal area CA1, axons of approximately 50 % of pyramidal cells emerge from a basal dendrite instead of the soma. Synaptic inputs to these axon-carrying dendrites result in greater excitation than to non-axon-carrying dendrites (Thome et al., 2014). Moreover, due to the dendritic location of the axon, respective cells exhibit synaptic integration in



dendritic compartments, rather than in the soma. Taken together, published data ascribe a privileged role to axon-carrying branches with respect to input processing in the such cells (Hausser et al., 1995; Thome et al., 2014).

### 1.3 Hippocampal Network Oscillations

Memory processes involve the coordinated activity of distributed cells, forming so called neuronal ensembles (Hebb, 1949). Their information content is suggested to be defined by the activity pattern of participating cells (Nakajima et al., 1986; O’Keefe, 1976; Vandecasteele et al., 2014). To achieve synchrony, neuronal rhythms are thought to provide a temporal framework for ensemble activities, organizing the order of spiking within an ensemble (Buzsaki and Draguhn, 2004; Engel et al., 2001).

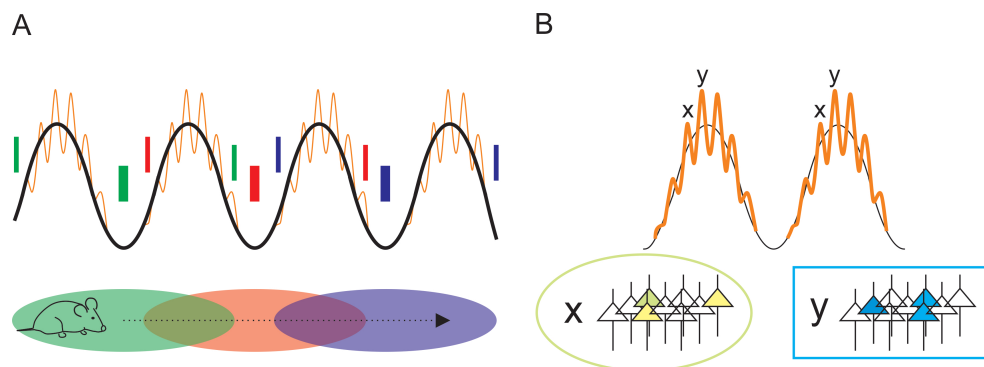


**Figure 1.2: Schematic field potentials of theta (black) and gamma (orange) rhythms in the hippocampus.**

**A. Scheme of place cell firing during locomotion.** Place fields and place cell spikes are illustrated in corresponding colors. Place cell activity is precisely locked to theta, whereby the rate of AP firing increases until the center is reached, as the animal traverses a place field. Peak firing emerges at the theta trough and indicates the center of the place field. **B. Scheme of interactions between theta and gamma oscillations.** Memory representations are illustrated as the ensembles x and y. They are activated with each theta cycle, precisely timed by gamma. Adapted from Jensen and Colgin (2007)

Thus, such rhythms are postulated to provide an indispensable temporal framework for information processing and transfer (Klausberger and Somogyi, 2008; Salinas and Sejnowski,

2001). Hippocampal network oscillations include *theta rhythms* ( $\sim 4\text{-}12$  Hz; Vanderwolf 1969), *gamma rhythms* ( $\sim 25\text{-}150$  Hz; Bragin et al. 1995; Lasztoczi and Klausberger 2017) and *sharp wave-ripple complexes* ( $\sim 0.01\text{-}3$  Hz sharp waves with  $\sim 110\text{-}250$  Hz superimposed ripples; Buzsaki 1986).

### 1.3.1 Theta Rhythms ( $\sim 4\text{-}12\text{Hz}$ )

*Theta* oscillations occur during active exploration, locomotion and rapid eye movement (REM) sleep (figure 1.2 A; Vanderwolf 1969). Hippocampal *theta* oscillations are maintained by cholinergic medial septum input (Yoder and Pang, 2005), which is thought to provide excitation as well as to antagonize other types of oscillations, such as sharp wave-ripple complexes (SPW-Rs) (Nakajima et al., 1986; Vandecasteele et al., 2014). *Theta* oscillations enable a defined order of principal cell firing (Feng et al., 2015; Wang et al., 2015).

Mechanistically, *theta* is generated through rhythmic inhibition of hippocampal inhibitory interneurons by parvalbumin-positive ( $PV^+$ ) pacemaking interneurons in the medial septum (Freund and Antal, 1988). The fluctuating suppression of inhibition in turn disinhibits pyramidal cells temporally (Freund and Antal, 1988). Thereby, the firing of hippocampal interneurons as well as pyramidal cells are phase-locked to distinct phases of the *theta* cycle (Somogyi et al., 2014). As the animal transverses through a place field, hippocampal  $PV^+$  interneurons rhythmically inhibit and thereby synchronize place cell firing (Varga et al., 2012). Thereby, a place cell elicits APs to earlier phases of the *theta* cycle, while the animal passes its respective place field (figure 1.2 A; O’Keefe and Recce 1993; Skaggs et al. 1996).

Additionally, intrinsic resonance properties of hippocampal pyramidal cells contribute to *theta* generation. Subthreshold oscillations are established by slow voltage-gated cationic currents through potassium and hyperpolarization-activated cyclic nucleotide-gated (HCN) channels, called M- and h-current, respectively (Hu et al., 2002). Together with local interneuron characteristics, these cationic currents lead to the generation of hippocampal

*theta* oscillations without septal inputs *in vitro* (Goutagny et al., 2009). However, *in vivo* hippocampal *theta* rhythms are accompanied by septal inputs (Mizumori et al., 1990).

#### 1.3.2 Gamma Rhythms ( $\sim 25\text{-}150\text{Hz}$ )

*In vivo*, *gamma* oscillations occur during multiple behavioral states, showing a broad range of frequencies. Conceptually, they are thought to provide a binding mechanism, synchronizing distributed cells into ensembles, with a millisecond range precision (Buzsaki and Draguhn, 2004). Gamma are nested in *theta* oscillations and thereby modulated by the respective *theta* rhythms (figure 1.2 B).

Evidence suggests that there are functionally different types of *gamma* oscillations, depending on the frequency (Bieri et al., 2014; Lasztoczi and Klausberger, 2014). An illustrating scheme is depicted in figure 1.2 B. Frequencies in the range of  $\sim 25\text{-}50$  Hz were termed *slow gamma*, while frequencies in the range  $\sim 65\text{-}150$  Hz have been named *fast gamma* (Colgin et al., 2009). *Slow* and *fast gamma* are thought to foster synchronization between distinct brain regions (Womelsdorf et al., 2007), separating competing inputs to the hippocampus, depending on the animal's behavior (Bieri et al., 2014). *Slow* and *fast gamma* oscillations are associated near the *theta* trough, where the peak of *slow gamma* is aligned with the early descending *theta* phase (Colgin et al., 2009; Schomburg et al., 2014). It is followed by *fast gamma*, appearing at the peak of CA1 pyramidal cell firing probability (Colgin et al., 2009; Lasztoczi and Klausberger, 2014).

*Fast gamma* oscillations in CA1 synchronize with the medial entorhinal cortex (MEC), presumably enhancing signaling from the MEC to CA1 (Bragin et al., 1995; Colgin et al., 2009). CA1 plasticity is thought to be most efficient during the *theta* phase of *fast gamma*, which is therefore hypothesized to be essential for memory encoding (Huerta and Lisman, 1995; Jutras et al., 2009). During the *slow gamma* oscillation states CA1 on the other hand synchronizes with CA3, which is likely to promote transmission from CA3 to CA1 (Bragin et al., 1995; Colgin et al., 2009; Montgomery and Buzsaki, 2007). *Slow gamma* might play a crucial role in memory retrieval (Hasselmo et al., 2002). The portion of CA1 pyramidal

## 1 INTRODUCTION

cells being phase-locked to *slow gamma* is decreased as compared to *fast gamma* (Colgin et al., 2009). Data suggests that *slow gamma* is driven by transient feedforward inhibition from CA3 (Csicsvari et al., 2003). However, the selection mechanism of pyramidal cells participating during *gamma* is not known yet.

*In vitro*, multiple pharmacological gamma models have been described for hippocampal brain slice approaches. The muscarinic acetylcholine receptor agonist carbachol induces gamma oscillations ( $\sim 35\text{-}70$  Hz; Fellous and Sejnowski 2000; Fisahn et al. 1998), simulating medial cholinergic septum input to the hippocampus and enhancing synchronous spiking of CA1 pyramidal neurons (Ovsepian, 2006). Carbachol-based gamma oscillations are shown to be generated by inhibitory interneurons (Gulyas et al., 2010). Furthermore, the ionotropic glutamate receptor agonist kainate also induces tonic excitation, resulting in gamma oscillations in the frequency range of  $\sim 20\text{-}80$  Hz (Fisahn et al. 2004; Fuchs et al. 2007). As a third prominent approach, Whittington et al. (1995) describe an interneuron gamma model. It is induced by activating metabotropic glutamate receptors, which results in the excitation and consecutive synchronization of inhibitory interneuron networks. All pharmacological gamma induction are modified by modulation of GABA<sub>A</sub> receptors (Bartos et al., 2007; Fisahn et al., 2004; Traub et al., 1996; Whittington et al., 1995), which underlines the importance of inhibition in gamma oscillatory activity. Moreover, gamma oscillations can be evoked by optogenetic stimulation (Akam et al., 2012; Butler et al., 2016; Pastoll et al., 2013). The light-gated ion channel channelrhodopsin was expressed in either pyramidal cells (Akam et al., 2012; Butler et al., 2016) or inhibitory interneurons (Pastoll et al., 2013) and the respective cells were stimulated with increasing light intensities. Upon light-evoked activation the local network resonates in a gamma frequency range ( $\sim 24\text{-}80$  Hz).

### 1.3.3 Sharp Wave-Ripple Oscillations ( $\sim 0.01\text{-}3\text{ Hz}$ / $\sim 110\text{-}250\text{ Hz}$ )

SPW-Rs, comprising  $\sim 0.01\text{-}3\text{ Hz}$  sharp waves and  $\sim 110\text{-}250\text{ Hz}$  superimposed ripples, are thought to originate in the hippocampus (Buzsaki, 1986; Maier et al., 2003; Schlingloff et al., 2014), as illustrated in figure 1.3. They are believed to be electrophysiological biomarkers for memory consolidation (Buzsaki, 2015). Abolition of SPW-Rs leads to an impaired performance in memory tasks (Girardeau et al., 2009). As pointed out in section 1.1.2, during active waking subsets of CA3 and CA1 pyramidal cells form receptive fields for specific locations in space, namely place fields. During awake stillness and slow wave sleep these internal representations of the external world are consolidated (Csicsvari and Dupret, 2014; Kali and Dayan, 2004). For this purpose, previously activated place cells are replayed in a timely compressed manner during SPW-Rs. Evidence suggests that SPW-Rs precede cortical spindle activity (Siapas and Wilson, 1998). This indicates an essential role in encoding and consolidating episodic and declarative memories. (Karlsson and Frank, 2009; Lee and Wilson, 2002; Ramadan et al., 2009; Squire, 1992).

Superimposed ripples, however, reflect the synchronous consecutive spiking of CA1 principal and inhibitory neurons (Buzsaki et al., 1992; English et al., 2014). According to the "*two-stage model of memory trace formation*", SPW-Rs are initiated by population burst of CA3 pyramidal cells (section 1.1.2; Buzsaki 1989). However, the two-stage model might have to be revised. Recent evidence suggests an essential role of CA2 neurons, which

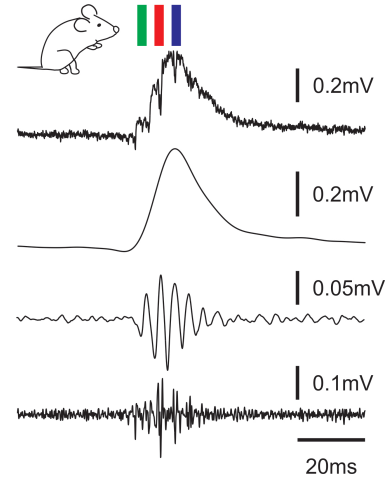


**Figure 1.3:** Example *in vitro* sharp-wave ripple.

During behavioral states which are not associated with theta rhythms, like grooming (indicated by the mouse drawing), SPW-R oscillations can be observed in the hippocampal CA region. Top: Vertical bars indicate temporally compressed spiking of reactivated place cells, which correspond to figure 1.2 A. First trace: Original sharp wave-ripple recorded in CA1 stratum pyramidale, *in vitro*. Below different frequency bands are illustrated. Sharp wave: low pass. Ripple oscillations: band pass. Multi-unit activity: high pass.

elicit population bursts prior to SPW-Rs, recorded in CA3 (Oliva et al., 2016).

The origin of the local field potential during sharp waves in the stratum pyramidale is still being debated. Sharp waves recorded in the stratum pyramidale potentially result from inhibitory inputs onto pyramidal cells (Schonberger et al., 2014; Valero et al., 2015). Whereas sharp waves which are observed in stratum radiatum might represent the excitatory population burst inputs onto pyramidal cell apical dendrites (Buzsaki, 1989; Buzsaki et al., 1983). The discussion about the hippocampal region of SPW-Rs initiation is still ongoing.

### **Ripple-Associated Ensemble Generation**

The spiking order of principle cells within neuronal ensembles dynamically depends on the behavior of the animal. Therefore, ensemble formation is unlikely to be predefined by hard-wired anatomical connections. Consequently, regarding ripple-associated ensembles, multiple ensemble building principles have been proposed. Ripple generation in CA1 constitutes a local process. Independent of CA3, CA1 place cell firing is phase-locked to CA1 but not to CA3 ripples (Sullivan et al., 2011). In accordance, CA3 and CA1 ripples are non-coherent and exhibit different frequency ranges (Csicsvari et al., 1999a; Sullivan et al., 2011).

At the current state of knowledge, hippocampal CA1 ripple oscillations are proposed to be explained by the following five non-exclusive mechanisms (figure 1.4).

**Ⓐ Reciprocal mechanism (figure 1.4 A):** The first model proposes that interactions between inhibitory interneurons are solely responsible to generate the fast ripple rhythm. The entire neuronal network is then synchronized via feedforward inhibition of inhibitory interneuron networks onto excitatory pyramidal cells. The required excitatory stimulus that activates the respective interneurons is provided by sharp wave activity. Their membrane potential starts to oscillate, presumably through the interplay between persistent sodium and slowly inactivating potassium conductance (Buzsaki and Chrobak, 1995). Next, the interneuron network oscillations synchronize due to  $\gamma$ -aminobutyric acid

A ( $\text{GABA}_A$ ) synaptic time constants of reciprocal inhibition and intrinsic membrane dynamics (Geisler et al., 2005; Whittington et al., 1995). Interneuron networks are thus believed to impose periodic inhibitory input onto pyramidal cells.

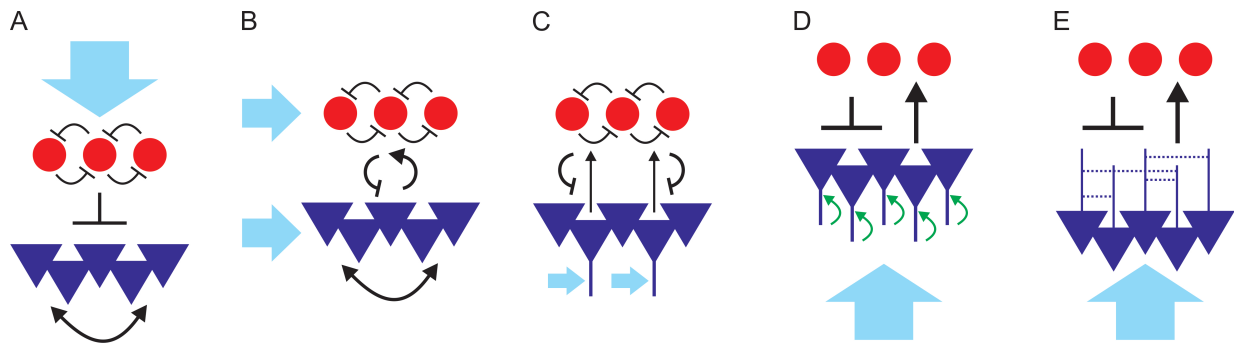


**Figure 1.4: Scheme of proposed models for hippocampal ripple generation mechanisms in CA1.**

Inhibitory interneurons and pyramidal cells are simplified by red circles and blue triangles, respectively. Azure arrows indicate broad sharp wave-driven excitation. Black arrow-completing lines show local excitation. Black-completing lines show local inhibition. **A. Reciprocal mechanism.** Upon excitatory sharp wave input, local interneurons synchronize through feedback inhibition. Inhibitory rhythm is conveyed onto pyramidal cells, which results in ripple frequency oscillations. The scheme was drawn based on evidence from Buzsaki and Chrobak (1995); Geisler et al. (2005); Taxidis et al. (2012); Ylinen et al. (1995) and Whittington et al. (1995). **B. Feedback mechanism.** Excitatory input onto both interneurons and pyramidal cells leads to ripple frequency oscillations, due to GABAergic synaptic time constants and intrinsic membrane dynamics. The scheme was drawn based on evidence from Brunel and Wang (2003) and Ylinen et al. (1995). **C. Reciprocal feedback mechanism.** The sole activation of pyramidal cells by incoming sharp waves leads to feed-forward activation of perisomatic interneurons. Eventually, direct interactions between inhibitory and excitatory neurons results in ripple oscillations. The scheme was drawn based on evidence from Geisler et al. (2005); Racz et al. (2009); Schlingloff et al. (2014) and Stark et al. (2014). **D. Mechanism based on non-linear dendritic integration.** Here, interneurons only fulfill a balancing function. Excitation of pyramidal cells is amplified by dendritic supralinear integration (indicated by green arrows). These cause dendritic sodium spikes, which synchronize pyramidal cells in the ripple frequency range. The scheme was drawn based on evidence from Ariav et al. (2003); Gasparini and Magee (2006); Gasparini et al. (2004) and Memmesheimer (2010). **E. Mechanism based on axo-axonal gap junctions.** Axonal gap junctions connect the axonal meshes of multiple pyramidal cells (blue dashed lines). Sharp wave input consequently results in ectopic APs, exciting other cells. Networks are thereby synchronized in high-frequency oscillations. The scheme was drawn based on evidence from Draguhn et al. (1998); Maex and De Schutter (2007); Nimrich et al. (2005); Schmitz et al. (2001); Traub and Bibbig (2000); Traub et al. (1999) and Traub et al. (2012).

The resulting frequency and synchrony yield oscillation activity in the ripple frequency

range (Taxidis et al., 2012; Ylinen et al., 1995).

Following this mechanism, a sharp wave from CA3 excites CA1 interneurons, which then synchronize and provide intermittent inhibition to spontaneously active CA1 principal cells, resulting in oscillatory activity of the network in the form of ripples.

**(B) Feedback mechanism (figure 1.4 B):** Reduced inhibitory to excitatory models suggest that fast oscillations can be generated via feedback inhibition (Ylinen et al., 1995). Inhibitory as well as excitatory cells receive excitation via network-entrained inputs, for instance through the CA3 input. The resulting oscillation frequency depends on the synaptic time constants and relative time scales of excitatory and inhibitory conductances (Brunel and Wang, 2003).

**(C) Reciprocal feedback mechanism (figure 1.4 C):** Evidence suggests that sole activation of pyramidal cells can be sufficient to induce high-frequency oscillations in hippocampal networks via feedback inhibition (Racz et al., 2009; Stark et al., 2014). Following the reciprocal feedback mechanism, pyramidal cells activate perisomatic interneurons, which in turn inhibit and thus pace the spiking of excitatory cells (Schlinghoff et al., 2014; Stark et al., 2014). The time constants of synaptic interaction between the two cell types then lead to fast oscillating network activity, fueled predominantly by excitatory input to principal cells (Geisler et al., 2005).

**(D) Mechanism based on non-linear dendritic integration (figure 1.4 D):** *In silico*, non-linear dendritic integration is suggested to be a stable mechanism for enhanced synchrony propagation in randomly connected neuronal networks (Jahnke et al., 2015; Memmesheimer, 2010; Memmesheimer and Timme, 2012). Dendritic sodium spikes mediate supra-linear integration. They are elicited by synchronous inputs to dendritic arbors (Ariav et al., 2003; Gasparini and Magee, 2006; Gasparini et al., 2004; Nevian et al., 2007). Consequently, dendritic spikes depolarize the soma rapidly, resulting in somatic APs, characterized by high temporal precision (Ariav et al., 2003).

In current CA1 models, the frequency of oscillations is determined by the timing of dendritic spikes and delay properties of the principal cell connections (Memmesheimer,



2010). In this way, dendritic spikes are essential for the generation of robust periodic activity with high-frequency oscillations, in hippocampal CA1 of about 200Hz, while inhibitory interneuron fulfill a global function (Memmesheimer, 2010).

**(E) Mechanism based on axo-axonal gap junctions (figure 1.4 E):** In principle, CA3 sharp waves can also result in fast oscillatory activity in CA1 via axo-axonal gap junctions between principal cells (Draguhn et al., 1998; Traub and Bibbig, 2000; Traub et al., 1999). These connections form an interconnected axonal mesh and in that way a sparse network of CA1 pyramidal cells. CA3 input onto CA1 is thereby multiplied in the axonal bulk of interconnected principal cells, resulting in axonal ectopic APs that lead to the excitation of other excitatory and inhibitory cells (Maex and De Schutter, 2007; Schmitz et al., 2001; Traub and Bibbig, 2000; Traub et al., 1999). Ectopic APs, also called antidromic spikes, represent APs that lack the positive charging of the somatodendritic compartment prior to the steep AP rise (Schmitz et al., 2001).

The resulting network activity resembles a burst of oscillations (Traub and Bibbig, 2000; Traub et al., 1999, 2012) of which the underlying high-frequency activity is suggested to be independent of synaptic transmission (Draguhn et al., 1998; Nimmrich et al., 2005). Interestingly, there is experimental evidence showing the proposed spiking behavior of pyramidal cells during SPW-Rs. Intracellular recordings from CA1 pyramidal cells revealed that about 41 % of the cells elicited ectopic-like APs during SPW-Rs *in vitro* (Bahner et al., 2011). The peculiar waveform suggests that ripple-associated APs reach the soma antidromically (Bahner et al., 2011), underlining the gap junction-based ripple mechanism.

Indeed, respective CA1 pyramidal cells are able to overcome SPW-R-entrained shunting inhibition. However, the exact mechanisms are still unknown.

## 1.4 The Potential of Endogenous Factors to Modulate and Protect Neuronal Networks

The spiking behavior of single neurons is controlled by rhythmical excitation and inhibition. Neuronal oscillations are thought to synchronize individual neurons into functional ensembles (Buzsaki and Draguhn, 2004; Engel et al., 2001). Endogenous and exogenous factors can modulate encoded information by either disturbing its content or enhancing coding efficacy. The neuropeptide oxytocin as well as the amyloid precursor protein have been shown to influence the activity of individual neurons. Both intrinsic factors are therefore postulated to fulfill vital roles in higher order information processing and storage. However, up to this date they remain to be investigated in detail.

### 1.4.1 The Hypothalamic Neuropeptide Oxytocin

The word oxytocin already contains information about the neuropeptide's impact on mammals. It originates from the Greek word *okytokine*, translating to 'quick birth'. Oxytocin facilitates pregnancy, lactation, delivery and maternal care (Feldman et al., 2010, 2011, 2007; Magon and Kalra, 2011). Oxytocin further modulates pregnancy-independent complex emotional and social behaviors (Kirsch et al., 2005; Kosfeld et al., 2005; Ross and Young, 2009) as well as stress alleviation and learning in mammals (Heinrichs et al., 2003, 2004).

Oxytocin is secreted by magnocellular as well as parvocellular cells. Magnocellular neurons are found in the paraventricular, supraoptic and accessory nuclei of the hypothalamus, projecting their axons to the posterior pituitary. They secrete the structurally similar neuropeptides oxytocin and vasopressin (Du Vigneaud et al., 1953; Katsoyannis and Du Vigneaud, 1958). Magnocellular neurons are evolutionary preserved cells, being found in reptilians, avians and mammalians (Knobloch and Grinevich, 2014). Recent evidence

#### 1.4 *The Potential of Endogenous Factors to Modulate and Protect Neuronal Networks*

suggests that magnocellular neurons form long-range connections to multiple forebrain regions, such as the central nucleus of the amygdala, presumably facilitating the named behavioral states (Althammer and Grinevich, 2017; Knobloch et al., 2012).

Oxytocin releasing parvocellular neurons are found in the paraventricular nucleus. Their axons project to the brain stem and spinal cord (Swanson and Kuypers, 1980; Swanson and Sawchenko, 1983), and possibly to the median eminence (Fink et al., 1988; Vandesande et al., 1977). Parvocellular neurons modulate autonomous functions like breathing (Mack et al., 2002), food intake (Blevins et al., 2004) and even pain perception (Rash et al., 2014). Parvocellular cells send oxytonergic projections to the dopamine system of the midbrain, amongst other, modulating the pars compacta of the substantia nigra and the ventral tegmental area (Xiao et al., 2017). The latter region is known to connect to the hippocampus, possibly influencing memory formation (Heinrichs et al., 2004).

Oxytocin and its receptor are widely found in the brain (Marlin and Froemke, 2017). In the hippocampus ORs are located in the regions DG, CA3, CA2 and CA1 (Hammock and Levitt, 2013; Mitre et al., 2016; Raam et al., 2017; Yoshida et al., 2009), which indicates an essential role of oxytocin in memory. Tomizawa et al. (2003) for instance showed that oxytocin facilitates long-term potentiation (LTP) during motherhood, improving long-term spatial learning. On the cellular level oxytocin enhances the activity of fast-spiking inhibitory interneurons, thereby enhancing the fidelity of AP transmission (Owen et al., 2013). As a result, oxytocin increases the timing precision of pyramidal cell firing as well as the signal-to-noise ratios (Owen et al., 2013).

All in all, oxytocin appears to play a vital role in modulating information processing in the brain. However, its effect on network rhythms remains to be elusive.

## 1.4.2 Amyloid Precursor Protein - A Fine Line Between Neurotoxicity and Neuroprotection

Alzheimer's disease represents the most common cause of dementia in developed countries (Prince et al., 2015). Interestingly, patients with hypoxic-ischemic brain injuries are more susceptible to Alzheimer's disease (Zhang and Le, 2010). Hypoxic conditions are accompanied by a dramatic increase in intracellular calcium levels, leading to neurodegeneration and apoptosis (Berridge, 2010).

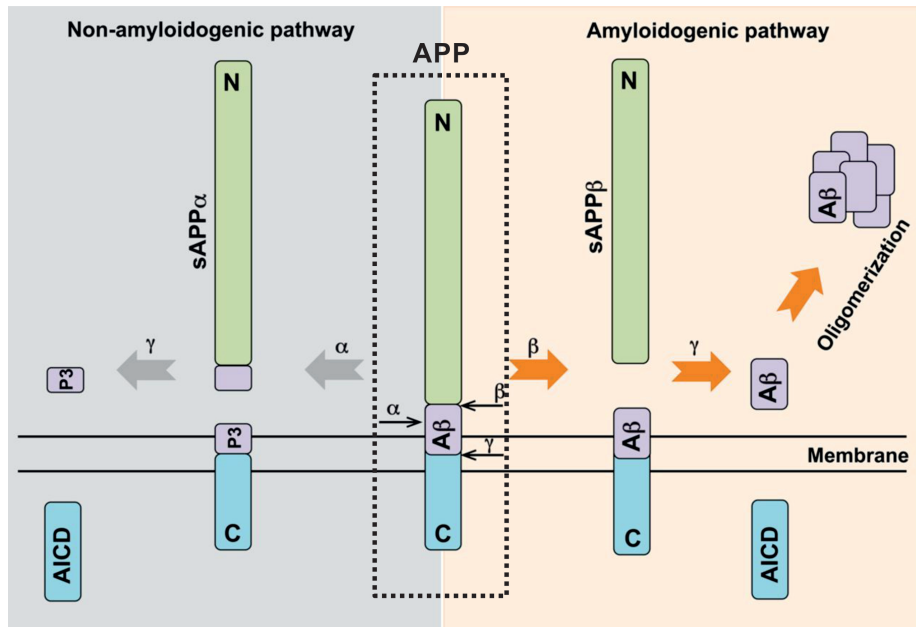


**Figure 1.5: Scheme of amyloid precursor protein metabolism.**

Amyloid precursor protein (APP; surrounded by a dashed square) is located in the neuronal membrane and can be cleaved by  $\alpha$ -,  $\beta$ -, and  $\gamma$ -secretase. The cleavage sites are indicated by black arrows. Following the **non-amyloidogenic pathway**,  $\alpha$ -secretase cleaves APP within the amyloid- $\beta$  domain, generating APPs $\alpha$  (soluble N-terminus fragment) and a non-amyloidogenic C-terminal fragment. Thereby,  $\alpha$ -secretase averts the formation of amyloid- $\beta$  (A $\beta$ ). The membrane-bound C-terminus is subsequently cleaved by  $\gamma$ -secretase, resulting in an amyloid precursor protein intracellular domain (AICD) and a P3 peptide (P3). In the **amyloidogenic pathway**,  $\beta$ -secretase cleaves APP at the beginning of the amyloid- $\beta$  domain, generating APPs $\beta$  (soluble N-terminus fragment) and an amyloidogenic C-terminal fragment. The latter one is subsequently cleaved by  $\gamma$ -secretase, which results in the generation of A $\beta$  and an AICD. Adapted from Nicolas and Hassan (2014).

#### 1.4 *The Potential of Endogenous Factors to Modulate and Protect Neuronal Networks*

In Alzheimer's disease, deposition of amyloid plaques in the extracellular space are assumed to play a major role in the pathogenesis of the disease (Murphy and LeVine, 2010). Amyloid plaques are formed by amyloid- $\beta$ , a cleavage product of the amyloid precursor protein (APP; figure 1.5). They can have profoundly negative effects on hippocampal network oscillations (Goutagny et al., 2013; Scott et al., 2012). In contrast, data from rodents suggest that APP itself fulfills a neuroprotective function against cellular stress (Kogel et al., 2012). APP overexpression even decreases the size of brain infarct volumes (Clarke et al., 2007), while lacking APP leads to increased acute mortality after hypoxic-ischemic brain injuries (Koike et al., 2012). APP $\alpha$  and APP $\beta$  are the two direct soluble cleavage products of APP, cleaved by  $\alpha$ - and  $\beta$ -secretase, respectively (figure 1.5). However, as opposed to APP $\beta$  (Hick et al., 2015) APP $\alpha$  facilitates multiple positive effects on neuronal encoding, rescuing plasticity and behavioral deficits of APP $^{-/-}$  animals (Hick et al., 2015; Ring et al., 2007). Astonishingly, APP $\alpha$  in fact shows memory enhancing effects when applied intraventricularly (Meziane et al., 1998). APP $\alpha$  is secreted upon neuronal activity (Gakhar-Koppole et al., 2008; Kirazov et al., 1997), exerting neuroprotective and trophic effects (Fol et al., 2016; Hick et al., 2015; Plummer et al., 2016). So far, the suggested neuroprotective effects of APP and / or APP $\alpha$  during hypoxia have not been extensively investigated on the cellular and network level. The impact of a deficiency in APP $\alpha$  on SPW-R oscillations is still open for investigation. However, it is crucial to study these potentially SPW-R-impairing mechanisms because changes in neuronal oscillations can have profound effects on network oscillations (Goutagny et al., 2013; Scott et al., 2012) as well as cognitive performance (Girardeau et al., 2009).



## 2 Aims of the Study

Within the scope of this thesis, we address the following issues using hippocampal mouse brain slices:

- **Study the selective activation mechanism of individual pyramidal cells in neuronal ensembles.** *In vitro* pyramidal cells depict a particular spiking behavior during hippocampal ensemble activation. How are single neurons recruited into neuronal ensembles? Is there a functional relationship between observed spiking behaviors and described peculiar anatomical features of specific pyramidal cells?
- **Investigation of the modulatory impact of oxytocin receptor activation on network oscillations.** Former studies suggest a decisive correlation between oxytocin application and changes in the cognitive performance in human subject groups. To what extent are hippocampal network oscillations modulated by oxytocin? Are distinct neural rhythms influenced selectively?  
To conduct required experiments, we implemented a spatially and temporally precise illumination system, which enabled us to selectively activate defined cell types.
- **Find underlying evidence for altered calcium dynamics in amyloid precursor protein deficient mice.** The amyloid precursor protein appears to fulfill a neuroprotective role during ischemic brain injury. Which ion channels are involved in this protection mechanism and what are the characteristics of the resulting intracellular calcium dynamics?





## 3 Materials and Methods

### 3.1 Applied Drugs

**Table 3.1:** *List of applied drugs*

| Item   | Supplier  |
|--|---|
| (2S,3S,4S)-Carboxy-4-(1-methylethenyl)-3-pyrrolidineacetic acid  | Tocris, Bristol, United Kingdom                   |
| Carbamoylcholine chloride  | Sigma-Aldrich, Steinheim, Germany                 |
| DesGly-NH <sub>2</sub> -d(CH <sub>2</sub> ) <sub>5</sub> -[D-Tyr <sub>2</sub> ,Thr <sub>4</sub> ]OVT             | Maurice Manning, College of Medicine, Toledo, USA |
| Nifedipine   | Sigma-Aldrich, Steinheim, Germany                 |
| L-Glutamic acid monosodium salt hydrate  | Sigma-Aldrich, Steinheim, Germany                 |
| [Phenylacetyl <sup>1</sup> , O-Me-D-Tyr <sup>2</sup> , Arg <sup>6,8</sup> , Lys <sup>9</sup> ]-Vasopressin amide | Sigma-Aldrich, Steinheim, Germany                 |
| Picrotoxin   | Tocris, Bristol, United Kingdom                   |
| (Thr <sup>4</sup> ,Gly <sup>7</sup> )-Oxytocin H-Cys-Tyr-Ile-Thr-Asn-Cys-Gly-Leu-Gly-NH <sub>2</sub>             | Bachem, Bubendorf, Switzerland                    |
| (Arg <sup>8</sup> )-Vasopressin (H-Cys-Tyr-Phe-Gln-Asn-Cys-Pro-Arg-Gly-NH <sub>2</sub> )                         | Bachem, Bubendorf, Switzerland                    |

## 3.2 Animal Handling and Slice Preparation

Animals were treated in accordance with guidelines of the Federation of European Laboratory Animal Science Associations (FELASA). In our experiments we used male wild-type (WT, Charles River, Sulzfeld, Germany), APP<sup>-/-</sup> and APPs $\alpha$ -KI mice with a C57BL/6 background. APP<sup>-/-</sup> and APPs $\alpha$ -KI animals were provided by Ulrike Mueller (Institute for Pharmacy and Molecular Biotechnology, Functional Genomics, Heidelberg University). Mice were anesthetized by defined CO<sub>2</sub> influx into animal cage. After loss of the righting reflex mice were decapitated, the brain was surgically removed and immediately stored in ice-cold (<4°C) artificial cerebrospinal fluid (ACSF), containing in mM: 124 NaCl (AppliChem, Darmstadt, Germany), 3 KCl (AppliChem, Darmstadt, Germany), 1.25 NaH<sub>2</sub>PO<sub>4</sub> (Grüssing, Filsum, Germany), 1.6 CaCl<sub>2</sub> (AppliChem, Darmstadt, Germany), 1.8 MgSO<sub>4</sub> (Merck, Darmstadt, Germany), 10 glucose (Merck, Darmstadt, Germany), 26 NaHCO<sub>3</sub> (Sigma-Aldrich, Steinheim, Germany), saturated with 95 % O<sub>2</sub> and 5 % CO<sub>2</sub> (pH = 7.4). Frontal and parietal lobes as well as cerebellum were largely removed to then glue the brain to a vibratome cutting chamber (Leica VT1000S, Leica Biosystems GmbH, Nussloch, Germany). The following slicing procedure allowed us to obtain 400  $\mu$ m thick, horizontal slices. These were quickly transferred to a Haas-type interface recording chamber (Haas et al., 1979) in which slices were allowed to recover for at least 2 hours and to record signals under defined flow (1.2 - 1.6 ml / min) of pH-adjusted ACSF at 35 %  $\pm$  1 °C.

## 3.3 Electrophysiology

### 3.3.1 Standard Local Field Potential Recordings

Glass electrodes (GB200F-10, Science Products, Hofheim, Germany) were pulled to an opening of about 9-12  $\mu$ m using a DMZ-Universal-Electrode-Puller (Zeitz, Martinsried,

Germany) and filled with ACSF. After lowering such a glass electrode onto the slice surface, extracellular field potentials were recorded in hippocampal stratum pyramidale of CA1. Field potentials were amplified 100x, filtered at 2 kHz (lowpass) and at 0.3 Hz (highpass) using a EXT 10-2F amplifier (npi electronics, Tamm, Germany), direct-current-filtered, digitized at 20 kHz for off-line analysis (power1401 digital/analog converter, Cambridge Electronic Design, Cambridge, UK) and sampled with SPIKE2 (Cambridge Electronic Design, Cambridge, United Kingdom). Prior to any drug administration baseline SPW-R activity was recorded for at least 5 minutes.

#### 3.3.2 Single Cell Sharp Electrode Intracellular Recordings

Glass electrodes (GB100F-10, Science Products, Hofheim, Germany) were pulled to a resistance of 60-150 M $\Omega$  using a DMZ-Universal-Electrode-Puller and filled with 2 M potassium acetate (Grüssing, Filsum, Germany; pH 7.35) containing 1 % biocytin (Sigma-Aldrich, Steinheim, Germany). Intracellular potentials were amplified 10x, filtered at 8 kHz (lowpass) using Axoclamp 900A amplifier (Molecular Devices, Biberach an der Riss, Germany), DC-filtered, digitized at 20 kHz for off-line analysis (power1401 digital/analog converter, Cambridge Electronic Design, Cambridge, United Kingdom) and sampled with Signal4 (CED, Cambridge, United Kingdom) as well as SPIKE2 software. After impalement cells were stabilized through negative current injection, followed by at least 5 min of zero current injection. Bridge balance was set and repeatedly adjusted throughout the recording, by using negative squared current pulses (-200 pA). These were also applied to calculate input resistance and membrane time constant (-200 pA for 500 ms each, every 2 s). Input resistance was calculated by applying Ohm's law ( $R_{\text{Input}} = V_{\text{measured}} / I_{\text{injected}}$ ). Membrane time constant was determined by a monoexponential fit of the first 50 ms of negative voltage responses upon current onset. Intrinsic characteristics of cells were measured through consecutive current steps, ranging from negative to positive currents (200 pA steps, each for 100-500 ms). For post-hoc data analysis cells were required to remain stable during current-free recording (at least 10 min in total) and to elicit overshooting ac-

### 3 MATERIALS AND METHODS

tion potentials with typical firing characteristics of pyramidal cells during positive current injection.

#### 3.3.3 Conductance Analysis and Statistics

Understanding hippocampal ensemble activity in the brain requires knowledge about synaptic conductance inputs to individual principle cells. Estimates of synaptic conductances contribute to the understanding of single cell recruitment to such temporally specific population activity. They describe the evolution of the membrane voltage and in that way provide information on the nature of networks inputs. Excitatory and inhibitory inputs to a single cells are formed by various synaptic channels. They affect the membrane voltage according to their respective characteristic reversal potential and conductance. Combined integration of excitatory and inhibitory conductances leads to intracellularly obtainable voltage and current responses. These do not only depend on conductance amplitudes, kinetics and reversal potential but also on parameters like the time constant of the membrane, resting membrane potential, leak conductance and the conductance overlap.

For post-hoc conductance calculations individual cells were recorded in conjunction

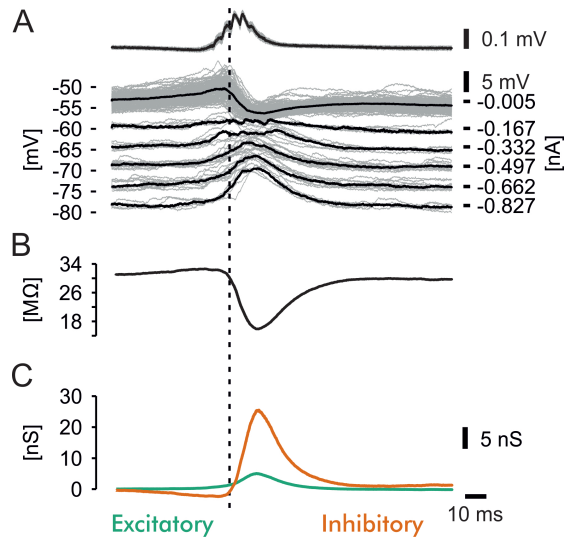


**Figure 3.1: Example pyramidal cell recording during SPW-Rs and corresponding conductance changes.**

**(A) Spontaneously occurring SPW-Rs (top traces) induced intracellular membrane potential deflections (bottom traces).** Respective potentials are indicated on the left, applied currents are shown on the right. Gray - individual responses per SPW-R, black - median of individual responses. **(B) Time course of the input resistance change, induced by SPW-Rs in A.** **(C) Mean of induced SPW-R conductance changes.** Green - excitatory, orange - inhibitory. Dotted lines indicate the first ripple before the peak of median SPW-R.

with spontaneous SPW-R oscillations (figure 3.1 A, top). We injected 5 negative squared current pulses with decreasing amplitude and at least a single positive pulse. Each current injection was selected to shift the membrane potential for about 5 mV (figure 3.1 A, bottom). Time of current injections was either 30 s, with 30 s of current-free recordings in between individual pulses ( $n_{\text{baseline}} = 32$ ,  $n_{\text{picrotoxin}} = 6$ ), or for the duration of 40 occurring SPW-Rs, with 40 SPW-Rs appearing during current-free recordings ( $n_{\text{baseline}} = 4$ ,  $n_{\text{dynamic clamp}} = 1$ ). To infer excitatory and inhibitory synaptic conductance from membrane potential changes we employed a multi-trial method of continuous conductance estimation of stimulus-evoked voltage deflections, as originally described by Borg-Graham et al. (1998). We modified this method for current-clamp recordings, following Priebe and Ferster (2005). Computational approaches by Koch et al. (1990) lay out that conductance changes resulting from perisomatic inhibitory basket cell activity can be recorded at the soma. Thus, we took into consideration that excitatory as well as inhibitory input signals affected the electric activity of the membrane, either via polarization or shunting.

As described above, we targeted single pyramidal cells in hippocampal CA1 using sharp microelectrodes. We aimed to calculate excitatory and inhibitory components from synaptic conductance by applying the aforementioned stimulations (figure 3.1; section 3.3.2: *Single cell sharp electrode intracellular recordings*). In short, off-line analyses were performed as follows. We only took non-voltage-dependent conductances into account. Action potentials were thus excluded from the analysis due to their non-linear current to voltage relations. Additionally, we assumed that only two major types of synaptic inputs, non-NMDA-excitatory and inhibitory, reached the target cell. This enabled an estimation of the corresponding conductance at each time point, during a SPW-R. Reversal potentials of excitatory and inhibitory currents were estimated according to the reversal potentials of  $\alpha$ -amino-3-hydroxy-5-methyl-4-isoxazolepropionic acid (AMPA) and GABA, being 0 mV and -75 mV respectively.

### 3 MATERIALS AND METHODS

**Algebraic calculations of corresponding conductances were performed using the following equations.** Synaptic conductance is composed of the sum of excitatory and inhibitory conductances.

$$(3.1) \quad g_{\text{synaptic}}(t) = g_{\text{excitatory}}(t) + g_{\text{inhibitory}}(t)$$

By applying Ohm's law  $U = R \cdot I_{\text{total}} = \frac{I_{\text{total}}}{g_{\text{synaptic}}(t)}$  the apparent reversal potential can be calculated as

$$E_{\text{synaptic}}(t) = \frac{I_{\text{total}}}{g_{\text{synaptic}}(t)} = \frac{I_{\text{total}}}{g_{\text{excitatory}}(t) + g_{\text{inhibitory}}(t)}$$

with  $I_{\text{total}} = E_{\text{synaptic}}(t) \cdot g_{\text{synaptic}}(t)$  the apparent reversal potential is defined by

$$(3.2) \quad E_{\text{synaptic}}(t) = \frac{[E_{\text{excitatory}}(t) \cdot g_{\text{excitatory}}(t)] + [E_{\text{inhibitory}}(t) \cdot g_{\text{inhibitory}}(t)]}{g_{\text{excitatory}}(t) + g_{\text{inhibitory}}(t)}.$$

Next, the derivation of the specific conductance equations is shown for the inhibitory conductance. Excitatory conductance computation was performed respectively. By combining the equations (3.1) and (3.2) the apparent reversal potential can be further characterized by

$$(3.3) \quad \begin{aligned} E_{\text{synaptic}}(t) \cdot g_{\text{synaptic}}(t) = & [E_{\text{excitatory}}(t) \cdot (g_{\text{synaptic}}(t) - g_{\text{inhibitory}}(t))] \\ & + [E_{\text{inhibitory}}(t) \cdot g_{\text{inhibitory}}(t)]. \end{aligned}$$

After transformation of the equation (3.3) the excitatory conductance can be calculated as

$$g_{\text{inhibitory}}(t) = \frac{[E_{\text{synaptic}}(t) \cdot g_{\text{synaptic}}(t)] - [E_{\text{excitatory}}(t) \cdot g_{\text{synaptic}}(t)]}{[E_{\text{inhibitory}}(t) - E_{\text{excitatory}}(t)]}.$$

The resulting equations, seen below, were then applied to compute inhibitory as well as

excitatory conductance.

$$(3.4) \quad \mathbf{g}_{\text{inhibitory}}(\mathbf{t}) = \frac{\mathbf{g}_{\text{synaptic}}(\mathbf{t}) \cdot [\mathbf{E}_{\text{synaptic}}(\mathbf{t}) - \mathbf{E}_{\text{excitatory}}(\mathbf{t})]}{\mathbf{E}_{\text{inhibitory}}(\mathbf{t}) - \mathbf{E}_{\text{excitatory}}(\mathbf{t})}$$

$$(3.5) \quad \mathbf{g}_{\text{excitatory}}(\mathbf{t}) = \frac{\mathbf{g}_{\text{synaptic}}(\mathbf{t}) \cdot [\mathbf{E}_{\text{inhibitory}}(\mathbf{t}) - \mathbf{E}_{\text{synaptic}}(\mathbf{t})]}{\mathbf{E}_{\text{inhibitory}}(\mathbf{t}) - \mathbf{E}_{\text{excitatory}}(\mathbf{t})}$$

Figure 3.1 C shows the median excitatory and inhibitory conductance changes over the course a median SPW-R for a representative example cell. Further, we sub-divided the original conductance changes into fast and slow components. To separate these conductance components, we filtered the obtained conductance changes (fast: 150 - 300 Hz) and subtracted the resulting signal from the original conductance changes (slow). The integral of the resulting curves was calculated by trapezoidal numerical integration. Statistical difference was tested with the nonparametric Wilcoxon's signed-rank test. Data were analyzed using custom-written MATLAB (The MathWorks) algorithms.

### 3.3.4 Implementation of a Dynamic Clamp System

#### Working Principle of the Dynamic Clamp System

Dynamic clamp utilizes an *in silico* model to introduce artificial conductances into intracellularly recorded neurons (Robinson and Kawai, 1993; Sharp et al., 1993). It thereby offers the advantage of precise alteration of synaptic conductances while avoiding unknown side effects of drug applications. Here, we designed a dynamic clamp model that allowed us to counteract perisomatic inhibitory conductance inputs to an individual cell during SPW-Rs. Furthermore, our model computed an average conductance change over the course of an average SPW-R that was specific of the recorded cell and the activity state of the network. The annihilation basically represented a two-step process. First, after invading a target cell, we obtained SPW-R-entrained inhibitory con-

### 3 MATERIALS AND METHODS

ductance changes, as described in section 3.3.3. These changes were averaged across multiple SPW-Rs, as the conductance changes varied between SPW-Rs. The mean inhibitory conductance change  $g_{\text{inhibitory}}(t)$  was then provided to the *in silico* model:  $I = g_{\text{inhibitory}}(t) \cdot (V_m - E_{\text{reversal, inhibitory}})$ . Note that time  $t$  represents the beginning of the crossing of the SPW-R detection threshold and  $E_{\text{reversal, inhibitory}} = -75\text{mV}$ .

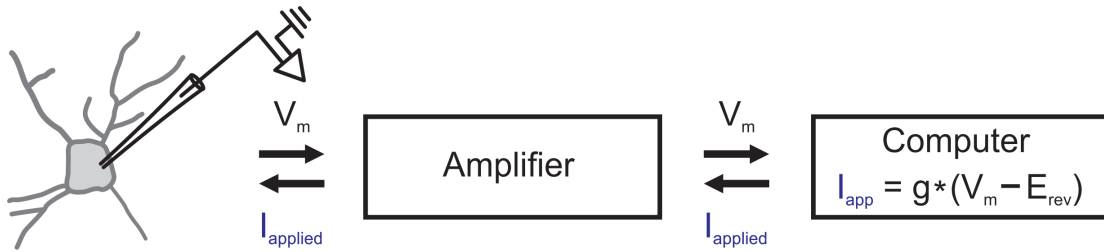


**Figure 3.2: Scheme of the dynamic clamp recording principle.**

In current clamp, the intracellular membrane potential is recorded and provided to an *in silico* model, which calculates the actual current via  $I = g \cdot (V_m - E_{\text{reversal}})$ . Abbreviations:  $I_{\text{applied}}$  - Applied current,  $V_m$  - Membrane potential,  $g$  - Modeled conductance,  $E_{\text{reversal}}$  - Reversal potential.

The second step represented the injection of the calculation current evolution upon SPW-R detection. Consequently, for each time point during a SPW-R event, the applied current varied continuously depending on two parameters, the target cell's membrane potential and the prior obtained mean inhibitory conductance change over multiple SPW-Rs. The membrane potential was recorded as described in section 3.3.2, however using the SEC05-X (npi electronics) amplifier. The illustrated closed-loop approach was performed with the RELACS software (Benda et al., 2007; Walz et al., 2014).

### Contributions to the Implementation of a Dynamic Clamp System

Installation of dynamic clamp hardware was done by Dr. Alexei Egorov, Franziska Lorenz and Paul Pfeiffer. The aforementioned recording procedure was implemented by Paul Pfeiffer and Martin E. Kaiser, aided by Dr. Martin Both. The functional principle of the applied dynamic clamp model was designed by Dr. Martin Both, Paul Pfeiffer and Martin E. Kaiser. It was coded in C and rendered user friendly by Paul Pfeiffer. Custom-



written MATLAB algorithms were coded by Dr. Martin Both and Martin E. Kaiser.

### 3.3.5 Microelectrode Array Recordings

#### Microelectrode Array Recording and Perfusion System

As exemplified in section 3.2, brain slices were placed in a Haas-type interface recording chamber for post-preparation recovery. After verification of spontaneous SPW-R activity (as described in section 3.3.1) slices were placed on a permeable microelectrode array (MEA; 60pMEA200/30iR-Ti-pr; Multi Channel Systems, Reutlingen, Germany). Extracellular field potentials were obtained from 60 electrodes ( $30\ \mu\text{m}$  in diameter each) with an interpolar distance of  $200\ \mu\text{m}$ , using hard- and software provided by Multi Channel Systems. Field potentials were amplified, filtered at  $8\ \text{kHz}$  (lowpass) and  $0.3\ \text{Hz}$  (highpass), and digitized at  $25\ \text{kHz}$  for off-line analysis. Due to MEA perforation, slices were rapidly provided with ACSF at  $4\text{-}5\ \text{ml / min}$ , saturated with  $95\ \%$   $\text{O}_2$  and  $5\ \%$   $\text{CO}_2$  ( $\text{pH} = 7.4$ ). As indicated in figure 3.3, the ACSF perfusion was provided beneath and above the slice, using a peristaltic pump (REGLO Analog, Ismatec, Germany) as well as sole gravity in combination with a vacuum pump (CVP, Multi Channel Systems), respectively. The lower perfusion created a negative pressure, which sucked the slice onto the MEA, ensuring a continuous ACSF supply and tight tissue to electrode contact. At  $32^\circ\text{C}$  (PH01 heater, Multi Channel Systems), this approach enabled us to record spontaneously occurring SPW-Rs (Hajos et al., 2009; Maier et al., 2009) as well as optically induced gamma oscillations.

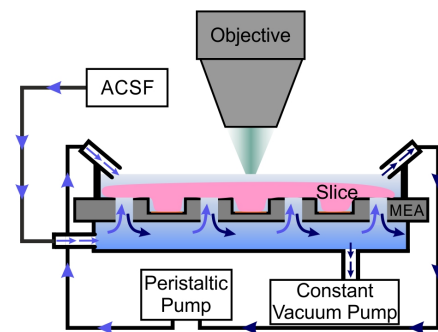


**Figure 3.3: Scheme of the microelectrode array perfusion system.**

Perfusion system (Multi Channel Systems) provided an upper and lower flow of ACSF. Rapid exchange of ACSF enabled us to record spontaneous SPW-R as well as induced gamma oscillations.

### 3 MATERIALS AND METHODS

#### Data Analysis and Statistics

Data shown in section 4.2 were obtained using the microelectrode array recording system and analyzed using custom-written MATLAB routines, based on the Neuroshare MATLAB API algorithm. We downsampled acquired data 10x and applied the morlet wavelet transform method (MATLAB wavelet toolbox [cmor1-1.5]). Statistical difference was tested with the nonparametric Wilcoxon matched-pairs signed-ranks test.

#### Contributions to the Microelectrode Array Recordings

The installation of the microelectrode array recordings system was accomplished by Dr. Martin Both, Dr. Pascal Geschwill and Martin E. Kaiser. MATLAB algorithms were custom-written by Dr. Martin Both, Dr. Jan-Oliver Hollnagel and Martin E. Kaiser.

## 3.4 Intracranial Injections of Viral Vectors

For analgesia animals received 0.1 mg / kg buprenorphine hydrochloride (Temgesic; Indivior, Richmond, United States) subcutaneously, about 30 min prior to surgery. During surgery we continuously observed the depth of isoflurane-induced anesthesia. Breathing rhythm and toe pinch reflex allowed us to adjust isoflurane flow accordingly. A moisturizing ointment protected the animals' eyes against exsiccosis. Mice were placed on a 37 °C warm heating pad.

Body temperature was continuously measured on the outside of the abdomen. As soon as mice were anesthetized, we began the surgery. Fur on the head was partly removed, the

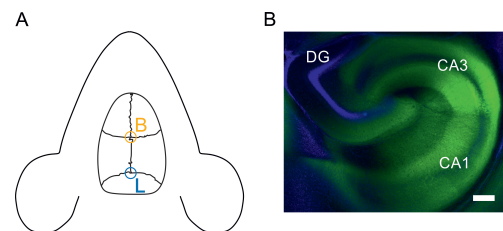


**Figure 3.4: Cranial injections yielded consistent viral expression.**

**(A) Scheme of the anatomical landmarks.** Abbreviations: B - Bregma, L - Lambda. **(B) Example slice showing the expression of eYFP.** Green - expression of eYFP, blue - DAPI staining; Scale bar represents 200  $\mu\text{m}$ .

### 3.4 Intracranial Injections of Viral Vectors

skin was disinfected and incised along the sagittal midline for about 1 cm. We expanded the skin and dried the skull surface with cotton sticks.

Using the anatomical landmarks bregma and lamda (figure 3.4 A), the skull was leveled in the lateral-medial and the anterior-posterior axes. Viral vectors were dispensed in 350 mM NaCl and 5 % D-Sorbitol in PBS (viral solution), resulting in titers of about  $4 \cdot 10^{12}$  viral genomes per ml. At the bilateral injection sites (in reference to bregma: anterior-posterior = -2.8; lateral-medial =  $\pm 3.5$ ; dorsal-ventral = -3.3, -3.1 and -2.9) the skull was opened locally, using a dental drill (Hager & Meisinger, Neuss, Germany). At each location in the dorsoventral axis, we pressure-applied 400 nl viral solution through a microsyringe (Hamilton Company, Reno, United States), at 200 nl / min (SYS-Micro4, World Precision Instruments, United States). After application the skull surface was moisturized with 0.9 % NaCl and the skin was stitched. Animals recovered from surgery under 28 °C warm infrared light for about 1 h. We again administered 0.1 mg / kg buprenorphine hydrochloride 3.5 h after surgical intervention. During subsequent viral incubation time of 3-4 weeks mice were checked upon on a daily basis.

In order to optically activate principle cells, we injected the recombinant adeno-associated virus (AAV) vector (AAV5-CaMKII $\alpha$ -hChR2[H134R])-eYFP (Vector Core Facility, University of North Carolina, USA) into both hemispheres. Briefly, channelrhodopsin-2 (ChR2) is a light-sensitive cation channel, found in the green alga *Chlamydomonas reinhardtii* (Nagel et al., 2005, 2003). It was expressed under the calcium/calmodulin-activated protein kinase II  $\alpha$  (CaMKII $\alpha$ ) promoter. As a result we observed a specific expression of ChR2 in glutamatergic hippocampal neurons (Liu and Jones, 1996), which entailed the possibility to depolarize these in a temporally precise manner (Boyden et al., 2005). The viral vector comprised humanized ChR2 (hChR2[H134R]), which is an engineered gain-of-function ChR2 mutant. It yields larger photocurrents, increasing the probability of AP induction at comparatively low light intensities (Nagel et al., 2005). To render the expression of ChR2 visible, viral vectors contained as fusion protein the enhanced yellow fluorescent protein (eYFP; figure 3.4 B). YFP was developed on the basis of the green fluorescent protein from the jellyfish *Aequorea macrodactyla* (Xia et al.,

2002). Regarding the expression pattern, we aimed for a broad and consistent expanse. We therefore applied the AAV5 serotype, which as compared to other serotypes is known to transverse the hippocampus effectively, infecting a large volume of neuronal cells (figure 3.4 B; Aschauer et al. 2013; Burger et al. 2004).

## Contributions to Intracranial Injections of Viral Vectors

Surgeries were performed by Katja Lankisch and Martin E. Kaiser.

## 3.5 Illumination and Microscopy

### 3.5.1 Implementation of a Holographic Illumination and Imaging System

A major part of the presented work included the implementation of a holographic illumination system in combination with a CSU-X1 Nipkow-type spinning-disk for confocal imaging. Holographic light presentation was generated with a spatial light modulator (SLM; X10468, Hamamatsu Photonics, Japan). By utilizing liquid crystals on silicon (LCOS) it modulates the phase of a light beam. Voltages can be applied to individual pixels, allowing a defined phase retardation of the incident light wavefront. In that way the resulting intensity patterns yield the projected image (Neff et al., 1990; Papagiakoumou et al., 2010; Zhang et al., 2014). Figure 3.5 illustrates a scheme of the illumination and imaging system. As a light source, we used a diode-pumped solid state laser (wavelength = 473 nm; DL473 Rapp Optoelectronics, Germany). Light passed a polarization filter (P) to ensure specific angle of light polarization, required for phase modulation by the SLM. Before reaching the SLM the light beam was expanded to 20 mm in diameter (lens L1) and converted into parallel rays to infinity (lens L2). Thereby the light fully covered the SLM's aperture. Due to the grid structure of the pixel arrays non-modulated

### 3.5 Illumination and Microscopy

light formed higher order diffraction effects. These disturbances reduced the quality of the generated holographic image dramatically and therefore needed to be removed. First and foremost, we shifted the zero order diffraction pattern from the image by applying an additional fresnel lens to the SLM. Then, we were able to filter the zero-order without disturbing the image. As zero-order filter (ZF), we modified a glass coverslip by drawing a simple black dot in the center. This blocked transmission of the center of the ray, which contained the zero order diffraction. From there on, a dichroic mirror guided the light beam through a tube lens. This lens converted the light to parallel rays again. Then the light passed the objective (Nikon LWD, 169/0.80 w, 16x magnification, water immersion, [working distance = 3.0], Nikon, Japan) and the holographic image was focused onto the slice. Using this objective, we were able to illuminate a field of view of  $353 \times 353 \mu\text{m}$  with a maximum light intensity of  $0.3 \text{ mW} / \text{mm}^2$ .

In MATLAB, we developed a custom-made graphical user interface to enable live image acquisition and to define the pattern of holographic light presentation. The latter one was drawn with the graphical user interface and Fourier transformed based on the Gerchberg–Saxton algorithm from (Gerchberg and Saxton, 1972). Together with a computational insertion of a fresnel lens and the setting of the pattern of light intensity progression, we were able to project light onto the slice in a temporally and locally precise

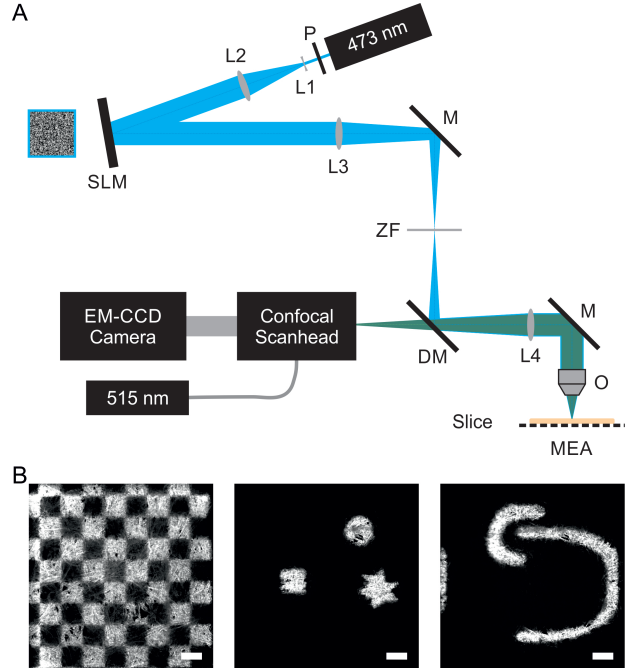


**Figure 3.5: Scheme of the holographic illumination and imaging system.** (A) **Schematic drawing of the illumination and imaging light path.** Abbreviations: P - polarization filter, L1-L4 - lenses, SLM - spatial light modulator, M - mirror, ZF - zero-order filter, DM - dichroic mirror, O - objective, MEA - microelectrode array. (B) **Example projections of test images onto a fluorescent surface.** Scale bars represent  $200 \mu\text{m}$ .

### 3 MATERIALS AND METHODS

manner. The time course of light presentation was controlled with transistor-transistor-logic (TTL) squared voltage pulses, applied with the power1401 digital/analog converter.

#### **Contributions to the Implementation of the Illumination System**

The installation of the holographic illumination system as well as the development of a graphical user interface software (amongst others laser controls, holographic pattern generation and image acquisition) were accomplished by Dr. Martin Both, Dr. Felix Friedl, Dr. Jan-Oliver Hollnagel, Dr. Pascal Geschwill and Martin E. Kaiser. Figure 3.5 A was designed by Dr. Martin Both and modified by Martin E. Kaiser.

#### **3.5.2 Immunocytochemistry and Confocal Imaging**

Following electrophysiological recordings, slices were fixed in paraformaldehyde (PFA; Sigma-Aldrich, Steinheim, Germany), diluted to 1 % in 0.1 M phosphate buffer (pH = 7.4), at 4 °C overnight. After fixation, slices were stored in phosphate buffered saline (PBS; in mM: 137 NaCl, 2.7 KCl, 8 NaH<sub>2</sub>PO<sub>4</sub>, 2 KH<sub>2</sub>PO<sub>4</sub>; pH = 7.2) at 4 °C. The subsequent staining procedure was performed as follows. Slices were washed in PBS 3x for 15 min, each before and after incubating slices in blocking solution for 2 h at room temperature. Blocking solution (5 % normal goat serum (NGS; Vector Laboratories, Burlingame, USA) with 0.5 % Triton X-100 (Merck, Darmstadt, Germany)) served to block unspecific antibody binding sites. Primary antibodies (rabbit anti  $\beta$ -IV spectrin) were provided by Dr. Maren Engelhardt (Institute of Neuroanatomy, Medical Faculty Mannheim, CBTM, Heidelberg University, Germany). They were diluted 1:1000 in primary antibody solution (0.2 % Triton X-100 and 1 % NGS in PBS) and applied to the slices. After an overnight incubation period at room temperature, slices were again washed 3x for 15 min in PBS. Next, we used avidin, Alexa Fluor 488 conjugate (Molecular Probes, Schwerte, Germany; excitation wavelength = 493 nm, emission wavelength = 519 nm) to render intracellular biocytin visible. Avidin non-

### 3.5 *Illumination and Microscopy*

covalently binds to biocytin, which allowed us to image the Alexa conjugate. Additionally, we applied the CY3 antibody (goat, anti rabbit; Dianova, Hamburg, Germany; excitation wavelength = 552 nm, emission wavelength = 570 nm) against the  $\beta$ -IV spectrin primary antibody. Secondary antibodies were also diluted in antibody solution. Slices were then incubated in both secondary antibodies at room temperature, and again washed 3x for 15 min each. Finally, the histology mounting medium containing 4',6-Diamidin-2-phenylindol (DAPI; Fluoroshield with DAPI; Sigma-Aldrich) was used, which allowed us to improve the preservation of fluorescence and to counterstain for deoxyribonucleic acid (DNA).

For anatomical analysis cells were imaged with a Nikon A1R confocal microscope. We used objectives with magnification factors 10 (Nikon Plan Apo  $\lambda$  10x NA 0.45 [numerical aperture = 0.45, working distance = 4mm, field of view at zoom 1 = 1.27 x 1.27mm]), 40 (Nikon Plan Fluor 40x NA 1.3 oil immersion [numerical aperture = 1.3, working distance = 0.2mm, field of view at zoom 1 = 0.32 x 0.32mm]) or 60 (Nikon N Apo 60x NA 1.4  $\lambda$  oil immersion [numerical aperture = 1.4, working distance = 0.14 mm, field of view at zoom 1 = 0.21 x 0.21mm]).

### **Contributions to Immunocytochemistry and Confocal Imaging**

Immunocytochemistry and detailed confocal imaging were performed by Nadine Zuber, Lucie Landeck and Martin E. Kaiser, aided by Tina Sackmann as well as Dr. Maren Engelhardt.

### **3.5.3 Calcium Imaging**

In order to measure intracellular calcium dynamics of large groups of cells in the hippocampal network, we used the synthetic fluorescent calcium indicator Oregon Green BAPTA 1-acetoxymethyl ester (OGB-1; Molecular Probes; excitation wavelength = 494 nm, emission wavelength = 523 nm). Solid OGB-1 was dissolved in Pluronic F-127 (20 % in DMSO, Molecular Probes) and diluted in calcium free Ringer's solution (in mM: 150NaCl,

### 3 MATERIALS AND METHODS

2.5 KCl, 10 HEPES (Carl Roth, Karlsruhe, Germany)). For bolus loading (Garaschuk et al., 2006; Tsien, 1981) of OGB-1 into CA1 strata pyramidale and radiatum (Pfeiffer et al., 2014), a glass electrode with an opening of about 2-3  $\mu\text{m}$  was back-filled with the OGB-1 solution. After slight tissue penetration, gentle pressure was applied for about 5 min, which caused a release of OGB-1 into the slice. OGB-1 could then diffuse across cell membranes due to its acetoxymethyl ester group, which was cleaved and thus trapped the OGB-1 inside the cells. Dye loading was performed under normal gas supply (95 %  $\text{O}_2$  and 5 %  $\text{CO}_2$ ). Following a 60 min incubation period, calcium imaging in conjunction with field potential recording in hippocampal CA1 was performed under hypoxia (95 %  $\text{N}_2$  and 5 %  $\text{CO}_2$ ). Laser light (wavelength = 489 nm; Toptica iBeam Smart; Toptica Photonics, Muenchen, Germany) excited OGB-1. We employed a custom-built fluorescence microscope with a CSU-X1 Nipkow-type spinning-disk (1800 rpm, Yokogawa) to image a large field of view (410 x 410  $\mu\text{m}$ ; Reichinnek et al. 2012). Fluorescent light was sampled through a dry objective (Olympus LMPlanFL N 20x [numerical aperture = 0.4]) by an electron-multiplying charge-coupled device (EMCCD) camera (Image EM C9100-13; Hamamatsu, Herrsching am Ammersee, Germany) at 31.9 Hz. Both, a dichroic mirror (486 - 491 nm; Yokogawa, Ratingen, Germany) and an emission filter (525  $\pm$  18 nm; Chroma, Olching, Germany) separated excitation and emission wavelength, to detect a conclusive signal. Slice movement artifacts, caused by hypoxia, were corrected manually during imaging procedure.

#### **Data Analysis and Statistics**

For off-line analysis, only slices that showed spontaneously occurring SPW-Rs prior to and post OGB-1 bolus loading were included. With the aid of ImageJ we obtained pixel intensity values per imaged frame of a defined 40 x 40  $\mu\text{m}$  region of interest (ROI) of the CA1 pyramidal cell layer. Intensity values were then analyzed by applying custom-written MATLAB routines. We subtracted background fluorescent intensity and calculated shown intensity values as percentage change from baseline conditions. Their intensity



### *3.5 Illumination and Microscopy*

values were obtained from 60 s of continuous imaging immediately before the induction of hypoxia. Data were tested for statistical significance of differences with the nonparametric Wilcoxon's signed-rank test.



## 4 Results

### 4.1 Privileged Recruitment of Axon-Carrying Dendrite Pyramidal Cells in CA1 during Sharp Wave-Ripple Complexes *in vitro*

#### 4.1.1 SPW-R-Entrained Spiking Behavior Correlated to Cellular Anatomy

The field potential signal of hippocampal SPW-Rs represents the defined co-activity of multiple neurons. These are thought to be selectively activated in reliable and reverberating patterns, which are proposed to be the basis for complex information encoding in neuronal circuits (Hebb, 1949). Different recruitment mechanisms of single cells into these neuronal ensembles have been suggested so far (Bahner et al., 2011; Draguhn et al., 1998; Hebb, 1949; Memmesheimer, 2010; Schmitz et al., 2001). However, the exact mechanisms are still unknown.

Here, we aimed for a further understanding of the selective activation of single pyramidal cells within neuronal ensembles. As a model system, we used spontaneously occurring SPW-Rs in 400  $\mu\text{m}$  thick horizontal hippocampal mouse brain slices. We conducted

## 4 RESULTS

standard field potential measurements in conjunction with intracellular sharp electrode recordings in the proximal and distal hippocampal area CA1, respectively (figures 4.1 and 4.2; Bahner et al. 2011; Maier et al. 2003). During recordings, single pyramidal cells were filled with biocytin to stain them afterwards. In order to enable a sufficient biocytin filling, cells were recorded for at least 25 minutes. In addition, stainings for the AIS marker  $\beta$ -IV-spectrin allowed the observation of axon locations and therefore a classification of recorded neurons in two anatomical classes (figure 4.3; Thome et al. 2014).

### **Pyramidal Cell Spiked Within SPW-Rs Selectively**

Bahner et al. (2011) described two functionally distinct subgroups of CA1 pyramidal cells during SPW-R oscillations, either eliciting APs or remaining silent within SPW-Rs. In accordance with their findings, we observed that a subgroups of principal neurons spiked within SPW-Rs (figure 4.1 B, C), namely participating cells. The waveform of APs occurring within SPW-Rs appeared ectopic-like, which suggested that they were generated in the axon, subsequently backpropagating into the soma (figure 4.1 C, D; Bahner et al. 2011). The typical antidromic AP waveform was further shown by the second temporal derivative, which depicted a clear latency separation between two spike components (figure 4.1 D, red), separating the spike generation in the AIS and the subsequent somatodendritic charging (Bahner et al., 2011).

In contrast, the second pyramidal cell group remained silent during network-entrained inputs, namely nonparticipating cells (figure 4.2; Bahner et al. 2011). The somatic membrane potential of these cells was hyperpolarized by SPW-R-driven inputs (figure 4.2 C; Bahner et al. (2011)). Interestingly, it has further been shown that even strong somatic current injection fails to induce AP firing of nonparticipating pyramidal cells within SPW-Rs (Bahner et al., 2011). In our recordings, these cells were only capable of eliciting APs outside of SPW-Rs.

#### 4.1 Privileged Recruitment of AcD Pyramidal Cells in CA1 during SPW-Rs *in vitro*

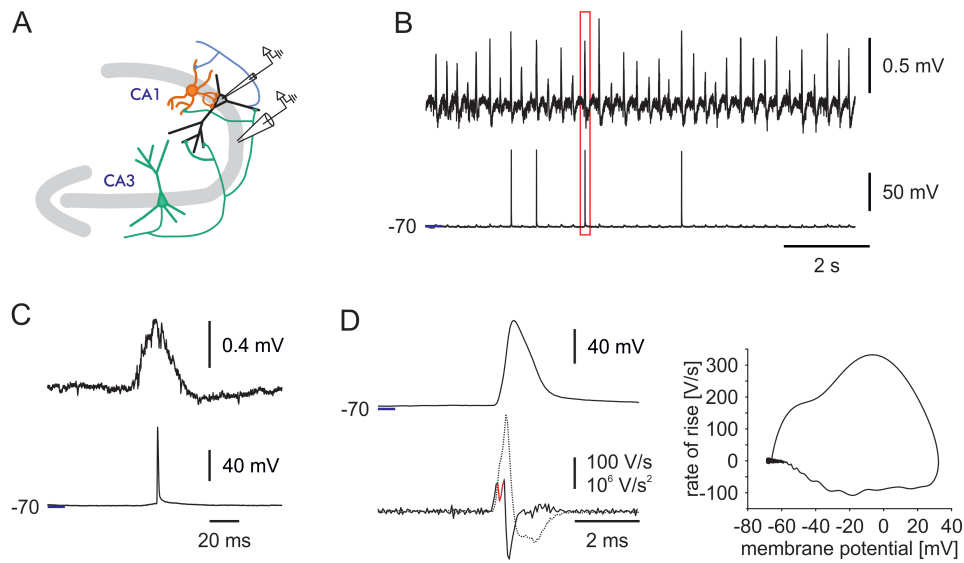


**Figure 4.1: Representative network-entrained spiking of a single CA1 pyramidal cell during SPW-R oscillations.**

**(A) Scheme of the experimental setup.** Intracellular voltage deflections from CA1 pyramidal cells were recorded in conjunction with field potential recordings in CA1 stratum pyramidale. **(B) and (C) Original field potential (upper traces) and intracellular recordings (bottom traces).** (B) Selective AP-firing of the shown cell during SPW-Rs. The cell was participating in SPW-R oscillations (participating cell). (C) Expanded traces from B (red rectangle), showing an ectopic-like AP within a SPW-R. Note the missing slow depolarization before the steep rising phase. **(D) Left top:** Zoomed-in view of the AP shown in C. **Left bottom:** Corresponding first (dotted line) and second (solid line) temporal derivative of the shown AP waveform. Note the prominent dent (red) in the latter one, reflecting the latency between spike generation in the AIS and following somatodendritic charging, which is typical for ectopic spikes. **Right:** Phase plot (dV/dt versus V) of the AP shown in B, C and D. A negative shift of SPW-R-driven AP threshold could be observed, in comparison to APs outside SPW-Rs (see figure 4.2).  $n_{\text{AcD cells}} = 18$ .  $n_{\text{nonAcD cells}} = 17$ .

The resulting nonparticipating APs depicted a canonical waveform, which was characterized by a continuous rise of the second temporal derivative (figure 4.2 D; Bahner et al. 2011). In general, APs induced by somatic current injections as well as spontaneously generated ones outside SPW-Rs mimicked a canonical waveform, in both participating and nonparticipating cells (figure 4.2 D; Bahner et al. 2011).

## 4 RESULTS

Moreover, the comparison of participating and nonparticipating APs did not only reveal differences in the waveform but also in the membrane potential upon AP initiation. Participating, ectopic-like APs showed a negatively shifted membrane potential as compared to nonparticipating APs (figures 4.1 D and 4.2 D, respectively; Bahner et al. 2011).

According to our observations, the participating cells represented approximately 25 % of all recorded CA1 principal neurons.

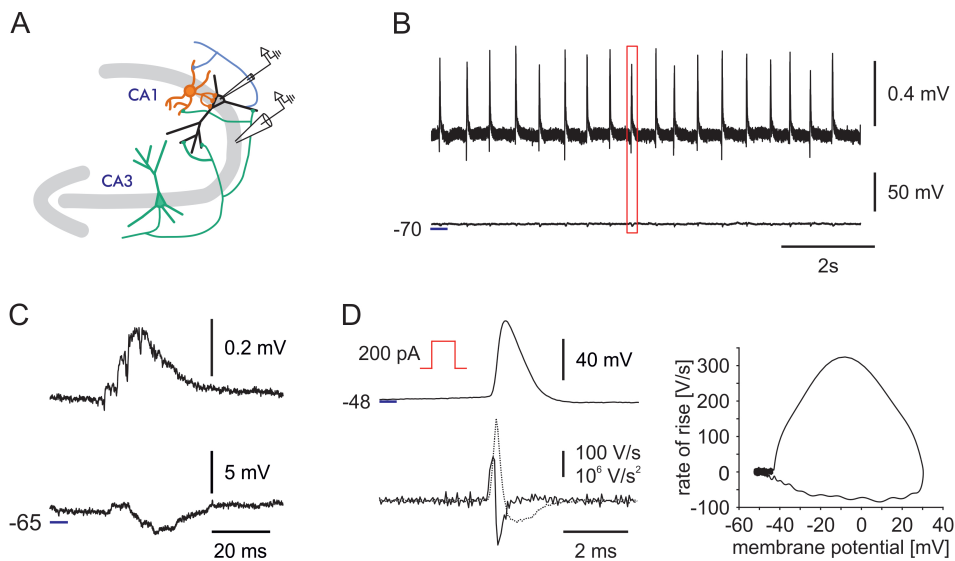


**Figure 4.2: Representative network-entrained hyperpolarization of a single CA1 pyramidal cell during SPW-R oscillations.**

**(A) Scheme of the experimental setup.** Intracellular voltage deflections from CA1 pyramidal cells were recorded in conjunction with field potential recordings in CA1 stratum pyramidale. **(B) and (C) Original field potential (upper traces) and intracellular recordings (bottom traces).** (B) Hyperpolarization of the shown cell during SPW-Rs. No spontaneous APs were observed within SPW-Rs. The cell was not participating in SPW-R oscillations (nonparticipating cell). (C) Expanded traces from B (red rectangle), showing an SPW-R-entrained hyperpolarization of the intracellular membrane potential. **(D) Left top:** Induced AP outside SPW-Rs, subsequent to 200 pA somatic current injection. **Left bottom:** Corresponding first (dotted line) and second (solid line) temporal derivative of the shown AP waveform. Note the continuous rising phase in the latter one, which is typical for orthodromic APs, missing a prominent dent. **Right:** Phase plot (dV/dt versus V) of the induced AP shown in D. Current-induced AP threshold was not shifted towards negative membrane potentials, as opposed to APs within SPW-Rs (see figure 4.1).  $n_{AcD\ cells} = 18$ .  $n_{nonAcD\ cells} = 17$ .

#### 4.1 Privileged Recruitment of AcD Pyramidal Cells in CA1 during SPW-Rs *in vitro*

### CA1 Pyramidal Cells Depicted a Dendritic Axon Origin

With respect to the anatomy of hippocampal CA1 pyramidal cells, Thome et al. (2014) showed a peculiar positioning of the axon in a portion of cells. Axons of approximately 50 % of CA1 pyramidal cells derive from dendritic compartments, which led to the name axon-carrying dendrite (AcD) cells. The excitability of axon-carrying dendrites is enhanced as compared to regular basal dendrites (Thome et al., 2014). The axons of the other half of CA1 pyramidal cells originate from the soma, therefore these cells were coined non-axon-carrying dendrite (nonAcD) cells. In line with Thome et al. (2014), we were able to classify about 49 % of all identified CA1 pyramidal cells as AcD neurons (figure 4.3;  $n_{\text{AcD cells}} = 29$ ,  $n_{\text{nonAcD cells}} = 30$ ).

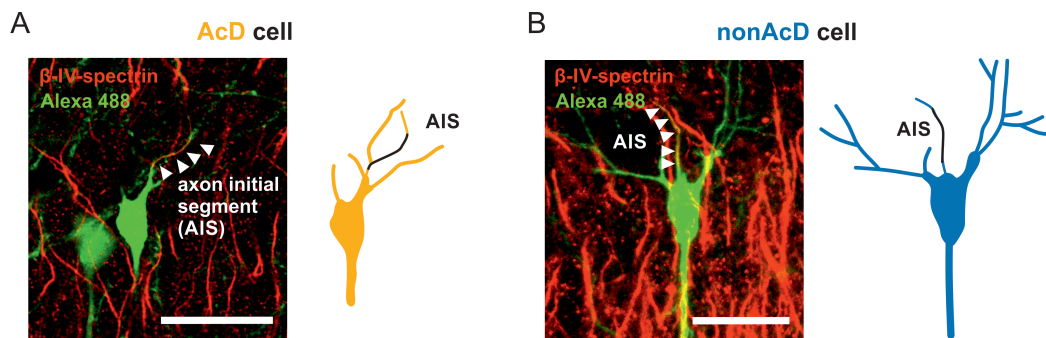


**Figure 4.3: CA1 pyramidal cells constituted two distinct anatomical groups. (A) and (B) Immunocytochemistry of two representative examples.**

*Left:* Images represent a maximum intensity projection of consecutive confocal imaging pictures. Cells were filled with biocytin through the sharp electrode and stained with Alexa Fluor 488 (green). The axon initial segment (AIS) was visualized by staining against the AIS marker protein  $\beta$ -IV-spectrin (red). The AIS is pointed out by white arrow heads. *Right:* Anatomical tracings of confocal images on the left. The axons are shown in black. Scale bars represent 40  $\mu\text{m}$ . **(A) Axon-carrying dendrite (AcD) cell.** Note, that the axon derived from a basal dendrite. **(B) Non-axon-carrying dendrite (nonAcD) cell.** The axon of the representative nonAcD cell originated from the soma.

### Correlation between AcD Anatomy and SPW-R-Entrained Spiking

Strikingly, our combined efforts in recording pyramidal cells intracellularly and post-hoc anatomy analyses revealed that solely AcD cells represented participating cells during

## 4 RESULTS

SPW-R oscillations (figure 4.4; two-tailed chi-squared test,  $P < 0.0001$ ). This potentially implies so far not considered effects on single cell activation in neural networks. While the aforementioned SPW-R-entrained ectopic-like APs were exclusively elicited by AcD cells, all recorded nonAcD cells remained silent within SPW-Rs, always representing nonparticipating neurons. However, not all but 14 of 28 AcD cells (50 %) were recruited into SPW-R ensembles (figure 4.4).

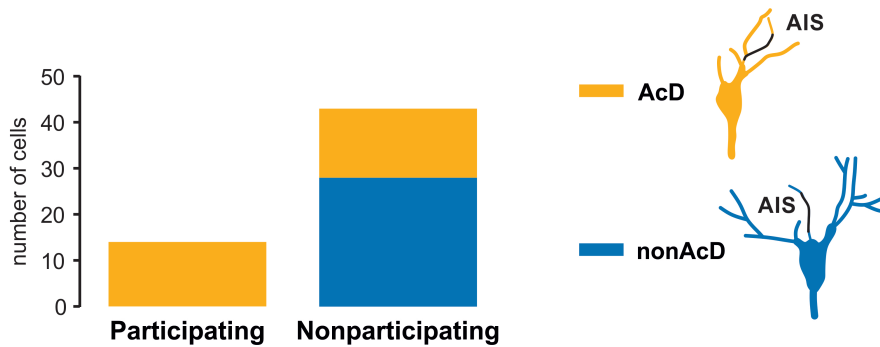


**Figure 4.4: Axon location indicated the SPW-R-entrained spiking behavior of targeted CA1 pyramidal cells.**

Cells were classified according to their respective anatomy (AcD or nonAcD) as well as to their SPW-R-entrained spiking behavior (participating or nonparticipating). Anatomical quantifications of AcD (yellow) or nonAcD (blue) cells are color-coded. In our recordings only AcD cells elicited spontaneous APs within SPW-Rs ( $n_{\text{AcD cells}} = 14$ ), whereas nonAcD cells ( $n_{\text{nonAcD cells}} = 28$ ) remained silent, only capable of spiking outside SPW-Rs. Note that there was also a fraction of AcD cells that did not participate during spontaneous SPW-R oscillations ( $n_{\text{AcD cells}} = 15$ ). Two-tailed chi-squared test,  $P < 0.0001$ .

### AcD and NonAcD Cells Received Similar SPW-R-entrained Synaptic Inputs

Since we wanted to study the recruitment of single cells into neuronal ensembles, we next investigated the mechanisms causing observed selective spiking behavior of AcD and nonAcD cells. Differences in passive membrane properties between AcD as well as nonAcD cells could be excluded from possible explanations. The following data is shown as mean  $\pm$  SEM. The input resistance was not different between AcD and nonAcD cells (*AcD*:  $38.8 \pm 4.3 \text{ M}\Omega$ ,  $n = 18$ ; *nonAcD*:  $42.6 \pm 5 \text{ M}\Omega$ ,  $n = 17$ ;  $P = 0.3014$ ). The membrane potential decay time was also unchanged between AcD and nonAcD cells (*AcD*:  $11.5 \pm 1.3 \text{ ms}$ ,  $n = 18$ ; *nonAcD*:  $14.3 \pm 2 \text{ ms}$ ,  $n = 17$  each;  $P = 0.1791$ ).



#### 4.1 Privileged Recruitment of AcD Pyramidal Cells in CA1 during SPW-Rs *in vitro*

Another possible explanation for the observed spiking behavior could lie in a substantially greater excitatory SPW-R-driven input to participating cells, here shown to be only AcD cells, as compared to nonparticipating neurons, here shown to be AcD as well as nonAcD cells. Following this proposition, a pronounced excitation is expected to depolarize participating neurons above the hyperpolarizing impact of perisomatic shunting inhibition (Colgin, 2016), which affects pyramidal cells during SPW-R oscillations (Klausberger et al., 2003; Schlingloff et al., 2014). Hence, we analyzed SPW-R-entrained inputs onto individual AcD and nonAcD pyramidal cells, by calculating network-driven conductance changes. The obtained data are illustrated in table 4.1, presented as median and 25<sup>th</sup> as well as 75<sup>th</sup> percentiles and illustrated in figures 4.5, 4.6 and 4.7 ( $n_{\text{AcD cells}} = 18$ ,  $n_{\text{nonAcD cells}} = 17$ ). Statistical differences were calculated using the nonparametric Wilcoxon rank sum test.

In order to quantify and compare synaptic inputs, we adapted the conductance estimation methods described by Borg-Graham et al. (1998) and Priebe and Ferster (2005), which we already published in Maier et al. (2016). We calculated excitatory as well as inhibitory conductance changes during SPW-Rs. For achieving this, single pyramidal cells were targeted with sharp electrodes. SPW-R-driven membrane potential changes were recorded while applying somatic current injections in discrete steps. In following off-line analyses, we plotted the injected current steps to the respective cellular membrane potential responses for each time point over all occurring SPW-Rs. In this way, we were able to use the linear regression approach to calculate the slopes of the resulting straights over all SPW-Rs for each time point. The slopes represent the total SPW-R-driven conductance changes of a targeted pyramidal cell. From there on, we estimated the fraction of inhibitory and excitatory conductance changes, depending on the respective reversal potential of AMPA and GABA (for illustration see section 3.3.3, Borg-Graham et al. 1998; Priebe and Ferster 2005).

## 4 RESULTS

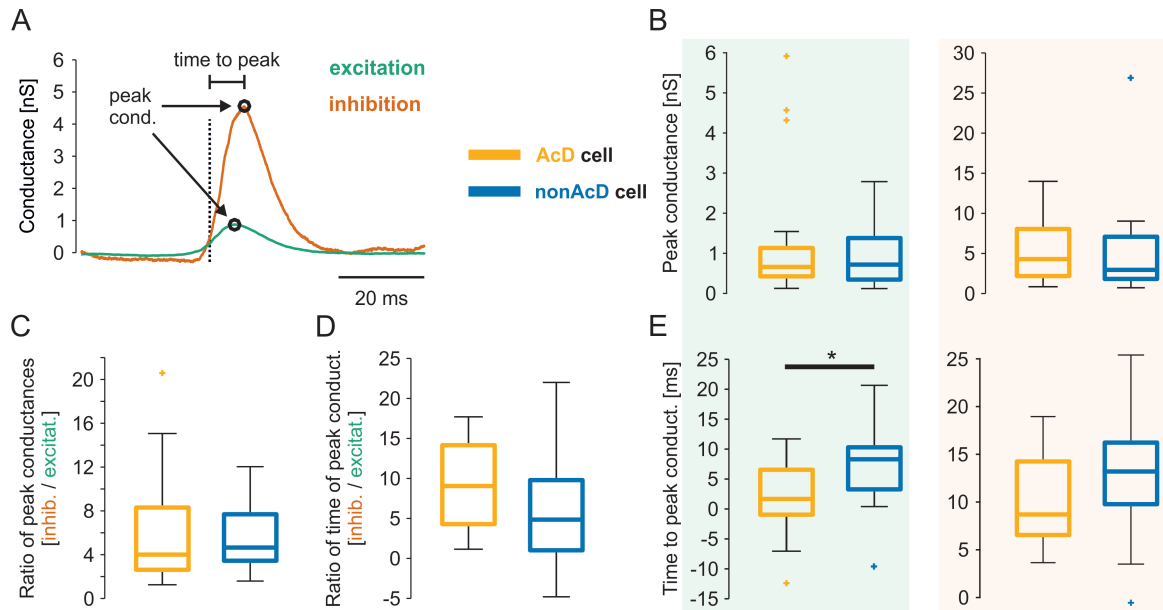


**Figure 4.5: AcD and nonAcD CA1 pyramidal cells received similar SPW-R-entrained peak conductance inputs but at different peak excitation times.**

**(A) Representative example of SPW-R-entrained excitatory (green) and inhibitory (orange) conductance changes.** Illustration for the following quantifications: Peak conductances were obtained as maximum conductance responses (indicated by black circles and arrows). Time to peak was calculated as the difference between the time point of the first sharp wave ripple before the sharp wave peak (dashed horizontal line) and the respective peak conductance (indicated by black circles and arrows). **(B)-(E) Quantifications of SPW-R-entrained conductance changes.** Characteristics of excitatory (highlighted in green) and inhibitory (highlighted in orange) inputs onto AcD (yellow) or nonAcD (blue) cells are illustrated as box plots. Colored boxes show the 25<sup>th</sup>, the 50<sup>th</sup> (median) and the 75<sup>th</sup> percentiles (from bottom to top, respectively). Black whiskers indicate the most divergent data points not considered outliers, while outliers are plotted by plus symbols. (B) SPW-R-induced peak excitatory (left) and peak inhibitory conductances (right) were not different between AcD and nonAcD cells. (C) Ratio of the peak conductances (inhibition / excitation) as well as (D) ratio of peak timings (inhibition / excitation) were also similar between both groups of cells. (E) Time to peak of excitatory (left) and inhibitory conductance evolutions (right). Note that the maximum of excitation occurred earlier in AcD than in nonAcD cells, as opposed the peak inhibition timing.  $n_{\text{AcD cells}} = 18$ .  $n_{\text{nonAcD cells}} = 17$ . Wilcoxon rank sum test. \* $P < 0.05$ .

Figure 4.5 A shows representative main excitatory (green) and inhibitory conductance changes (orange) of one cell. Our conductance quantifications revealed that spontaneous SPW-R-input provided higher inhibition than excitation to both AcD and nonAcD cells. Nevertheless, both cell groups received similar SPW-R-driven synaptic inputs.

#### 4.1 Privileged Recruitment of AcD Pyramidal Cells in CA1 during SPW-Rs *in vitro*

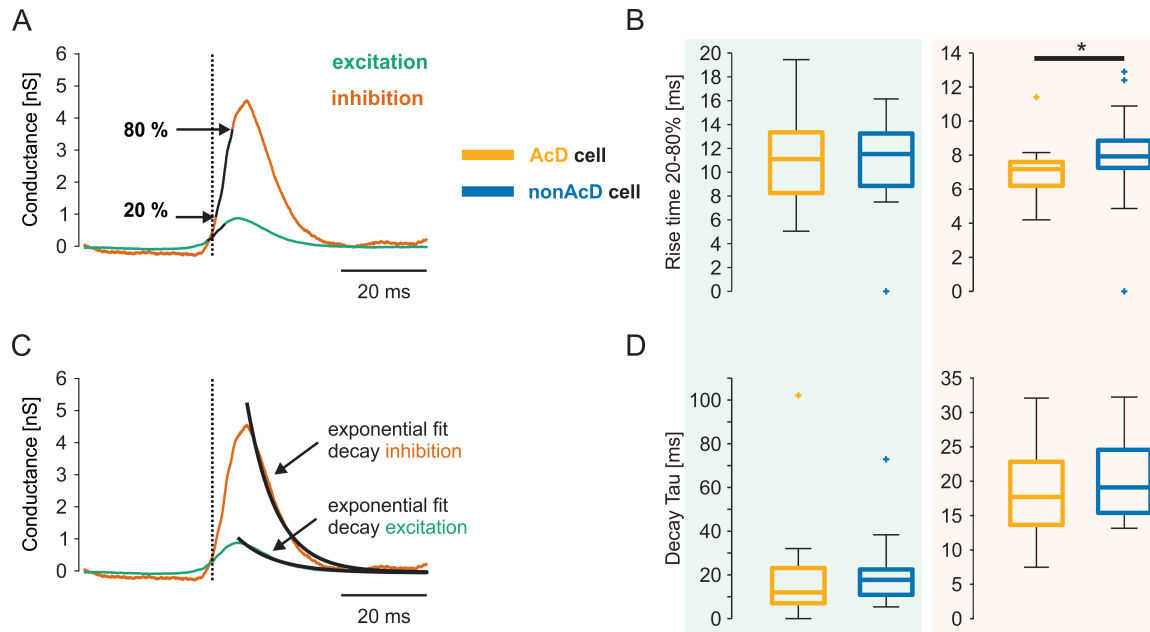


**Figure 4.6: AcD and nonAcD CA1 pyramidal cells received similar SPW-R-entrained conductance time courses but with different inhibitory rise times.**

**(A) and (C) Representative example of SPW-R-entrained excitatory (green) and inhibitory (orange) conductance changes.** Illustration for the following quantifications: (A) Rise time was calculated as the time difference between 20 % (lower black arrow) and 80 % (upper black arrow) of the respective conductance change (black components of the respective traces). Arrows are only illustrated for the inhibitory conductance change, however, analyses were performed for excitatory as well as inhibitory conductance evolutions. (C) Tau of the respective conductance decay was calculated from an exponential fit (black curves, pointed out by black arrows). **(B) and (D) Quantifications of SPW-R-entrained conductance changes.** Characteristics of excitatory (highlighted in green) and inhibitory (highlighted in orange) inputs onto AcD (yellow) or nonAcD (blue) cells are illustrated as box plots. Colored boxes show the 25<sup>th</sup>, the 50<sup>th</sup> (median) and the 75<sup>th</sup> percentiles (from bottom to top, respectively). Black whiskers indicate the most divergent data points not considered outliers, while outliers are plotted by plus symbols. (B) Rise time of excitatory (left) and inhibitory conductance evolutions (right). Note, that inhibition depicted a slightly steeper slope in AcD as compared to nonAcD cells. (D) Decay time of SPW-R-entrained excitation (left) and inhibition (right) revealed no differences between both groups of cells.  $n_{\text{AcD cells}} = 18$ .  $n_{\text{nonAcD cells}} = 17$ . Wilcoxon rank sum test. \*P < 0.05.

Peak excitatory as well as peak inhibitory conductances were not different between AcD and nonAcD cells (figure 4.5 B, table 4.1). Consequently, the median ratio of peak inhibitory to peak excitatory conductances was also similar in both groups (figure 4.5 C, table 4.1). However, we observed differences in time of peak excitation (figure 4.5 E, table 4.1). Excitatory SPW-R-driven input arrived 6.62 ms earlier in AcD than in nonAcD cells

## 4 RESULTS

(figure 4.5 E, table 4.1). This time to peak conductance was calculated relative to the first ripple in front the peak of the respective SPW-R. While the time point of strongest excitation differed between both groups of cells, we obtained no timing difference for peak inhibitory conductance changes (figure 4.5 E, table 4.1). The ratio of peak conductance timings (inhibition / excitation) was comparable in both groups of cells (figure 4.5 D, table 4.1). The time courses of both conductance changes were characterized by obtaining the rise and decay times, which are illustrated in figure 4.6. The rise time was specified as the time difference between 20-80 % of the respective conductance increase. The decay time on the other hand was calculated from the exponential fit of the declining conductance curves. Our analyses revealed that rise and decay times of excitatory conductance changes were similar between AcD and nonAcD cells (figure 4.6, table 4.1), as was the decay of inhibitory conductance changes (figure 4.6, table 4.1). However, the rise time of SPW-induced synaptic inhibition was observed to be 0.74 ms faster in AcD versus nonAcD cells (figure 4.6 B, table 4.1).

In a next step, we estimated the amount of sharp wave and ripple evoked conductance changes separately. In order to do so, the conductance changes were band-pass filtered (150-300 Hz; (figure 4.7). The filtered signal components were then subtracted from the original conductance evolution. In this way, we obtained *slow* and *fast* phasic conductance components (figures 4.7 A and C, respectively). We assessed the amount of the respective conductances by calculating the integral of the filtered curves of both components. Briefly, SPW-R oscillations resulted in comparable *slow* and *fast* conductance changes in AcD and nonAcD cells. The integrals of this decomposition in *slow* and *fast* phasic conductance components underlined the observed similarity of SPW-R-driven unfiltered synaptic inputs to AcD and nonAcD cells.

Summarized, spontaneous SPW-R-entrained inputs to AcD and nonAcD cells were similar to each other. Significant conductance differences between both groups of cells were only obtained with respect to the time to peak excitation and the rise time of inhibition, both being less in AcD as compared the nonAcD cells.

#### 4.1 Privileged Recruitment of AcD Pyramidal Cells in CA1 during SPW-Rs *in vitro*

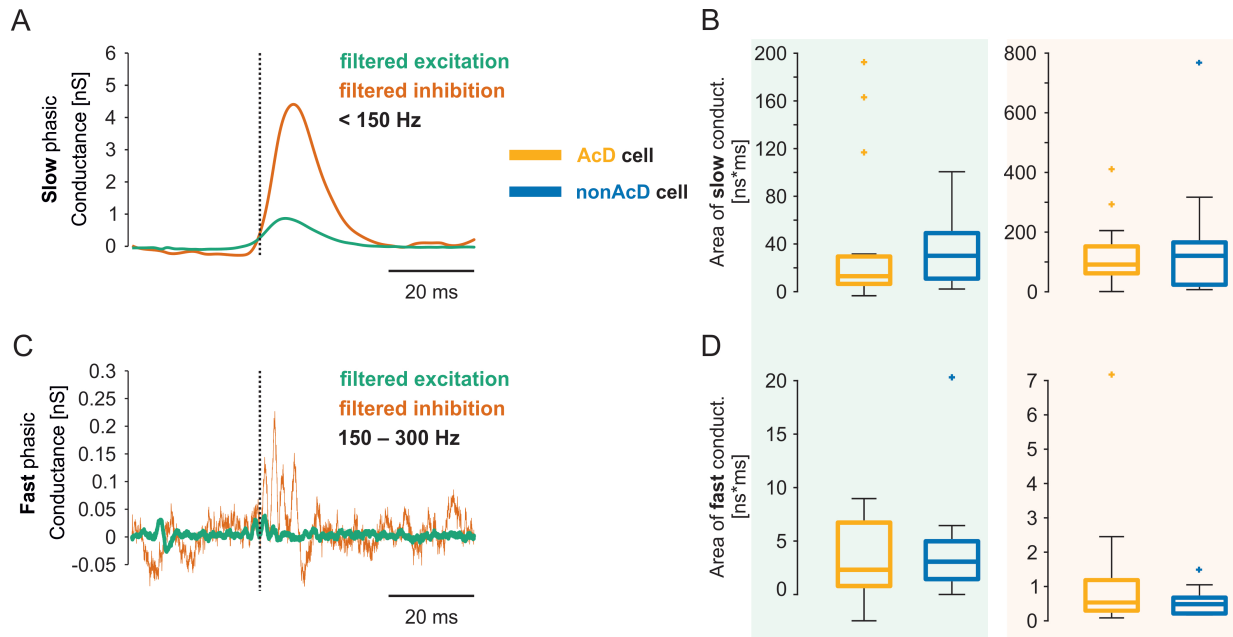


**Figure 4.7: AcD and nonAcD CA1 pyramidal cells received similar sharp-wave as well as ripple-entrained inputs.**

(A) and (C) Filtered examples of SPW-R-entrained excitatory (green) and inhibitory (orange) conductance changes. Originals can be seen in figure 4.6 A. Conductance changes were filtered and the integral of the resulting curves was calculated by trapezoidal numerical integration. (B) and (D) Quantifications of the *slow* and *fast* components of SPW-R-entrained conductance changes. Data of *slow* and *fast* excitatory (highlighted in green) and inhibitory (highlighted in orange) inputs onto AcD (yellow) or nonAcD (blue) cells are illustrated as box plots. Colored boxes show the 25<sup>th</sup>, the 50<sup>th</sup> (median) and the 75<sup>th</sup> percentiles (from bottom to top, respectively). Black whiskers indicate the most divergent data points not considered outliers, while outliers are plotted by plus symbols. (B) Integral of *slow* excitatory (left) and *slow* inhibitory conductance evolutions (right) were similar between AcD and nonAcD cells. (D) Integral of *fast* excitatory (left) and *fast* inhibitory conductance evolutions (right) were not different between AcD and nonAcD cells.  $n_{\text{AcD cells}} = 18$ .  $n_{\text{nonAcD cells}} = 17$ . Wilcoxon rank sum test. \* $P < 0.05$ .

The group-specific distinction of the timing to peak excitatory conductance changes indicates that dendritic input integration might rely on slower mechanisms in nonAcD cells. However, it can hardly explain the distinct SPW-R-driven spiking behavior of participating AcD versus nonparticipating nonAcD cells because the amplitude and the integral of observed conductance were comparable between both groups of cells. Likewise, the difference between AcD and nonAcD cells in inhibitory rise times in the microsecond range cannot explain a selective AP generation with SPW-Rs. Consequently, the here presented evi-

## 4 RESULTS

dence contradicts the prior described hypothesis that the pure strength of synaptic inputs defines the recruitment of individual cells into ensembles.

### Comparison to *in vivo* Data

Furthermore, in order to verify obtained conductance values, we compared our results to published *in vivo* data from Gan et al. (2017). Data is shown as mean  $\pm$  SEM. *In vivo*, peak excitation was  $1.8 \pm 0.4$  nS and peak inhibition was  $6.0 \pm 0.8$  nS (17 cells;  $P < 0.0001$ ; Gan et al. 2017). *In vitro*, we obtained  $1.15 \pm 0.22$  nS peak excitatory and  $5.12 \pm 0.85$  nS peak inhibitory conductances ( $n_{\text{AcD} + \text{nonAcD cells}} = 36$ ;  $P < 0.0001$ ). *In vivo* and *in vitro* excitatory and inhibitory conductances were similar to each other (unpaired t-test;  $P = 0.7164$  and  $P = 0.6492$ , respectively). Note that the inhibition to excitation ratio shows the tendency to be lower *in vivo* than in our *in vitro* approach (3.33 versus 4.45, respectively), indicating a relatively stronger inhibition *in vitro*. These ratios were calculated by dividing the overall mean, as opposed to the *in vitro* ratio shown in the table 4.1, which was calculated for each recording separately.

**Table 4.1:** SPW-R-entrained conductance features under baseline conditions

| Feature                       | Type   | Values   | P-value    |
|-------------------------------|--------|--|------------|
| Peak excitation<br>in nS      | AcD    | <i>median</i> = 0.66<br>[P25 = 0.42, P75 = 1.13] | P = 0.96   |
|                               | nonAcD | <i>median</i> = 0.72<br>[P25 = 0.34, P75 = 1.38] |            |
| Peak inhibition<br>in nS      | AcD    | <i>median</i> = 4.29<br>[P25 = 2.18, P75 = 8.05] | P = 0.609  |
|                               | nonAcD | <i>median</i> = 2.95<br>[P25 = 1.82, P75 = 7.08] |            |
| Peak ratio<br>(inhib./excit.) | AcD    | <i>median</i> = 4<br>[P25 = 2.62, P75 = 8.31]    | P = 0.8045 |
|                               | nonAcD | <i>median</i> = 4.65<br>[P25 = 3.45, P75 = 7.69] |            |

#### 4.1 Privileged Recruitment of AcD Pyramidal Cells in CA1 during SPW-Rs *in vitro*

|   |        |   |             |
|---|--------|---|-------------|
| <b>Time to peak<br/>in ms<br/>(excitation)</b>                | AcD    | <i>median = 1.68 ms</i><br>[P25 = -0.95, P75 = 6.55]  | *P = 0.0121 |
|   | nonAcD | <i>median = 8.3</i><br>[P25 = 3.28, P75 = 10.3]       |             |
| Time to peak<br>in ms<br>(inhibition)                         | AcD    | <i>median = 8.7</i><br>[P25 = 6.55, P75 = 14.25]      | P = 0.0774  |
|   | nonAcD | <i>median = 13.2</i><br>[P25 = 9.78, P75 = 16.22]     |             |
| Ratio peak time<br>(inhib./excit.)                            | AcD    | <i>median = 9.05</i><br>[P25 = 4.29, P75 = 14.15]     | P = 0.1252  |
|   | nonAcD | <i>median = 4.85</i><br>[P25 = 1.01, P75 = 9.79]      |             |
| Rise time<br>20-80 %<br>in ms<br>(excitation)                 | AcD    | <i>median = 11.1</i><br>[P25 = 8.25, P75 = 13.35]     | P = 0.7397  |
|   | nonAcD | <i>median = 11.53</i><br>[P25 = 8.85, P75 = 13.25]    |             |
| <b>Rise time<br/>20-80 %<br/>in ms<br/>(inhibition)</b>       | AcD    | <i>median = 7.18</i><br>[P25 = 6.2, P75 = 7.6]        | *P = 0.0227 |
|   | nonAcD | <i>median = 7.92</i><br>[P25 = 7.25, P75 = 8.85]      |             |
| Decay Tau<br>in ms<br>(excitation)                            | AcD    | <i>median = 12</i><br>[P25 = 7.02, P75 = 23.14]       | P = 0.2834  |
|   | nonAcD | <i>median = 17.74</i><br>[P25 = 10.88, P75 = 22.49]   |             |
| Decay Tau<br>in ms<br>(inhibition)                            | AcD    | <i>median = 17.71</i><br>[P25 = 13.65, P75 = 22.83]   | P = 0.2413  |
|   | nonAcD | <i>median = 19.1</i><br>[P25 = 15.39, P75 = 24.57]    |             |
| Integral of the<br>slow component<br>in mV·ms<br>(excitation) | AcD    | <i>median = 12.96</i><br>[P25 = 6.52, P75 = 29.50]    | P = 0.2038  |
|   | nonAcD | <i>median = 30.09</i><br>[P25 = 10.92, P75 = 49.12]   |             |
| Integral of the<br>slow component<br>in mV·ms<br>(inhibition) | AcD    | <i>median = 91.29</i><br>[P25 = 61.85, P75 = 152.16]  | P = 0.856   |
|   | nonAcD | <i>median = 120.59</i><br>[P25 = 23.67, P75 = 165.61] |             |

|  |        |  |            |
|--|--------|--|------------|
| Integral of the fast component in mV·ms (excitation) | AcD    | <i>median</i> = 0.53<br>[P25 = 0.3, P75 = 1.19]  | P = 0.3302 |
|  | nonAcD | <i>median</i> = 0.48<br>[P25 = 0.21, P75 = 0.68] |            |
| Integral of the fast component in mV·ms (inhibition) | AcD    | <i>median</i> = 2.32<br>[P25 = 0.8, P75 = 6.73 ] | P = 0.8301 |
|  | nonAcD | <i>median</i> = 3.07<br>[P25 = 1.44, P75 = 4.98] |            |

#### 4.1.2 A Working Hypothesis for Selective Network-Entrained Pyramidal Cell Activation, Based on the Position of the Axon

Our conductance analyses contradicted the proposition by some scholars that relatively stronger excitation to the participating group of cells enables them to uniquely participate in neuronal ensemble activity (Colgin, 2016). Therefore, we propose an anatomy-based recruitment mechanism of single cells into SPW-R ensemble activity (figure 4.8).

Briefly, during spontaneous SPW-R oscillations perisomatic inhibition, mediated by prominent PV<sup>+</sup> basket cell activity (Schlingloff et al., 2014), rhythmically hyperpolarizes the soma of pyramidal cells (English et al., 2014; Klausberger and Somogyi, 2008). Nevertheless, in the hippocampus, a portion of place cells elicit spikes during network-entrained events, leaving the question of the mechanistic principles unanswered. Consequently, ensembles of somehow privileged principal cells are able to overcome strong perisomatic shunting. We propose the following mechanistic explanation for the observed firing behavior of AcD CA1 pyramidal cells during SPW-R oscillations. A potential way to circumvent perisomatic shunting inhibition could be found in the positioning of the axon at a dendrite, as observed in AcD cells (figure 4.8 A). The AIS could thereby be both decoupled from the somatic compartment and receive direct dendritic input.



#### 4.1 Privileged Recruitment of AcD Pyramidal Cells in CA1 during SPW-Rs *in vitro*

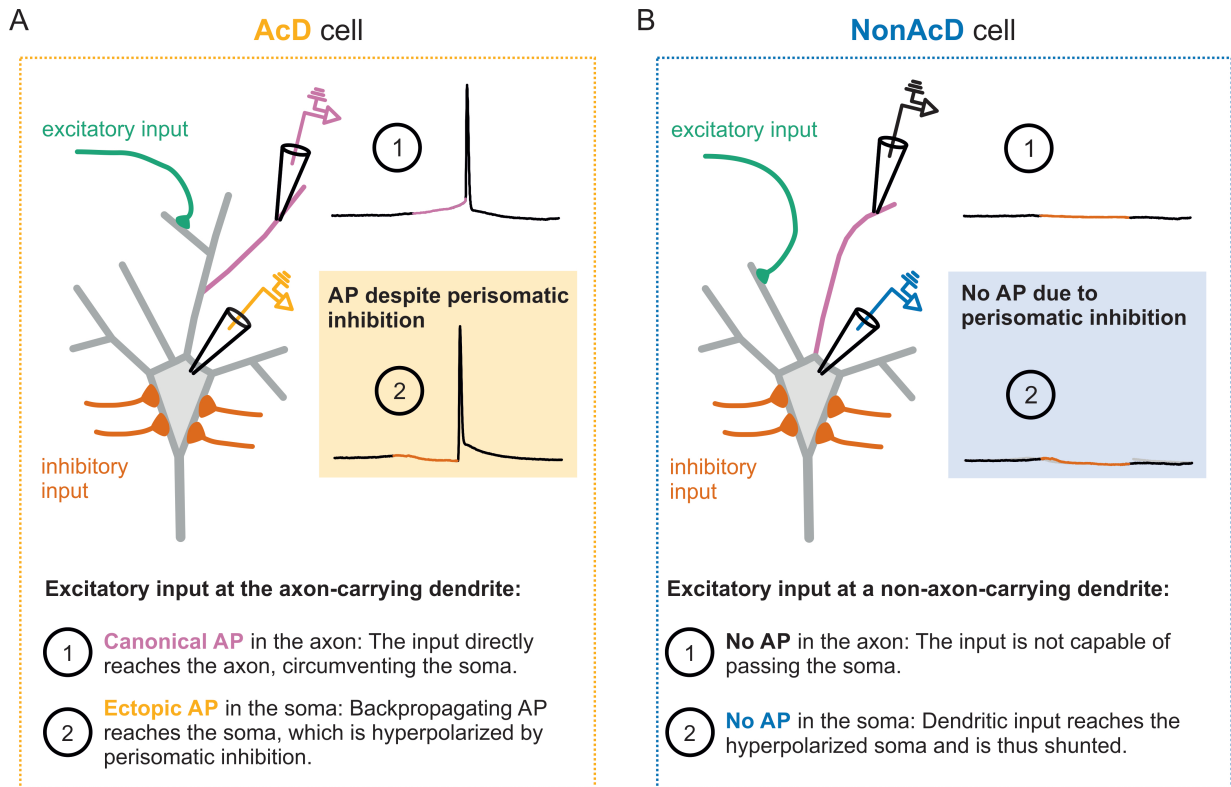


**Figure 4.8: Working hypothesis for selective AcD cell activation during hippocampal SPW-R oscillations.**

Mechanism explaining the observed distinct SPW-R-entrained spiking of AcD cells. It could constitute a basis for absent AP firing of nonAcD cells within SPW-Rs. Illustrated membrane potential deflections were modified from original recordings. We did not perform intracellular axonal recordings, these are meant to be hypothetical.

**(A) AcD cell input processing during SPW-Rs.** Upon excitation (green) of the axon-carrying dendrite, the resulting membrane potential depolarization transverses to the axon (rose) directly. The consecutive depolarization circumvents the somatic region. In the axon, the AIS depolarizes above threshold and thereby initiates a canonical AP (1), which propagates back to the soma. There, SPW-entrained perisomatic inhibition (orange) shifts the somatic membrane potential negatively (2), shunting the excitation at the perisomatic region. The incident back-propagating AP evokes a somatic AP by depolarizing the soma rapidly (ectopic-like AP, 2).

**(B) NonAcD cell input processing during SPW-Rs.** Upon excitation (green) of a non-axon-carrying dendrite, the resulting membrane potential depolarization cannot transverse to the axon (rose) directly. Instead, excitation has to pass the somatic region before reaching to the axon. In this way, the soma integrates synaptic inputs. At the soma, SPW-entrained perisomatic inhibition (orange) shifts the somatic membrane potential negatively (2). This shunts the network-driven excitatory postsynaptic potential, preventing it from transferring to the axon. Consequently, APs are neither observed at the soma (2) nor at the axon (1).

Excitatory inputs reaching an axon carrying dendrite could be integrated independently

## 4 RESULTS

of the soma and directly excite the AIS. Thereby, the somatic compartment would be circumvented. Cells in which the axon originates from a dendrite could meet these theoretical requirements. Hence, concurrent somatic inhibition, being observed during SPW-R oscillations, would have little influence on the output generation of the respective AcD cell.

In contrast, in nonAcD cells SPW-R-entrained perisomatic inhibition potentially has decisive consequences on the spontaneous AP generation (figure 4.8 B). The axons of nonAcD cells derive from the soma. Excitatory inputs to their dendrites are integrated in the soma and transversed to the axon. There, as soon as a critical membrane depolarization is reached, the AIS initiates AP firing. However, critical perisomatic inhibition shunts excitatory inputs, preventing network-driven pyramidal cell firing.

In the next steps, we provide evidence for the proposed working hypothesis by using two independent techniques, which are exclusively based on single cell manipulations.

### 4.1.3 Reduction of Perisomatic Inhibition Turned Silent Pyramidal Cells Into Participating Ones

Here, we present evidence that the positioning of the axon in conjunction with perisomatic inhibition are key regulators in including pyramidal cells into SPW-Rs. We selectively alleviated SPW-R-driven perisomatic inhibition to the targeted pyramidal cells by either pharmacologically blocking GABA<sub>A</sub> receptors or by applying dynamic clamp. Both approaches offered the advantage of leaving the network rhythms unchanged, only influencing the targeted cells. In section 4.1.2 we propose that only AcD cells are capable to circumvent SPW-R-entrained perisomatic silencing. Synaptic excitation to nonAcD cells on the other hand cannot bypass the soma and is thus shunted. According to this hypothesis, we expected that the abolishment of SPW-R-driven perisomatic inhibition by either blocking perisomatic GABA<sub>A</sub> receptors or by introducing an artificial conductance (dynamic clamp) affects the spiking behavior within SPW-Rs. As a consequence the observed selectivity of participating APs was presumed to be abolished. While only AcD cells

#### 4.1 Privileged Recruitment of AcD Pyramidal Cells in CA1 during SPW-Rs *in vitro*

elicited APs within SPW-Rs under baseline conditions, during diminution of perisomatic inhibition AcD as well as nonAcD cells were expected to elicit SPW-R-entrained APs.

#### Pharmacological Blockage of Perisomatic GABA<sub>A</sub> Receptors Reduced SPW-R-entrained Perisomatic Inhibition.

In order to obtain evidence for the aforementioned hypothesis, we aimed for a reduction of SPW-R-entrained perisomatic inhibition by first utilizing a pharmacological approach. We again recorded single pyramidal cells as well as standard field potential fluctuations in area CA1 of horizontal hippocampal brain slices. However, we dialyzed the targeted pyramidal cells with biocytin and the GABA<sub>A</sub> receptor antagonist picrotoxin (PTX, 1mM; Goutman and Calvo 2004; Inomata et al. 1988; Valero et al. 2017). PTX was dissolved in 2M KAc. Following intracellular recordings, we again stained for the intracellular biocytin and the indicator of the AIS,  $\beta$ -IV-spectrin. However, we were only able to classify a single cells according to its anatomy into AcD or nonAcD. The representative cell can be seen in figure 4.11 B and in table 4.2.

As expected, quantifications of network-entrained conductance changes revealed differences between intracellular application of picrotoxin versus sole KAc (baseline). The blockage of perisomatic GABA<sub>A</sub> receptors reduced the amplitude of inhibitory conductances as well as the ratio of inhibition to excitation (figure 4.9 B, C, respectively; table 4.2), while excitatory conductances were unaltered (figure 4.9 B, table 4.2). However, intracellular picrotoxin did not modulate decay times of excitatory and inhibitory conductance waveforms (figures 4.9 E, table 4.2). Moreover, we again decomposed obtained conductances into *slow* sharp wave-associated and *fast* ripple-related components (figures 4.10). In line with the altered peak conductance changes, picrotoxin dialysis also diminished the integral of *slow* and *fast* inhibitory components. However, as opposed to the inhibitory conductance components, both excitatory components were similar between dialysis of KAc and picrotoxin.

## 4 RESULTS

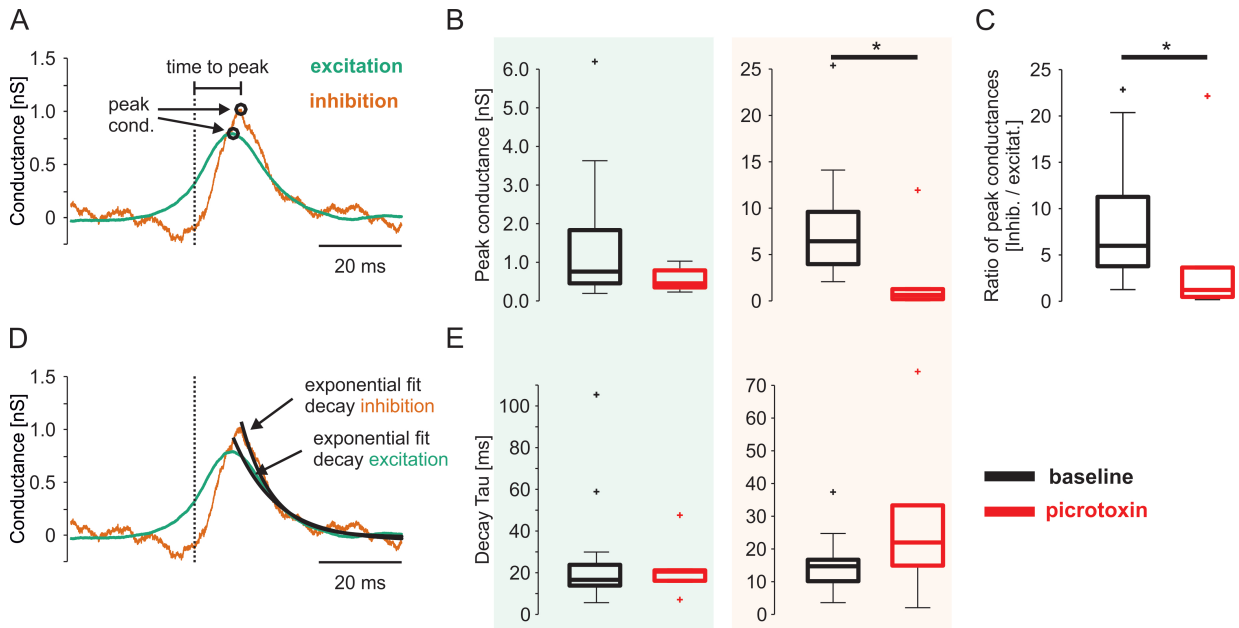


**Figure 4.9: Intracellular application of picrotoxin (1mM) reduced the peak of SPW-R-entrained inhibitory conductance changes of CA1 pyramidal cells.**

(A) and (D) Representative example of SPW-R-entrained excitatory (green) and inhibitory (orange) conductance changes, subsequent to intracellular picrotoxin dialysis. (A) Illustration of the quantifications in B and C: Peak conductances were obtained as maximum conductance responses (indicated by black circles and arrows). Time to peak was calculated as the difference between the time point of the first sharp wave ripple before the sharp wave peak (dashed horizontal line) and the respective peak conductance (indicated by black circles and arrows). (D) Illustration of the quantifications in E: Decay time of SPW-R-entrained conductances was calculated from an exponential fit (black curves, pointed out by black arrows). (B, C and E) Quantifications of SPW-R-entrained peak conductance changes. Characteristics of excitatory (highlighted in green) and inhibitory (highlighted in orange) inputs onto CA1 pyramidal cells, that were either filled with *KAc* (black) or *picrotoxin* (red) are illustrated as box plots. Recordings with *KAc* were termed *baseline* conditions. Colored boxes show the 25<sup>th</sup>, the 50<sup>th</sup> (median) and the 75<sup>th</sup> percentiles (from bottom to top, respectively). Black whiskers indicate the most divergent data points not considered outliers, while outliers are plotted by plus symbols. (B) SPW-R-induced peak excitatory conductance (left) was similar between *KAc* and *picrotoxin* filled cells. In contrast, peak inhibitory conductance (right) was different in both conditions, being reduced during dialysis of *picrotoxin*. (C) Ratio of the peak conductances (inhibition / excitation) was also decreased subsequent to intracellular *picrotoxin* application. (D) Decay time of SPW-R-entrained excitation (left) and (right) inhibition revealed no differences between *KAc* and *picrotoxin* filled cells.  $n_{\text{baseline}} = 25$ .  $n_{\text{PTX}} = 6$ . Wilcoxon rank sum test. \* $P < 0.05$ .

In figures 4.9 and 4.10 as well as in the table 4.2 quantifications are presented as median and 25<sup>th</sup> as well as 75<sup>th</sup> percentiles. We did not differentiate between AcD and

#### 4.1 Privileged Recruitment of AcD Pyramidal Cells in CA1 during SPW-Rs *in vitro*

nonAcD cells in the presented quantifications ( $n_{\text{baseline}} = 25$  and  $n_{\text{PTX}} = 6$ ). Statistical differences were calculated using the nonparametric Wilcoxon rank sum test.

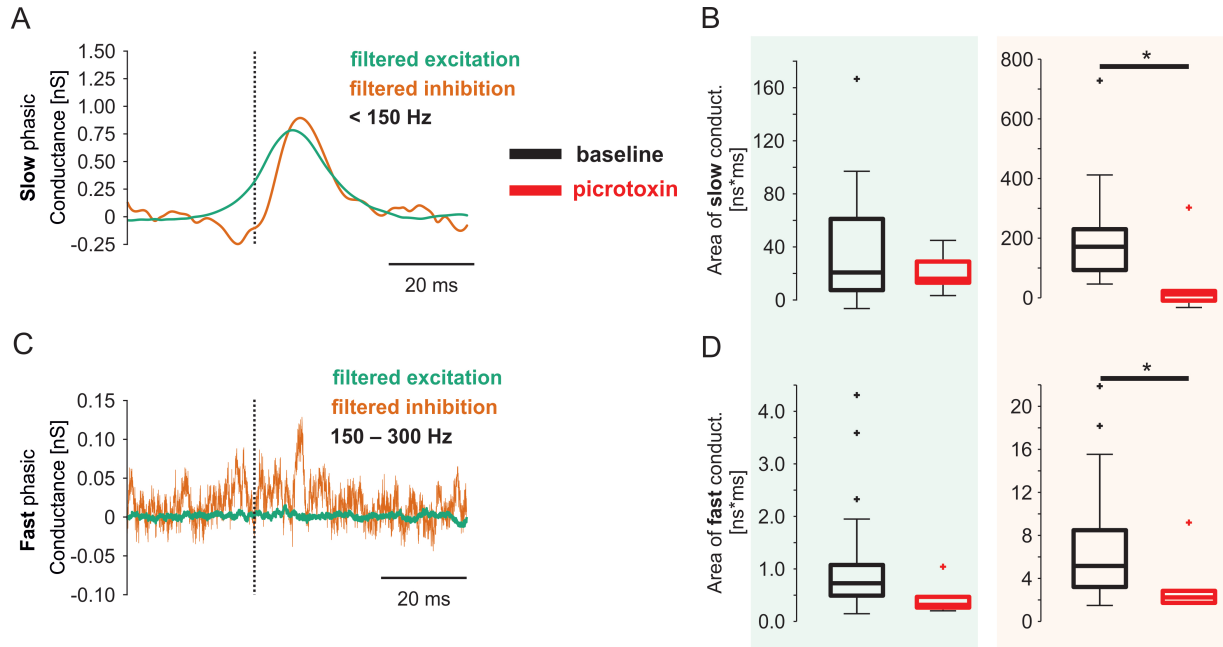


**Figure 4.10: Intracellular application of picrotoxin (1mM) diminished sharp wave- as well as ripple-entrained inhibitory conductances.**

(A) and (C) Filtered examples of SPW-R-entrained excitatory (green) and inhibitory (orange) conductance changes. Illustration of the quantifications in B and D: Originals (seen in figure 4.9 A). Conductance changes were filtered and the integral of the resulting curves was calculated by trapezoidal numerical integration. (B) and (D) Quantifications of the *slow* and *fast* components of SPW-R-entrained conductance changes. Characteristics of excitatory (highlighted in green) and inhibitory (highlighted in orange) inputs to CA1 pyramidal cells, that were either filled with *KAc* (black) or *picrotoxin* (red) are illustrated as box plots. Recordings with *KAc* were termed *baseline* conditions. Colored boxes show the 25<sup>th</sup>, the 50<sup>th</sup> (median) and the 75<sup>th</sup> percentiles (from bottom to top, respectively). Black whiskers indicate the most divergent data points not considered outliers, while outliers are plotted by plus symbols. (B) Integral of *slow* excitatory conductance evolution (left) was similar between *KAc* and *picrotoxin* filled cells. In contrast, *slow* inhibitory conductance change (right) was different between both conditions. (D) Integral of *fast* excitatory conductance (left) change was not different between both conditions. *Fast* inhibitory conductance evolutions differed between *KAc* and *picrotoxin* filled cells ( $n_{\text{baseline}} = 25$ .  $n_{\text{PTX}} = 6$ . Wilcoxon rank sum test. \* $P < 0.05$ ).

All in all, we were able to strongly diminish SPW-R-driven perisomatic inhibition onto the targeted pyramidal cells via intracellular dialysis of picrotoxin. Under baseline conditions, nonAcD cells could not elicit APs within SPW-Rs due to the shunting effect

## 4 RESULTS

of SPW-R-entrained perisomatic inhibition. However, picrotoxin reduced this inhibitory impact by reducing the peak conductance and the total amount of perisomatic inhibition. This leads to the assumption that the respective cells should have started to become participating in SPW-R oscillations.

**Table 4.2:** SPW-R-entrained conductance features during picrotoxin dialysis

| <b>Feature</b>  | <b>Type</b> | <b>Values</b>  | <b>P-value</b> |
|---|-------------|--|----------------|
| Peak excitation<br>in nS                                      | Baseline    | <i>median = 0.76</i><br>[P25 = 0.46, P75 = 1.83]       | P = 0.1273     |
|   | PTX         | <i>median = 0.45</i><br>[P25 = 0.35, P75 = 0.79]       |                |
| <b>Peak inhibition</b><br>in nS                               | Baseline    | <i>median = 6.43</i><br>[P25 = 3.97, P75 = 9.6]        | *P = 0.0074    |
|   | PTX         | <i>median = 0.64</i><br>[P25 = 0.19, P75 = 1.27]       |                |
| <b>Peak ratio</b><br>(inhib./excit.)                          | Baseline    | <i>median = 5.99</i><br>[P25 = 3.78, P75 = 11.27]      | *P = 0.0261    |
|   | PTX         | <i>median = 1.22</i><br>[P25 = 0.47, P75 = 3.65]       |                |
| Decay Tau<br>in ms<br>(excitation)                            | Baseline    | <i>median = 16.6</i><br>[P25 = 13.83, P75 = 23.8]      | P = 0.4685     |
|   | PTX         | <i>median = 20.55</i><br>[P25 = 16.14, P75 = 21.16]    |                |
| Decay Tau<br>in ms<br>(inhibition)                            | Baseline    | <i>median = 14.71</i><br>[P25 = 10.16, P75 = 16.72]    | P = 0.1542     |
|   | PTX         | <i>median = 21.98</i><br>[P25 = 14.92, P75 = 33.33 ms] |                |
| Integral of the<br>slow component<br>in mV·ms<br>(excitation) | Baseline    | <i>median = 20.74</i><br>[P25 = 7.43, P75 = 61.12]     | P = 0.7077     |
|   | PTX         | <i>median = 15.99</i><br>[P25 = 13.04, P75 = 28.97]    |                |
| <b>Integral of the slow comp.</b><br>in mV·ms<br>(inhibition) | Baseline    | <i>median = 171.31</i><br>[P25 = 93.15, P75 = 230.11]  | *P = 0.0074    |
|   | PTX         | <i>median = 11.64</i><br>[P25 = -9.37, P75 = 22.92]    |                |

#### 4.1 Privileged Recruitment of AcD Pyramidal Cells in CA1 during SPW-Rs *in vitro*

|   |          |   |             |
|---|----------|---|-------------|
| Integral of the fast component in mV·ms (excitation)    | Baseline | <i>median</i> = 0.7<br>[P25 = 0.49, P75 = 0.98]   | P = 0.068   |
|   | PTX      | <i>median</i> = 0.32<br>[P25 = 0.26, P75 = 0.47]  |             |
| <b>Integral of the fast comp.</b> in mV·ms (inhibition) | Baseline | <i>median</i> = 5.16<br>[P25 = 3.20, P75 = 8.48 ] | *P = 0.0483 |
|   | PTX      | <i>median</i> = 2.24<br>[P25 = 1.73, P75 = 2.84]  |             |

#### Pharmacological Blockage of Perisomatic GABA<sub>A</sub> Receptors Resulted in Spontaneous Canonical Action Potentials during SPW-Rs.

Indeed, picrotoxin dialysis for about 15 min resulted in canonical AP firing in a nonAcD cell during spontaneous SPW-Rs, upon mild current injection (50pA; figure 4.11 C and D). Mild current injection was necessary because we aimed to substitute pruned excitatory inputs to the targeted cell. Due to our *in vitro* approach, using hippocampal brain slices, network inputs to targeted cells were potentially pruned. In slices, the probability of excitatory dendritic inputs decreases with distance. The calculated AP derivatives in figure 4.11 D underlined the observed nonAcD anatomy of the respective cell. Accordingly, the second derivative misses the dent in the rising phase. Moreover, the canonical AP waveform was uncovered by computing the AP phase plot (figure 4.11 D). Since Bahner et al. (2011) report that even strong somatic current injections in nonparticipating cells failed to evoke APs within SPW-Rs, the here applied mild unspecific current injection was unlikely to be responsible for the observed network-entrained spiking behavior. Furthermore, 5 out of 6 pyramidal cells elicited SPW-R-entrained APs after dialysis of picrotoxin. The observed spiking of a nonAcD cells with SPW-Rs provided clear evidence that the sole blockage of perisomatic GABA<sub>A</sub> receptors resulted in spontaneous, network-driven somatic APs in nonAcD cells.

Consequently, the presented data suggests that the mere reduction of perisomatic in-

## 4 RESULTS

hibitory inputs was sufficient to cause network-entrained AP firing in nonAcD cells. However, pharmacological interventions potentially bear the disadvantage of, amongst others provoking unspecific or unknown side effects.

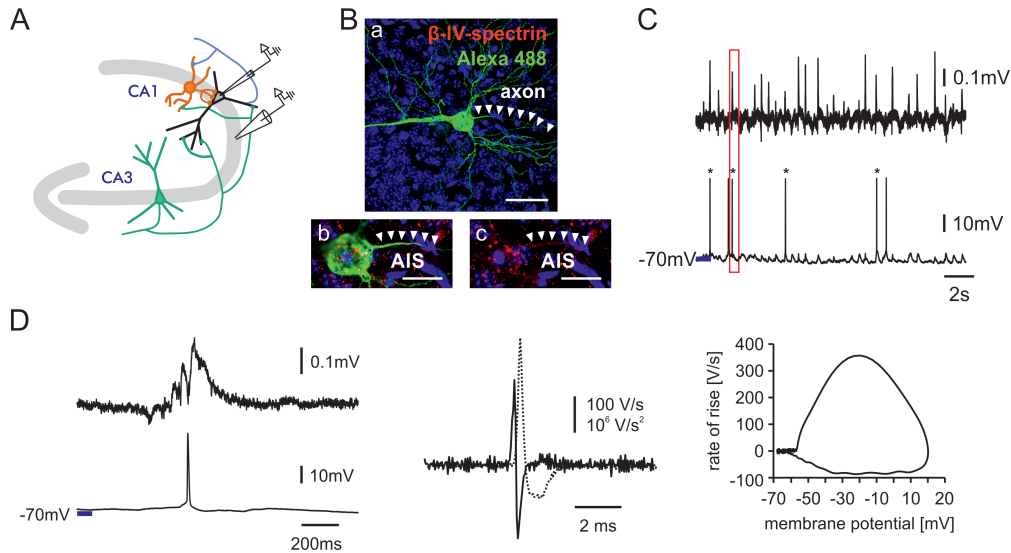


**Figure 4.11: Intracellular application of picrotoxin (1mM) resulted in spontaneous firing of canonical APs of nonAcD CA1 pyramidal cells during SPW-Rs.**

(A) **Scheme of the experimental setup.** Intracellular voltage deflections from CA1 pyramidal cells were recorded in conjunction with field potential recordings in CA1 stratum pyramidale. (B)-(D) **Original perisomatic anatomy as well as field potential and intracellular recordings from a single CA1 pyramidal cell.** (B) **Immunocytochemistry of a representative nonAcD cells.** Cell was filled with biocytin through the sharp electrode and stained with Alexa Fluor 488 (green). The axon initial segment (AIS) was rendered visible by staining against the AIS marker protein  $\beta$ -IV-spectrin (red). (a) the axon or (b) the AIS is pointed out by white arrow heads. Note, that the axon derived from the soma. Images represent a maximum intensity projection of consecutive confocal imaging pictures. Scale bars represent  $50 \mu\text{m}$  for (a) and  $20 \mu\text{m}$  for (b) and (c). (C) Selective AP-firing of the shown cell within SPW-Rs (marked by \*). The cell was participating in SPW-R oscillations, despite being a nonAcD cell. (D) Expanded traces from (C, red rectangle) showing a canonical AP within a SPW-R (left), subsequent to mild somatic current injection ( $50 \text{ pA}$ ). Corresponding first (dotted line) and second (solid line) temporal derivative of the shown AP waveform in D (bottom) (middle). Note the continuous rising phase in the second derivative, which is typical for orthodromic APs, missing a prominent dent. Phase plot ( $dV/dt$  versus  $V$ ) of the induced AP shown in D (right). Current-induced AP threshold was not shifted towards negative membrane potentials, similar to canonical AP shown in figure 4.2.

In our case, this constitutes a potential influence on the activity of single cells and thus their recruitment into neuronal ensembles. Hence, we used a second approach (dynamic



#### 4.1 Privileged Recruitment of AcD Pyramidal Cells in CA1 during SPW-Rs *in vitro*

clamp) to substantiate the presented findings.

#### **Dynamic Electrical Reduction of Perisomatic Inhibition Resulted in Spontaneous Canonical Action Potentials during SPW-Rs.**

We implemented a dynamic clamp system and an *in silico* model, which offers an alternative method to diminish the shunting effect of perisomatic inhibition on pyramidal cells (for illustration see section 3.3.4). In general, the dynamic clamp approach offers the possibility to insert an artificial synaptic conductance into a targeted neuron. Here, this additional conductance was supposed to counteract SPW-R-entrained perisomatic inhibition and thereby lead to spontaneous participating APs in the targeted pyramidal cell.

We thus processed this approach as follows. First, intracellular recordings of CA1 pyramidal cells and standard field potential recordings were performed as described in section 4.1.1. Inhibitory conductance changes were obtained from 40 SPW-Rs, providing an estimate of the perisomatic inhibition that the respective pyramidal cells received on average. In off-line analyses synaptic conductance changes were estimated and inhibitory as well as excitatory components were calculated (see sections 3.3.3 and 4.1.1). In parallel to these analyses, targeted cells were continuously recorded, to maintain penetration of the respective cell. This time course of the inhibitory conductance change over all 40 SPW-Rs was included in our *in silico* model, which then calculated the respective artificial synaptic conductance change that would annihilate the average SPW-R-entrained inhibitory conductance change. Next, we applied this simulated conductance change to the recorded cell, every time a spontaneous SPW-R occurred. Upon SPW-R input onto the targeted cell, a current that corresponded to the actual membrane potential and to the artificial conductance was applied via the intracellular recording electrode. In this way, we selectively diminished the network-entrained perisomatic inhibition of a single pyramidal cell on-line, thereby being cell as well as network specific. Indeed, the time course of the resulting average inhibitory conductance change was reduced and curtailed during dynamic clamp (figure 4.12 D, gray [baseline] vs. orange [dynamic clamping]). Moreover, estimations of

## 4 RESULTS

peak excitation, inhibition as well as their ration revealed a change due to electrical reduced on SPW-R-entrained perisomatic shunting.

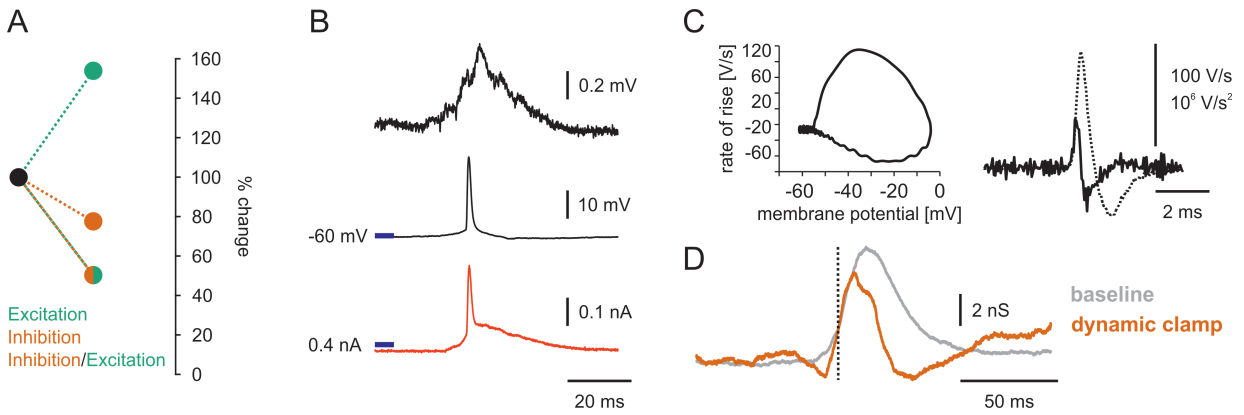


**Figure 4.12: Counteracting phasic inhibition with dynamic clamp resulted in canonical APs during SPW-Rs.**

**(A)-(D) Data from an example CA1 pyramidal cell recording.** (A) Calculated conductance changes during dynamic clamp, as compared to baseline. Peak excitatory conductance was increased (green filled circle) while peak inhibitory conductance (orange filled circle) as well as the inhibitory / excitatory ratio were decreased (orange and green filled circle). (B) Within a SPW-R (top) the targeted pyramidal cell elicited an AP (middle) potentially due to dynamic current injection, decreasing inhibitory inputs (bottom). (C) Phase plot (left;  $dV/dt$  versus  $V$ ) of the AP shown in B. AP threshold was not shifted towards negative membrane potentials (similar to the one in figure 4.2). Corresponding first (dotted line) and second (solid line) temporal derivative (right) of the shown AP waveform in B. Note the continuous rising phase in the second derivative, which is typical for orthodromic APs, missing a prominent dent. (D) Obtained SPW-R-entrained mean inhibitory conductance changes without (baseline; gray) and with (orange) dynamic clamp.

Amplitude of mean the perisomatic inhibitory conductance was reduced by 22.58 % (4.97 nA [baseline] vs. 3.85 nA [dynamic clamp]; figure 4.12 A, orange circle). In contrast, amplitude of median excitatory conductances increased by 52.68 % (0.93 nA [baseline] vs. 1.42 nA [dynamic clamp]), shifting the inhibition to excitation ratio to a favorable state (5.37 [baseline] vs. 2.71 [dynamic clamp]; figure 4.12 E, green circle and split green/orange circles respectively). The reason for the increased peak excitatory conductance might be found in the limited number of SPW-Rs and accompanied variations in SPW-R characteristics, that were used for conductance calculations. Data shown represent data from one cell only, therefore no further statistical analysis was performed. Nevertheless, these

#### 4.1 Privileged Recruitment of AcD Pyramidal Cells in CA1 during SPW-Rs *in vitro*

results appear to be promising. The recorded pyramidal cell exhibited SPW-R-entrained spiking upon reduction of network-driven shunting and medium current injection. Figure 4.12 B shows a spontaneously occurring SPW-R (top trace), the corresponding intracellular voltage deflection (middle trace) as well as the dynamically computed and applied current injection (bottom trace). As illustrated by the phase plot (figure 4.12 C) the participating AP exhibited a canonical waveform, which is confirmed by the second derivative of the AP waveform, missing a clear dent during the rising phase (figure 4.12 C; Bahner et al. 2011). Furthermore, according to data in section 4.1.1 this indicates that the recorded cell represented a nonAcD cell, which is in line with the finding that the targeted cell never participating in SPW-Rs during baseline recordings. Only the dynamic reduction of SPW-driven inhibition resulted in a participating spiking behavior.

Taken together, we showed that a dynamic reduction of network-entrained perisomatic shunting inhibition in conjunction with mild positive current injection resulted in AP firing during SPW-Rs. Thus, the dynamic clamp approach confirmed the evidence obtained by the pharmacological blockage of GABA<sub>A</sub> receptors, providing a promising tool for further pyramidal cells recordings.

All in all, in section 4.1 we presented a hypothesis and validating data that suggests an AcD-based recruitment mechanism of individual pyramidal cells into SPW-R ensemble activity. The described evidence potentially provides a function relation between the observed selective spiking network-entrained behavior *in vitro* and the axon location of CA1 pyramidal cells in the hippocampus.

## Contributions to the AcD Study

Data shown in section 4.1 were collected, analyzed and figures were designed by Martin E. Kaiser, aided by Paul Pfeiffer for section 4.1.3. Custom-made Matlab scripts were written by Martin Both and Martin E. Kaiser. Slice shown in figure 4.3 (A) was stained and imaged by Lucie Landeck. Martin Both, Paul Pfeiffer, and Martin E. Kaiser designed the

## 4 RESULTS

utilized model in section 4.1.3. Paul Pfeiffer generated the respective model and adapted the software, used for dynamic clamp recordings, presented in section 4.1.3.

## 4.2 Differential Modulation of Hippocampal Network Oscillations by Oxytocin *in vitro*

The coherent and repetitive activation of neurons plays a key role in memory formation and retrieval. The AcD-based recruitment mechanism of individual cells into memory encoding ensembles, shown in the last section, could be decisive during these processes. However, the formation of neuronal ensembles can potentially be additionally modulated by endogenous hormones. They might tune neuronal co-activation and therefore also network oscillations.

### 4.2.1 Oxytocin Receptor Activation Resulted in Reduced SPW-R Oscillations

Oxytocin appears to be widely present in the hippocampus, with oxytocin receptors being expressed in the CA area and the dentate gyrus (Hammock and Levitt, 2013; Mitre et al., 2016; Raam et al., 2017; Yoshida et al., 2009). While on the behavioral level facilitating long-lasting spatial learning (Tomizawa et al., 2003), on the single cell level oxytocin enhances the activity of fast-spiking inhibitory interneurons, thereby improving the fidelity of AP transmission (Owen et al., 2013). However, the apparently vital role in the modulation of information processing has so far not been shown on the level of neuronal network oscillations.

Here, we investigated whether the social hormone oxytocin modulates network-entrained ensembles rhythms. We recorded spontaneous SPW-Rs in the hippocampal area CA1 of horizontal mouse brain slices (Maier et al., 2003), using standard local field potential measurements. Prior to drug application, we obtained at least 5 min baseline SPW-R activity. For statistics, drug-induced effects were compared to these baseline recordings. Drugs were dissolved in ACSF and applied via global wash-in, affecting the entire slice. To guarantee

## 4 RESULTS

sufficient drug concentration in the tissue, drugs were supplied for at least 30 min before quantifying their observed impacts.

### Selective Oxytocin Receptor Activation by TGOT

Experiments performed by Pia Maier suggest that the oxytocin receptor antagonist (Thr<sup>4</sup>,Gly<sup>7</sup>)-Oxytocin H-Cys-Tyr-Ile-Thr-Asn-Cys-Gly-Leu-Gly-NH<sub>2</sub>; disulfide bond (TGOT) resulted in a decline of sharp wave and ripple characteristics, across a large range of concentrations (0.3-300 nM) (figure 4.13; Maier et al. 2016).

It has been published that at low concentrations TGOT targets oxytocin receptors selectively (Busnelli et al., 2013). However, at higher concentration TGOT is shown to also binds to AVP receptors (Busnelli et al., 2013). Oxytocin and arginine-vasopressin (AVP) receptors share a great structural similarity (Chini and Manning, 2007). Thus, certain ligands can potentially bind to both receptor types in a concentration dependent manner, which challenges the observed effects of TGOT on SPW-Rs. Hence, here we tackled the possible unspecificity of TGOT in OR binding by co-applying both the OR agonist TOGT (10 nM) and the specific OR antagonist OTRA (200 nM) to the slice during SPW-R oscillations. Figure 4.13 C illustrates that this co-application negated suppressing effects of TGOT alone. The following data is presented as mean  $\pm$  SEM. SPW-R amplitudes and ripple energies were even increased by  $9.7 \pm 4.7$  % and  $11.1 \pm 5.2$  %, respectively (SPW-R amplitude  $0.21 \pm 0.01$  mV [baseline] vs.  $0.23 \pm 0.02$  mV [TGOT + OTRA],  $P = 0.0476$  and ripple energy ( $0.29 \pm 0.03$  a.u. [baseline] vs.  $0.33 \pm 0.03$  a.u. [TGOT + OTRA],  $P = 0.0349$ ) (Maier et al., 2016). The abolishment of TGOT-mediated effects on SPW-Rs by the specific OR antagonist provides evidence that TGOT indeed specifically binds to ORs at low concentrations.

In order to exclude possible AVP receptor involvement in the observed TGOT-induced SPW-R modulations, next, we co-applied the AVP receptor antagonist V1ARA (300 nM) together with TGOT. Interestingly, the observed prominent SPW-R changes were comparable to the application of TGOT application alone (figures 4.13 A, D and Ha-d,  $n = 11$ ).

## 4.2 Differential Modulation of Hippocampal Network Oscillations by Oxytocin *in vitro*

SPW-R frequency and amplitude were reduced by  $19.6 \pm 4.8 \%$  ( $2.89 \pm 0.25$  Hz [baseline] vs.  $2.41 \pm 0.32$  Hz [TGOT],  $P = 0.0026$ ) and  $19.2 \pm 4.6 \%$  ( $0.44 \pm 0.05$  mV [baseline] vs.  $0.36 \pm 0.05$  mV [TGOT],  $P = 0.0016$ ), respectively. Ripple energy was decreased by  $16.3 \pm 2.1 \%$  ( $0.60 \pm 0.09$  a.u. [baseline] vs.  $0.50 \pm 0.08$  a.u. [TGOT],  $P = 0.0002$ ) and ripple frequency declined by  $2.7 \pm 0.6 \%$  ( $234 \pm 5$  Hz [baseline] vs.  $228 \pm 4$  Hz [TGOT],  $P = 0.0012$ ), whereas the number of ripple cycles was unchanged. The sole application of V1AR decreased the SPW-R amplitude. However, this effect was considered to correspond to the recording time and observed amplitude deterioration.

The presented data provided evidence that the observed TGOT-induced impacts of SPW-R characteristics were independent of AVP receptor activation. We were able to rescue oxytocin-induced reduction of SPW-R characteristics. Moreover, the combined activation of oxytocin and blockage of vasopressin receptors yielded results that were comparable to a sole oxytocin receptor activation.

### **Vasopressin Acted on Vasopressin as well as Oxytocin Receptors**

The so far suggested specificity of vasopressin at low concentrations might not be that specific after all. At concentrations used here, (Arg<sup>8</sup>)-Vasopressin (H-Cys-Tyr-Phe-Gln-Asn-Cys-Pro-Arg-Gly-NH<sub>2</sub> (vasopressin, 20 nM) was reported to activate AVP receptors specifically. However, evidence for that was shown in rats (Spoljaric et al., 2017). In contrast to Spoljaric et al. (2017), we present evidence that vasopressin partially acts on ORs at the applied concentration. Figures 4.13 A and F illustrate that in our hands the suggested selective activation of AVP receptors resulted in diminished SPW-R characteristics ( $P < 0.05$ ,  $n = 9$ ). The following data is presented as mean  $\pm$  SEM. SPW-R incidence was reduced by  $28.3 \pm 11.3 \%$  ( $2.76 \pm 0.26$  Hz [baseline] vs.  $2.06 \pm 0.43$  Hz [20 nM vasopressin],  $P = 0.0383$ ). SPW-R amplitudes were decreased by  $36.7 \pm 6.1 \%$  ( $0.30 \pm 0.03$  mV [baseline] vs.  $0.19 \pm 0.03$  mV [20 nM vasopressin],  $P = 0.0007$ ).

## 4 RESULTS

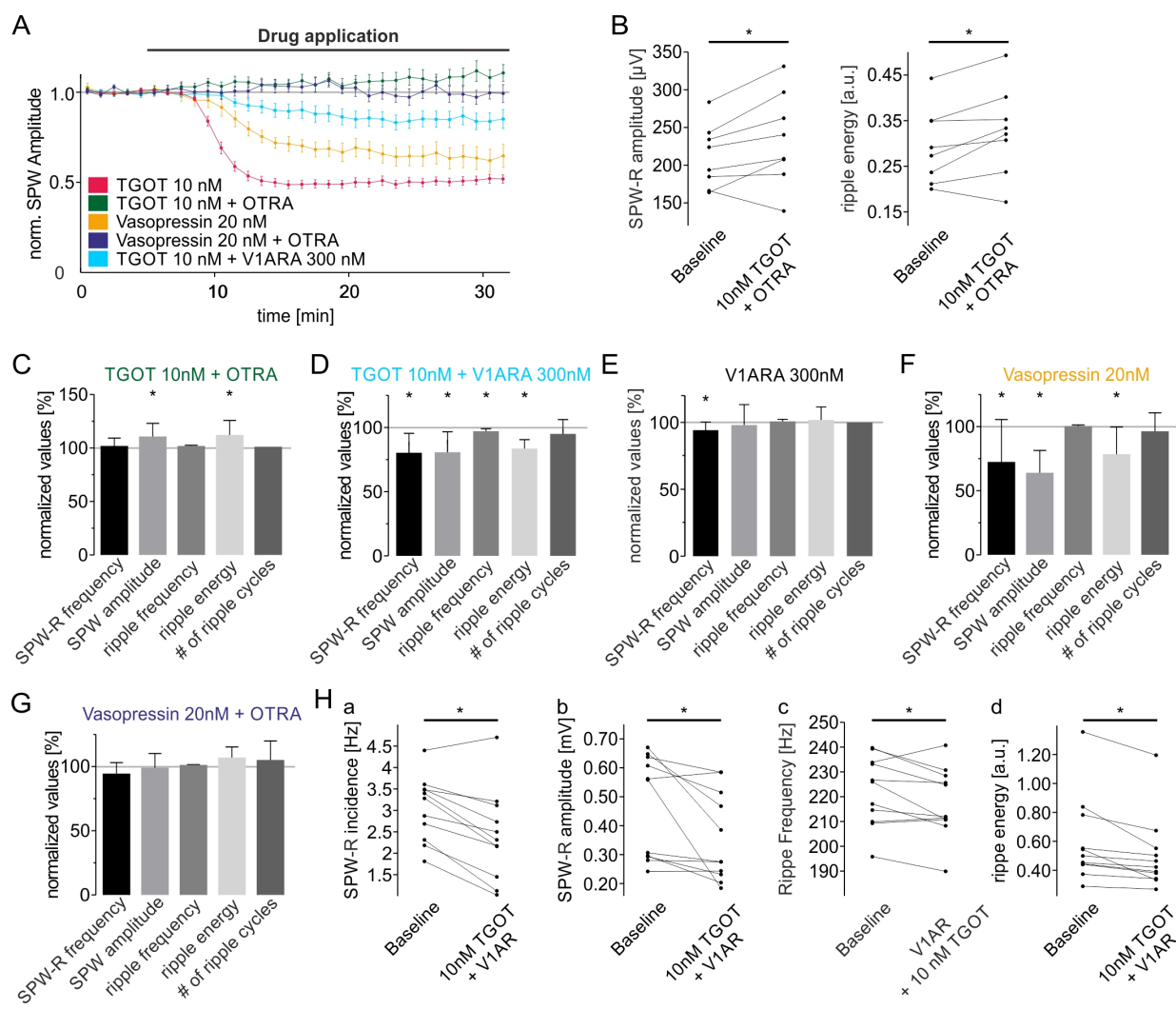


**Figure 4.13: Oxytocin receptor activation decreased SPW-R oscillations.**

(A): Time course of SPW-R amplitudes after drug applications. TGOT as well as vasopressin reduced SPW-R amplitudes. This reduction was either preserved or reversed during parallel blockage of AVP receptors, respectively. (B) Quantification of SPW-R characteristics before (baseline) and during application of TGOT (10 nM) and OTRA (200 nM). Applied in combination, OR agonist and antagonist increased SPW-R amplitude and ripple energy. (C)-(G) Normalized quantifications of the applied agonizing or antagonizing approaches. (C) TGOT (10 nM) and OTRA (200 nM) increased SPW-R amplitude and ripple energy. (D) TGOT (10 nM) and V1ARA (300 nM) diminished SPW-R amplitude and frequency as well as ripple energy. (E) V1AR (300 nM) decreased only SPW-R frequency. (F) Vasopressin (20 nM) diminished SPW-R amplitude and frequency as well as ripple energy. (G) Vasopressin (20 nM) and OTRA (200 nM) showed no modulation of SPW-R characteristics. (G) V1AR (300 nM) decreased only SPW-R frequency. (Ha-Hd) Quantification of SPW-R characteristics before (baseline) and during application of TGOT (10 nM) and V1AR (300 nM). (H) (a-d) SPW-R incidence, amplitude, ripple frequency as well as energy were decreased. \* $P < 0.05$ . Adapted from (Maier et al., 2016).



## 4.2 Differential Modulation of Hippocampal Network Oscillations by Oxytocin *in vitro*

Ripple energy was lowered by  $22.4 \pm 7.4$  % ( $0.35 \pm 0.04$  a.u. [baseline] vs.  $0.29 \pm 0.07$  a.u. [20 nM vasopressin],  $P = 0.0421$ ) (Maier et al., 2016). Hence, vasopressin mimicked TGOT regarding its effect on SPW-R oscillations (Maier et al., 2016).

A similar impact of the putative specific oxytocin or vasopressin receptor activation could result from unspecific vasopressin to AVP binding in mice, as Spoljaric et al. (2017) presents evidence from experiments with rat tissue. We investigated this by activating AVP receptors at the reportedly selective concentration (Spoljaric et al., 2017) while blocking ORs. Together, vasopressin (20 nM) and OTRA (200 nM) yielded no changes of SPW-R characteristics (figure 4.13 A and G).

At large, the presented data suggests that vasopressin resembled the effect of TGOT on SPW-Rs because of a co-activation of oxytocin receptors. According to our data, activation of oxytocin but not VAP receptors modulated SPW-R characteristics.

### 4.2.2 Oxytocin Receptor Activation Did Not Modulate Gamma Oscillations

After identifying an OR-dependent modulatory impact on hippocampal ensembles during SPW-R oscillations, we aimed at investigating whether oxytocin receptor activation disrupts SPW-Rs selectively or also other network oscillations. Hippocampal gamma oscillations are believed to fulfill specific functions in hippocampal input processing and memory formation. Here we investigated the modulatory potential of an OR activation on induced gamma rhythms. We tested the impact of the OR agonist TGOT on three different pharmacological and one optogenetic gamma models.

#### Pharmacologically Induced Gamma Oscillations

First, in experiments performed by Pia Maier, gamma oscillations were induced globally through wash-in of either carbamoylcholine chloride (carbachol,  $5 \mu\text{M}$ , figure 4.14 A; Fellous and Sejnowski 2000) or by application of (2S,3S,4S)-Carboxy-4-(1-methylethenyl)-

## 4 RESULTS

3-pyrrolidineacetic acid (kainate, 100 nM, figures 4.14 A and C; Fisahn et al. 2004). The following data is presented as mean  $\pm$  SEM. TGOT altered kainate-based gamma oscillations with respect to their amplitude, which was increased by  $11.3\% \pm 4.34\%$  ( $0.42 \pm 0.06$  mV [baseline] vs.  $0.47 \pm 0.07$  mV [TGOT],  $P = 0.0150$ ;  $n = 17$ , figure 4.14 E). The half width maximum was decreased by  $16.8 \pm 5.6\%$ , ( $20.1 \pm 1.6$  Hz [baseline] vs.  $17.3 \pm 2.4$  Hz [TGOT],  $P = 0.0305$ ;  $n = 17$ , figure 4.14 E). In contrast, TGOT did not modulate carbachol-induced gamma oscillations, as illustrated in figure 4.14 E(a-d). This difference in TGOT sensitivity of carbachol- and kainate-induced gamma models might be based on the activation of muscarinic acetylcholine receptors (mAChRs) in the first one. mAChRs are located at the pre- and postsynaptic site of neurons (Levey et al., 1991; Volpicelli and Levey, 2004). Activation of mAChRs can modulate parvalbumin-positive (PV<sup>+</sup>) inhibitory interneurons in a somewhat opposing manner. Presynaptic mAChRs diminish vesicular release from PV<sup>+</sup> interneuron terminals (Lawrence et al., 2015) whereas postsynaptic mAChRs depolarize PV<sup>+</sup> interneurons (Yi et al., 2015). Due to this likely interference of PV<sup>+</sup> inhibitory interneurons by mAChRs, they potentially influence the described gamma oscillations.

Therefore, we additionally utilized a third pharmacological gamma model. Whittington et al. (1995) showed that isolated networks of inhibitory neurons can generate oscillations in low gamma frequencies in pyramidal cells. For this, interneurons need to be activated tonically, which results in mutual inhibition, eventually leading to field potential oscillations in the gamma frequency range. In order to provide tonic excitation of interneurons, we applied the glutamate receptor agonist L-Glutamic acid monosodium salt hydrate (L-glutamic acid, 500  $\mu$ M) locally while globally blocking ionotropic glutamate receptors with 6-cyano-7-nitroquinoxaline-2,3-dione (CNQX, 10  $\mu$ M) and D(-)-2-Amino-5-phosphonopentanoic acid (D-APV, 30  $\mu$ M). CNQX represents an AMPA receptor antagonist while D-APV acts as a N-methyl-D-aspartate (NMDA) receptor antagonist. Thereby, interneurons were solely activated via metabotropic glutamate receptors, which are thought to drive the oscillation in the inhibitory network (Whittington et al., 1995).

## 4.2 Differential Modulation of Hippocampal Network Oscillations by Oxytocin *in vitro*

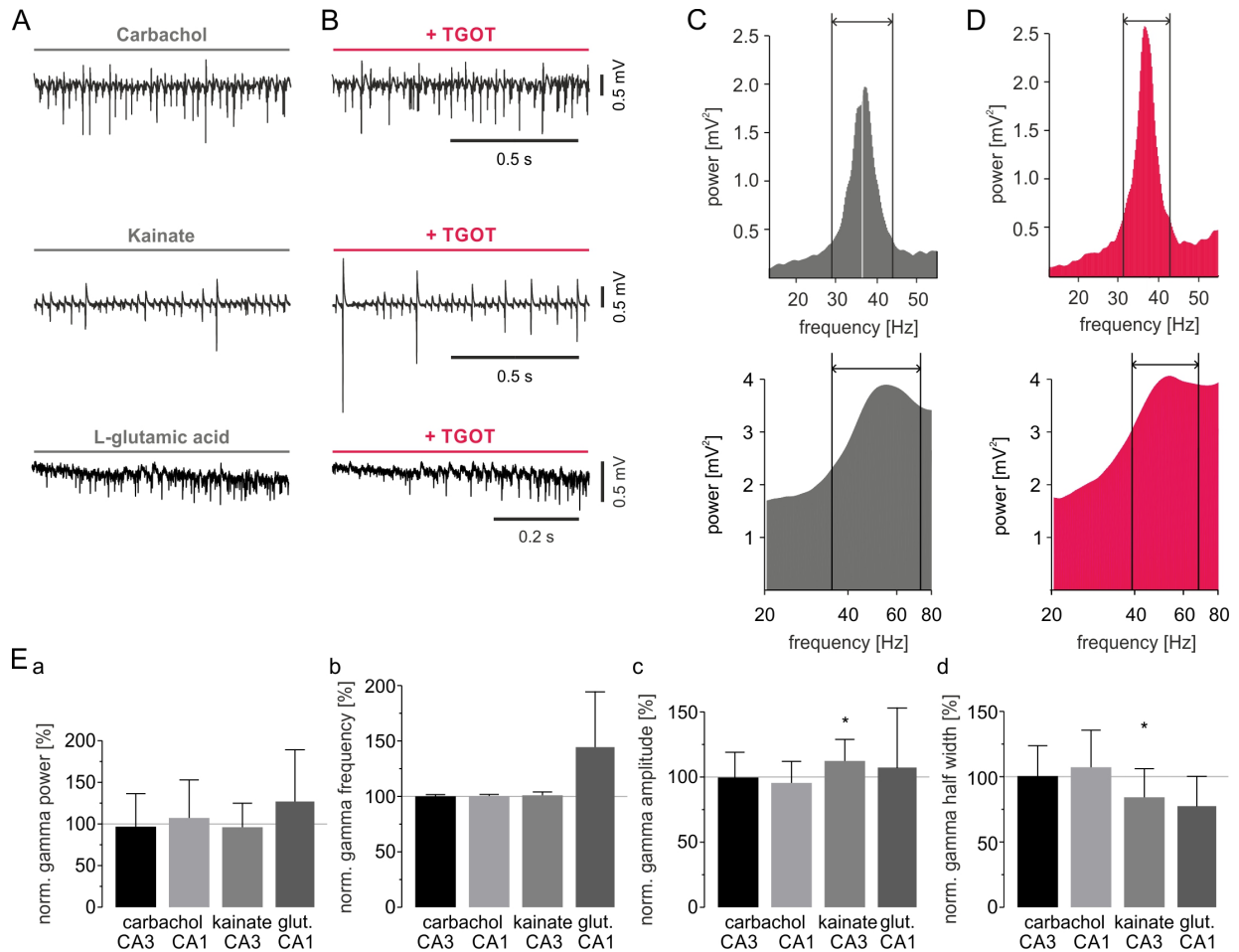


**Figure 4.14: TGOT marginally affected pharmacologically induced gamma oscillations.**

**(A)** and **(B)** Example traces of gamma oscillations during baseline TGOT (100 nM) condition, respectively. Carbachol-induced gamma oscillations (top), kainate-induced gamma oscillations (middle), L-glutamic acid-induced gamma oscillation (bottom). **(C)** and **(D)** Power spectra of gamma oscillations during baseline (gray) or TGOT condition (red). Kainate-induced gamma (top) and L-glutamic acid-induced gamma (bottom). **(E):** Normalized quantifications of gamma oscillation parameters following TGOT (100 nM) treatment. Gamma power (a) and frequency (b) were unchanged in all three gamma oscillation models. Apart from the kainate-induced gamma model, amplitude and half width maximum were also unaltered by TGOT (c - d) \* $P < 0.05$ . Adapted from (Maier et al., 2016).

L-glutamic acid was applied into the hippocampal area CA1, using a thin glass electrode, which was carefully lowered onto the slices. Upon glass to tissue contact, we observed oscillations in the gamma frequency range (see figure 4.14 A, C). In line with the previously

## 4 RESULTS

shown gamma models, this interneuron-based gamma was also insensitive to oxytocin receptor activation ( $n = 7$ ). The following data is presented as mean  $\pm$  SEM. Gamma power only showed a tendency to be decreased by  $26.86\% \pm 23.45\%$ , ( $0.0049 \pm 0.0014 \text{ mV}^2$  [baseline] vs.  $0.0046 \pm 0.0011 \text{ mV}^2$  [TGOT]), however, not statistically significant ( $P = 0.0655$ ). Gamma frequency tended to be increased by  $44.19\% \pm 18.88\%$ , ( $65.3844 \pm 7.8807 \text{ Hz}$  [baseline] vs.  $89.4103 \pm 6.2272 \text{ Hz}$  [TGOT];  $P = 0.1553$ ), similar to gamma amplitude, which was slightly increased by  $6.84\% \pm 17.19\%$ , ( $0.1205 \pm 0.0262 \text{ mV}$  [baseline] vs.  $0.1389 \pm 0.0305 \text{ mV}$  [TGOT];  $P = 0.7044$ ).

Strikingly, all employed pharmacological gamma oscillation models were largely insensitive to the application of the selective OR agonist TGOT. However, the shown gamma rhythm induction models are all based on additionally applied pharmacological receptor agonists. These might interfere with the ORs or AVP receptors, potentially intermingling with the investigated modulation impact of the selective OR activation.

### Optogenetically Induced Gamma Oscillations

In order to overcome potential deficits of the applied pharmacological gamma oscillation models, we applied optogenetics for gamma induction, in a next set of experiments. Akam et al. (2012) and Butler et al. (2016) describe that gamma oscillations can be locally generated in the hippocampus by slowly but consistently activating a large group of pyramidal cells. This action was performed with optogenetic tools. A purely optogenetic approach entails the advantage of circumventing drug-evoked neuromodulatory effects. For the selective and temporally defined activation of CA3 pyramidal cells, we implemented a holographic illumination system, based on a spatial light modulator (see section 3.5.1). By applying that system we were able to transmit light in a locally and temporally specific and well defined mode.

We recorded field potential fluctuations in the hippocampal area CA3 of horizontal mouse brain slices, expressing ChR2-eYFP under the CamKII $\alpha$  promoter (figure 3.4 in

#### 4.2 Differential Modulation of Hippocampal Network Oscillations by Oxytocin *in vitro*

section 3.4), which allowed for a restriction of ChR2 expression to excitatory pyramidal cells only (Wang et al., 2013). As opposed to prior sections, local field potential recordings were performed in submerged conditions (Hajos et al., 2009), using a microelectrode array, that comprised 60 extracellular electrodes (see section 3.3.5). Using the dual perfusion MEA (see section 3.3.5), the implemented recording system enabled spontaneous SPW-R oscillations to occur. In conjunction, confocal imaging, precise light presentation and MEA-based field potential recordings allowed us to perform the following experiments. Slices were placed on a MEA in a way that its recording electrodes were covered by most part of the hippocampal pyramidal cell layers. If SPW-R activity was observed optogenetic experiments were conducted. Then, we recorded a confocal image and tagged the location of light stimulation to hippocampal CA3 (figure 4.15 A). Confocal imaging provided the additional advantage of clear and high-resolving images of the respective tissue. Prior to light presentation this was needed to define the exact location that the light had to target. Gamma oscillations were recorded adjacent to the stimulation area. For off-line analyses we only used data from a single recording electrode from CA3 stratum pyramidale of each hippocampal slice. The negative potential deflection was possibly observed due to the light evoked cation influx into pyramidal cells, through ChR2 channels.

In contrast to theta nested characteristics of *in vivo* gamma oscillations (Belluscio et al., 2012), here optogenetically induced *in vitro* gamma oscillations lacked the theta component (figure 4.15 B and C). However, similar experiments that were conducted in an interface chamber (see section 3.3.1; Haas et al. 1979) revealed an underlying theta rhythm (data not shown). Further, *in vivo* cholinergic input has been shown to be crucial for shifting hippocampal activity states (Vandecasteele et al., 2014). As described at the beginning of this section, we conveyed that evidence to the *in vitro* situation in a separate set of experiments by applying carbachol as a structural analogue of acetylcholine (figure 4.14). Interestingly, in our optogenetic approach the exclusive activation of CA3 pyramidal cells by ChR2 was sufficient to induce gamma oscillations. Additional septal inputs were not evoked or simulated otherwise (figure 4.15 B and C).

## 4 RESULTS

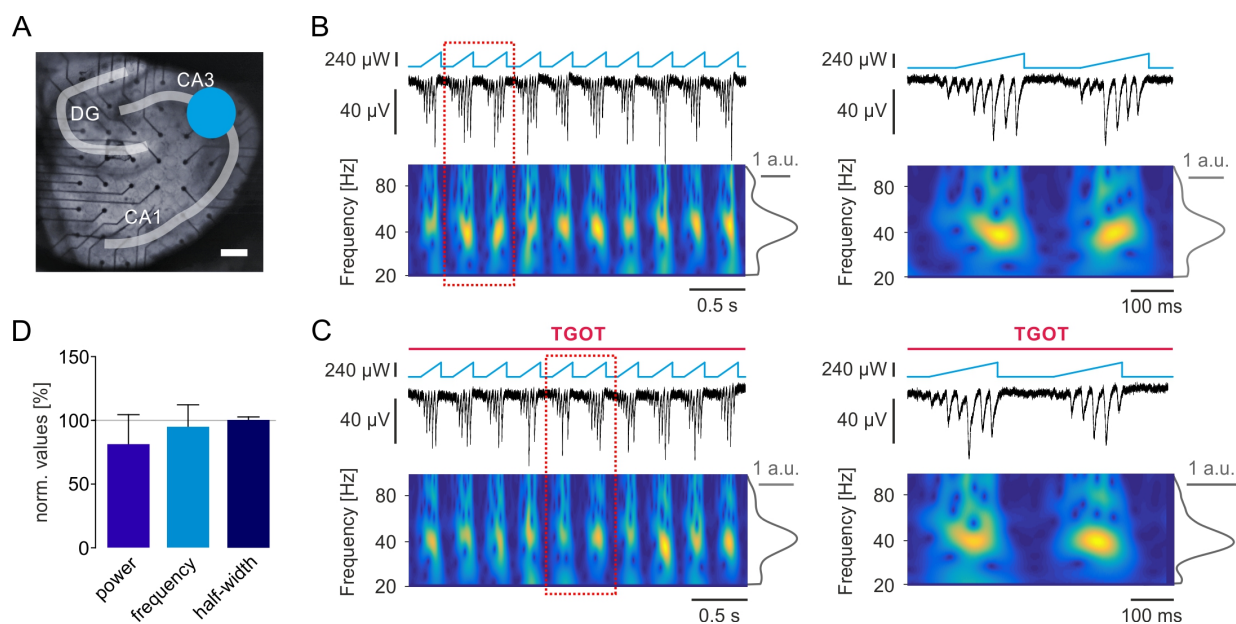


**Figure 4.15: Oxytocin receptor activation left light-induced nested gamma oscillations unchanged.** (A) Field of view, observed as a light microscopic image of a hippocampal brain slice recumbent on a MEA. Anatomical regions (DG, CA3 and CA1) as well as location of light stimulations (blue circle) are illustrated. Scale bar represents  $200 \mu\text{m}$ . (B) and (C) Examples of induced gamma oscillations, recorded in stratum pyramidale of CA1. (Top) Azure lines indicate intensity changes of the delivered light. (Middle) Raw local field potentials show periodic gamma oscillations. (Bottom) Wavelet spectra of the extracellular signals with respective frequency components. Mean frequency power distribution is indicated by the gray line (right side). (B) Gamma oscillations during baseline condition (right: expanded few pointed out by the red rectangle). (C) Gamma oscillations after TGOT (100 nM) application (right: expanded few pointed out by the red rectangle). (D) **Normalized quantification of gamma oscillations properties after TGOT (100 nM) application.** Gamma power, frequency and half width maximum were unchanged. Adapted from (Maier et al., 2016).

Theta-rhythmic (4 Hz) light presentation in a ramp-like pattern stimulated CA3 pyramidal cells and thus resulted in gamma oscillations ( $47.7 \pm 1.6$  Hz; figures 4.15 A, B and C), which spread to CA1. As soon as the light presentation was turned off, optogenetically induced gamma oscillations vanished and spontaneous SPW-Rs occurred. This is in line with hypotheses regarding the SPW-R generation, which appears to be a "default" activity state of the hippocampus (Buzsaki, 2015; Buzsaki et al., 1983). Thus, by using the aforementioned approach we were able to rapidly switch between network states. During absence of light hippocampal slices generated spontaneous SPW-R oscillations. Upon light presentation in the described pattern, gamma oscillations were observed. We were

## 4.2 Differential Modulation of Hippocampal Network Oscillations by Oxytocin *in vitro*

able to investigate the activity-dependent transition between different hippocampal oscillatory states in more detail in (Geschwill et al., 2018).

Likewise to the prior pharmacological gamma oscillations, optogenetically evoked gamma oscillations were insensitive to the presence of TGOT (100 nM) (figure 4.15 D,  $n = 14$ ). Data is presented as mean  $\pm$  SEM. Quantifications revealed that gamma peak power ( $0.84 \pm 0.25$  a.u. [baseline] vs.  $0.73 \pm 0.16$  a.u. [TGOT],  $P = 0.1269$ ), gamma frequency ( $47.7 \pm 1.6$  Hz [baseline] vs.  $45.1 \pm 2.8$  Hz [TGOT],  $P = 0.3303$ ) as well as gamma half width maximum ( $20.1 \pm 0.7$  Hz [baseline] vs.  $20.1 \pm 0.7$  Hz [TGOT],  $P = 0.9293$ ) were not modulated by TGOT (figure 4.15 D).

All in all, we were able to present evidence that the activation of ORs modulates hippocampal network oscillations selectively. While SPW-R characteristics were largely diminished, different gamma oscillation models were independent of oxytocin modulations. With respect to the association of SPW-R oscillations with memory consolidation and gamma oscillations with memory formation, oxytocin potentially rather influences the first process.

## Contributions to the Study of The Impact of Oxytocin on Hippocampal Network Oscillations

Data shown in section 4.2 was collected in joint efforts of Pia Maier and Martin E. Kaiser. Pia Maier and Martin E. Kaiser contributed equally, consequently the study resulted in a shared first authorship publication (Maier et al., 2016). Data analysis and figure design were performed by Pia Maier, Martin Both and Martin E. Kaiser. Contributions to the illumination setup are stated in section 3.5.1.

## 4.3 Amyloid Precursor Protein Protected Neuronal Networks against Hypoxia *in vitro*

Neural oscillations are diminished by oxygen-lacking conditions (Hefter et al., 2016), potentially influencing associated memory processes. Thus, neurons potentially provide an arsenal of neuroprotective mechanisms, which contribute to a fast recovery after functional diminution due to neurotoxic events. Previous studies suggest a potentially neuroprotective role of endogenous APP and / or APPs $\alpha$  (see section 1.4.2). Here, we thus aimed to investigate the mechanism through which APP fragments function.

### 4.3.1 Block of L-type Calcium Channels Alleviated Posthypoxic Deficits in APP<sup>-/-</sup> Mice

Hypoxia disrupts neuronal membrane potential and firing properties (Hefter et al., 2016). Oxygen deprivation is accompanied by an intracellular calcium concentration increase (Lobner and Lipton, 1993). L-type voltage gated calcium channels (LTCCs) and NMDA receptors are a major source of neuronal calcium influx. Antagonizing them reduces the damaging impact of hypoxic conditions (Zhang et al., 2002). Since APP is associated with both LTCCs (Yang et al., 2009) and NMDA receptors (Cousins et al., 2009), we repeated such blockage experiments with electrophysiological and calcium imaging techniques in hippocampal mouse brain slices. To carve out the potentially neuroprotective role of APP and / or APPs $\alpha$  during hypoxia, we conducted the experiments on wild-type (WT), APP<sup>-/-</sup>, and APPs $\alpha$ -KI mice.

Field potential and intracellular recordings from hippocampal CA1, applied and analyzed by Dimitri Hefter (Hefter et al., 2016), revealed that hypoxia impaired excitability in APP<sup>-/-</sup> but not in WT hippocampal brain slices.



### 4.3 Amyloid Precursor Protein Protected Neuronal Networks against Hypoxia *in vitro*

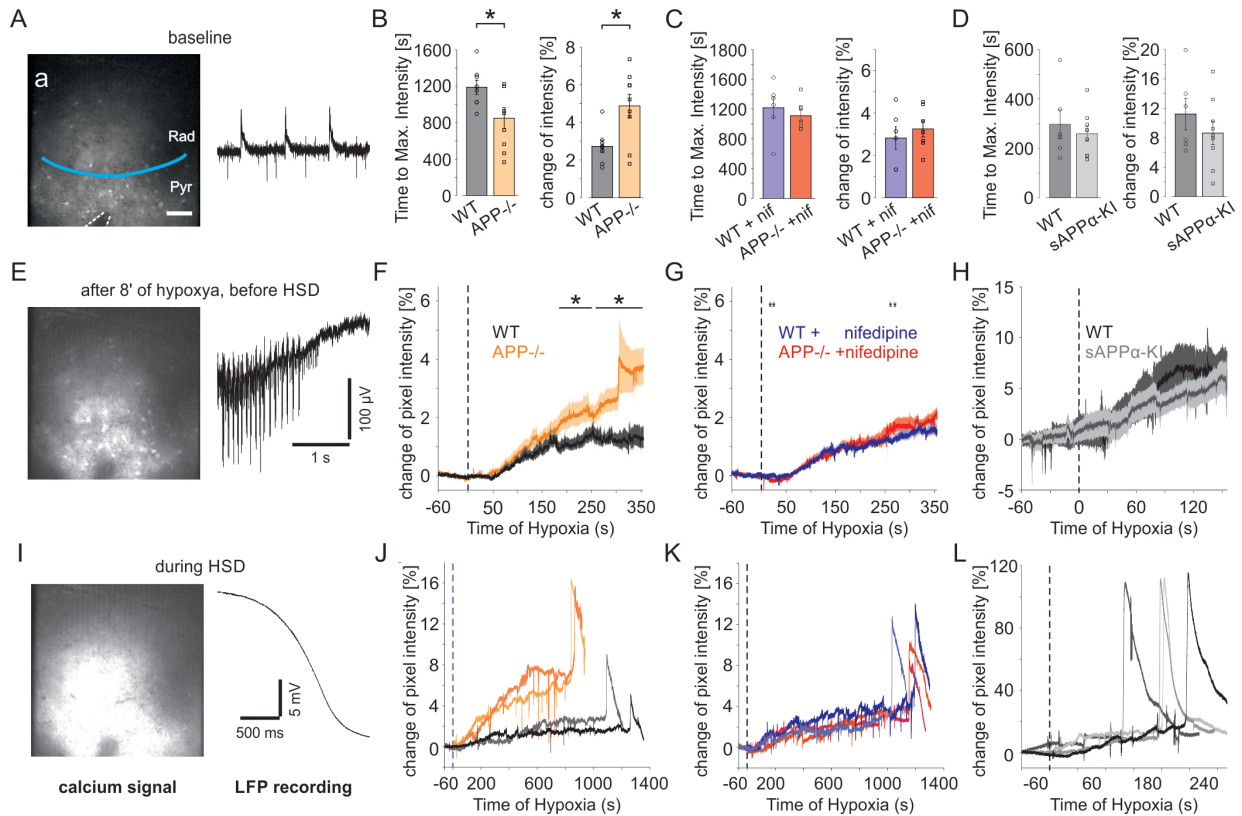


**Figure 4.16: Increased calcium influx through LTCC reduced latency to hypoxia-induced spreading depression in  $APP^{-/-}$  hippocampal brain slices.**

(A, E, and I) Representative examples of calcium imaging (left) in CA1 and the corresponding LFP recordings (right). During standard oxygen condition (A; see section 3.3.1), at the plateau-like phase before the spreading depression (E) and during hypoxia-induced spreading depression (I) calcium levels differed. Abbreviations: Rad - stratum radiatum. Pyr - stratum pyramidale. (A) Blue line illustrates the approximate border between Rad and Pyr in CA1. Dashed line indicates the position of the recording pipette. White bar represents 50  $\mu\text{m}$ , for A, E and I. (B–D) **Quantification of maximal calcium influx showed significant differences between genotypes.** Latency to the peak of fluorescence intensity (left) and increase of fluorescence intensity at the plateau before spreading depression (right) in untreated WT and  $APP^{-/-}$  slices (B;  $n = 7/9$  slices from 4/5 mice, respectively), in nifedipine-treated WT and  $APP^{-/-}$  (C; 6/7 slices from 2/3 mice, respectively), and in untreated WT and  $APP_{s\alpha}\text{-KI}$  slices (D; 6/9 slices from 2/3 mice, respectively). (F)–(H) and (J)–(L) **Calcium levels increased during hypoxia.** Hypoxia-induced mean increase of pixel intensity in (F) untreated, (G) nifedipine-treated WT and  $APP^{-/-}$  and (H) untreated WT and  $APP_{s\alpha}\text{-KI}$  slices. Dashed lines indicate the start of hypoxia. Fluorescence intensity increase shown with each two representative (J) untreated, (K) nifedipine-treated, (K) WT and  $APP^{-/-}$  and (L) untreated WT and  $APP_{s\alpha}\text{-KI}$  slices during hypoxia. \* $P < 0.05$ . Adapted from Hefter et al. (2016).

Population spike generation, high-frequency firing of CA1 pyramidal cells as well as spon-

## 4 RESULTS

taneous SPW-R activity were impaired following five minutes of hypoxia. Furthermore, these experiments alluded that blockage of LTCCs was crucial to mitigate neuronal damage after hypoxia. Application of the LTCC antagonist nifedipine (10  $\mu\text{M}$ ) indeed diminished observed differences between WT and  $\text{APP}^{-/-}$  tissues. The NMDA receptor antagonist D-APV (60  $\mu\text{M}$ ) had no effect on  $\text{APP}^{-/-}$  hippocampal tissue (Hefter et al., 2016). The obtained electrophysiological evidence pointed towards a substantial role of calcium influx through LTCCs regarding the increased susceptibility of APP-deficient mice to hypoxia. However, evidence showing the calcium dynamics during hypoxia, with and without blocking LTCCs, was needed.

Hence, in this work, we performed calcium imaging experiments in conjunction with standard field potential recordings in hippocampal area CA1. We compared the calcium dynamics in CA1 of WT,  $\text{APP}^{-/-}$ , and  $\text{APP}_{\alpha}\text{-KI}$  hippocampal networks before and during hypoxia (figure 4.16). Briefly, cells were bulk-loaded with OGB-1 by lowering an OGB-1 filled glass electrode into the slice prior to imaging (section 3.5.3). Gentle pressure application caused a slow OGB-1 injection into the CA1 region. After incubation we were able to record fluorescent pixel intensity variations from an area of about  $500 \times 500 \mu\text{m}$  (figure 4.16 A, E, I). Due to the calcium-binding characteristics of OGB-1, a change in fluorescent intensity correlated with a change in intracellular calcium concentrations. The following imaging data was analyzed as described in section 3.5.3. First, we obtained 5 min baseline activity of field potential fluctuations and corresponding calcium dynamics, while supplying the tissue with a gas mixture of 95 %  $\text{O}_2$  and 5 %  $\text{CO}_2$ . Afterwards, we switched to hypoxic gas supply conditions (95 %  $\text{N}_2$  and 5 %  $\text{CO}_2$ ). During the time course of hypoxia fluorescent intensity increased continuously (figure 4.16 E), typically reaching a plateau signal (figure 4.16 J-L). The amplitude of such a plateau intensity was increased in  $\text{APP}^{-/-}$  as compared to WT mice (figure 4.16 F). Hypoxia was maintained until so called hypoxia-induced spreading depressions occurred, which were observed as a rapid surge of fluorescent intensity, followed by a peak intensity (figure 4.16 I-L). Spreading depression constitute a prominent depolarization of neurons on the one hand and a dramatic

### 4.3 Amyloid Precursor Protein Protected Neuronal Networks against Hypoxia *in vitro*

distribution ion concentrations between the intra- and extracellular space on the other hand (Risher et al., 2010; Somjen, 2001). Peak intensities varied between cells, depending on the quality OGB-1 loading. Spreading depressions allowed us to image a maximum calcium influx into the cells. This peak pixel intensity signal was always higher than the prior plateau values, suggesting that they were indicating physiological values, which were not biased by technical calcium buffering limits of OGB-1. In the course of hypoxia the slices showed minor shrinking and expanding patterns, which changed the focused slice level and thereby also the recorded pixel intensities independent of cellular calcium influx. We corrected for these movements characteristics by adjusting the focus manually, depending on the magnitude of hypoxia-induced z-focus shifts. These shifts and the immediate focus corrections can be seen as downward spikes in the time course of pixel intensities (figure 4.16 J, K, L).

Strikingly, time to onset of spreading depressions was reduced in APP<sup>-/-</sup> mice ( $849.6 \pm 114.266$  s [WT] vs.  $1230.6 \pm 74.298$  s [APP<sup>-/-</sup>],  $P = 0.0385$ ; figure 4.16 B left), while the signal amplitude was increased ( $4.9 \pm 0.637$  % [WT] vs.  $2.69 \pm 0.36$  % [APP<sup>-/-</sup>],  $P = 0.0494$ ; figure 4.16 B right), as compared to WT mice ( $n = 7/9$  slices from 4/5 WT and APP<sup>-/-</sup> mice, respectively).

Application of nifedipine ( $10 \mu\text{M}$ ) abolished the observed differences between WT and APP<sup>-/-</sup> mice. Antagonizing LTCC receptors resulted in no difference in time to onset of spreading depressions ( $1111 \pm 75.007$  s [WT] vs.  $1216.9 \pm 143.086$  s [APP<sup>-/-</sup>],  $P = 0.5081$ ; figure 4.16 C left) as well as plateau intensity ( $3.24 \pm 0.347$  % [WT + nifedipine] vs.  $2.92 \pm 0.6143$  % [APP<sup>-/-</sup> + nifedipine],  $P = 0.8356$ ; figure 4.16 C right;  $n = 7/9$  slices from 4/5 WT and APP<sup>-/-</sup> mice, respectively). Also, the time course of fluorescent intensity changes were similar in both genotypes (figure 4.16 G, K). Next, we obtained further evidence for the key role of APP in the LTCC-mediated susceptibility to hypoxia. We compared calcium dynamics of WT and APP $\alpha$ -KI slices (figure 4.16 D, H and L). In line with the nifedipine experiments, slices from APP $\alpha$ -KI mice showed no difference in time to onset of spreading depressions ( $259.4411 \pm 29.9877$  s (WT) vs.  $277.0433 \pm 53.7153$  s (APP $\alpha$ -KI),  $P = 0.8639$ ; figure 4.16 D left), plateau intensity ( $8.2589 \pm 1.4963$  % [WT] vs.  $10.6201$

## 4 RESULTS

$\pm 1.7481$  % [APPs $\alpha$ -KI],  $P = 0.4559$ ; figure 4.16 D right) as well as the time course of fluorescent intensity changes (figure 4.16 H, L) as compared to WT tissue ( $n = 6/9$  slices from 2/3 WT and APPs $\alpha$ -KI mice, respectively). In accordance with field potential and single cell recordings presented in (Hefter et al., 2016), our calcium imaging data indicated disrupting consequences of a lack of APPs $\alpha$ .

All in all, we were able to confirm initial electrophysiological findings by Dimitri Hefter. We present supportive evidence that the calcium dynamics of APP<sup>-/-</sup> neural tissue showed a greater sensitivity towards hypoxia. This LTCC dependent effect could be rescued by either blocking these calcium channels or by APPs $\alpha$ , indicating that this APP fragment provides the basis for effective neuroprotection.

### **Contributions to the Study of the Neuroprotective Role of APP on Network Oscillations**

Data presented in section 4.3 contributed to the publication from Hefter et al. (2016). Dimitri Hefter set the foundations for the presented data, obtaining essential electrophysiological evidence. Calcium imaging and corresponding field potential recordings were performed by Martin E. Kaiser, as well as the respective analyses and figure design. For analysis custom-written Matlab scripts were used, created by Martin E. Kaiser.

## 5 Discussion

The hippocampus is vital for episodic and spatial memory (Squire et al., 2004). It is suggested that memory processes are enabled by groups of co-active cell forming neuronal ensembles (Hebb, 1949). While jointly performing neuronal computations these precisely spiking groups of neurons participate in network oscillations (Ylinen et al., 1995). In the local field potential, this coordinated activity can be observed as periodic potential changes (Buzsaki et al., 1983; Csicsvari et al., 2000; O'Keefe, 1976; O'Keefe and Recce, 1993), constituting behavioral correlates. Theta-nested gamma rhythms are present during active waking (Bragin et al., 1995; Vanderwolf, 1969) and rapid eye movement (REM) sleep (Jouvet, 1969). SPW-R oscillations are observed during immobility, consummatory behaviors and slow-wave sleep (Buzsaki et al., 1992, 1983). Networks oscillations are thought to synchronize neuronal activity and thereby to provide a temporal framework for the reliable formation neuronal ensembles (Buzsaki and Draguhn, 2004; Engel et al., 2001).

In this work we provide new insights in the formation, modulation and resistivity of neuronal ensemble activity during hippocampal network oscillations. We present evidence for a striking, so far unknown recruitment mechanism of single cells into defined ensembles. Further, our data showed selective modulatory effects of the endogenous hormone oxytocin on different network oscillations. Moreover, we illustrate a potential protection mechanisms of spontaneous rhythms in the hippocampus, working through L-type calcium channels.

## 5.1 Selective Recruitment of CA1 Pyramidal Cells into Hippocampal SPW-R-Ensembles Depended on Anatomical Features

In the first part of this work we unraveled a potential recruitment mechanism of single hippocampal pyramidal cells into neuronal ensembles (section 4.1). During hippocampal SPW-R oscillations the consecutive, temporally compressed reactivation of place cells supports spatial memory formation and consolidation (Buzsaki, 1986; Csicsvari and Dupret, 2014; Ego-Stengel and Wilson, 2010; Kali and Dayan, 2004). These cells exhibit experience-dependent reactivation during behavioral resting states (Pavrides and Winson, 1989; Wilson and McNaughton, 1994), resembling a selective activation of groups of cells that are geared to each other. *In vitro* and *in vivo* recordings provided evidence that inhibitory interneurons play a key role in the temporal organization of such ensembles (Csicsvari et al., 1999b). Therefore, excitatory pyramidal cells receive strong hyperpolarizing and shunting inhibition during SPW-Rs (Ellender et al., 2010; Gan et al., 2017; Klausberger et al., 2003).

Nevertheless, subgroups of pyramidal cells are somehow able to participate in SPW-R ensemble activity. *In vitro* these cells initiate somatic APs that exhibit an ectopic-like waveform, showing an abrupt rising, missing a slow subthreshold depolarization phase beforehand (Bahner et al., 2011). So far the recruitment mechanisms as well as the reason for their peculiar AP waveform are unknown.

### 5.1.1 Axon-Carrying Dendrite Cells Were Preferentially Recruited into SPW-R Oscillations

Within neuronal network oscillations, single neurons are activated, participating in ensemble activity. However, the mechanisms providing the basis for the observed selectivity of neuronal activity within hippocampal SPW-R oscillations are not fully understood.

### 5.1 Selective Recruitment of CA1 Pyramidal Cells into SPW-R-Ensembles *in vitro*

Why are some neurons activated while others, whether anatomically close or not, remain silent? In this regard, multiple potential recruitment mechanisms have been proposed. First, synaptic properties of a neuronal network promote differential excitation and inhibition of individual cells. Convergent and divergent synaptic wirings create structural frameworks for a specific flow of information (Kumar et al., 2010; Pernice et al., 2013; Song et al., 2005). Moreover, the strength of postsynaptic potentials differ depending on the respective synaptic efficacy (Lorente De N3, 1938; Sun et al., 2014). Both, synaptic connections as well as efficacy are influenced by activity-dependent plasticity, which can result in a modulation of neuronal ensemble formations (Bi and Poo, 1998; Garner et al., 2012; Lowel and Singer, 1992; Markram et al., 1997; Matsuzaki et al., 2004).

Taking a step further, evidence from *in silico* approaches suggests that nonlinear dendritic integration constitutes a potential mechanism for the activation of individual pyramidal cells into SPW-R ensembles (Memmesheimer, 2010). Voltage-gated sodium conductances in dendrites can trigger dendritic spikes that transverse to the soma and generate fast depolarizations with high temporal precision (Ariav et al., 2003; Gasparini and Magee, 2006; Gasparini et al., 2004). With respect to a group of excited neurons, supralinear dendritic interactions can mediate synchronization in network activity, diversifying the postsynaptic impact of synaptic potentials and thereby increasing the difference between participating and nonparticipating cells (Memmesheimer, 2010; Memmesheimer and Timme, 2012).

As a complementary possibility, Draguhn et al. (1998) and Schmitz et al. (2001) argue that the coupling of pyramidal cells via axonal gap junctions could result in the spiking of groups of neurons during SPW-R oscillations. Accordingly, ectopic-like, network-driven APs are generated by fast electronic coupling potentials, transmitting between axonal gap junctions that interconnect groups of pyramidal cells. Subsequent mathematical models predict that indeed this mechanism is able to generate spikes at high frequencies observed during ripples (Traub and Bibbig, 2000; Traub et al., 1994, 1999, 2012). Following their model, groups of pyramidal axons therefore generate APs at ripple frequency by utilizing conducting gap junction couplings. However, this view leaves the necessity of phasic inhi-

bition for ripple generation out of the picture. Consequently, the observed antidromic-like waveform of co-active cells during SPW-R oscillations might be complemented by other mechanisms.

Apart from that, it is hypothesized that the difference in AP firing behavior between participating and nonparticipating CA1 pyramidal cells results from distinct synaptic input strengths (Colgin, 2016). It is hypothesized that cells within a neuronal ensemble receive stronger excitatory inputs than cells outside such coordinated activity.

We followed up on this hypothesis and particularly took the work of Thome et al. (2014) into account. They recently discovered that the axons of about 50 % of CA1 pyramidal cells originate from a basal dendrite (AcD cells). The other half constitutes pyramidal cells of which the axons derive from the soma (nonAcD cells; Thome et al. 2014). In order to investigate whether the AcD as a privileged input channel impacts the recruitment of these cells into SPW-R ensembles, we performed field potential in conjunction with intracellular electrophysiological recordings from hippocampal brain slices. To our surprise, data presented in this work showed, that only AcD cells elicited SPW-R-entrained APs, while nonAcD cells were confined to spike outside of SPW-Rs. Furthermore, we showed that somatic excitatory as well as inhibitory conductance changes were similar in both pyramidal cell types. The amount of sharp wave- and ripple-evoked conductances as well as the amplitude, rate of rise, and decay kinetics of the overall conductances were not different between AcD and nonAcD cells. Our evidence thus contradicts the proposition from Colgin (2016). The observed differentiation in firing behavior cannot just be explained by different synaptic inputs alone.

Interestingly, peak excitatory and inhibitory conductances in awake mice were comparable to the respective values that we obtained (Gan et al., 2017). In our recordings, the average peak excitatory conductance was much lower than the peak inhibitory one. Also, the amplitude of SPW-R-entrained conductance changes were comparable between the *in vivo* and *in vitro* measurements. This comparison of the presented *in vitro* to already published *in vivo* data underlined the credibility of our approach.

So far, our evidence does not support the hypotheses from Schmitz et al. (2001) and



### 5.1 Selective Recruitment of CA1 Pyramidal Cells into SPW-R-Ensembles *in vitro*

Colgin (2016). Thus, we present the following alternative proposition about the involvement of single pyramidal cells in coherent neuronal activity.

#### 5.1.2 Cellular Anatomy and Incident Perisomatic Inhibition Shaped Defined CA1 Pyramidal Cell Recruitment into Ensemble Activity

In this work, we propose a recruitment mechanism of CA1 pyramidal cells into hippocampal SPW-R-ensemble activity that is based on an anatomical feature which allows excitation to bypass somatic inhibition-mediated shunting. We provided evidence that AcD cells were able to elicit APs because excitatory inputs to the respective axon-carrying dendrite remained efficient, while the ones to other dendrites were abolished by somatic shunting. Following this proposition, even similar excitatory as well as inhibitory inputs to individual AcD and nonAcD cells could result in selective spiking patterns. With respect to the intracellular flow of depolarization towards the AIS, excitatory inputs to the AcD would omit transversing through the soma and thereby directly depolarize the axonal region. In contrast, excitatory inputs to nonAcD cells would always be required to transverse the soma, in order to depolarize the AIS and thus be shunted during SPW-R oscillations. Hence, the here proposed recruitment mechanism is based on *in silico* evidence of Thome et al. (2014). They illustrate that in AcD cells, the axon and thus the AIS are shifted away from the perisomatic region, thus rendering the AP generation site to be less affected by perisomatic inhibition.

Our data strongly supports the here hypothesized AcD-based selection mechanism. We experimentally diminished SPW-R-entrained perisomatic inhibition of the targeted pyramidal cells. As a consequence and as predicted by the aforementioned hypothesis, we were able to demonstrate that upon this reduction, pyramidal cells participated in hippocampal ensemble activity, irrespective of their axon location. Strikingly, nonAcD cells elicited spontaneous APs within SPW-Rs. Moreover, the typical ectopic-like waveform of

participating APs changed to canonical waveforms. Consequently, the privilege of an AcD, regarding the efficacy of incident excitatory inputs in triggering APs, was abolished by the reduction of network-entrained perisomatic shunting.

To reduce SPW-R-driven perisomatic inhibition, we used two independent approaches, each only modulating the targeted pyramidal cell, while leaving the overall network activity unchanged. First, we utilized a pharmacological approach. While recording single pyramidal cells, we applied the GABA<sub>A</sub> receptor antagonist picrotoxin intracellularly, through the recording pipette (Goutman and Calvo, 2004; Inomata et al., 1988; Valero et al., 2017). As expected, the amount of inhibitory sharp wave- and ripple-entrained as well as the amplitude of the overall inhibitory conductances decreased. Thereby, prior silent pyramidal cells started to elicit APs during SPW-Rs. In detail, by using post-hoc anatomical analyses we confirmed that this approach resulted in the network-driven recruitment of nonAcD cells. However, due to possible drawbacks of this pharmacological approach, regarding drug application, controllability, and unknown unspecific binding effects, we utilized a second method of curtailing SPW-R-associated perisomatic inhibition. We implemented a dynamic clamp system that allowed us to precisely annihilate perisomatic inhibition depending on the membrane potential of the target cell. By applying dynamic clamp, we introduced an artificial conductance into a targeted cell that was tuned to the network-entrained inhibitory conductance input. Since synaptic input to individual pyramidal cells varies between cells and slice conditions, this approach enabled us to pursue a cell as well as network-state specific approach. The simulated artificial conductance diminished the impact of SPW-R-driven perisomatic inhibition effectively. In line with the aforementioned pharmacological approach, we thus obtained participating APs that resembled a canonical waveform, from a pyramidal cell that was likely to be regarded as a nonAcD cell. Nevertheless, our dynamic clamp approach still needs further characterization and adjustments to diminish inhibitory conductance changes to a greater extent. Data shown here was obtained from one cell only. However, we could still show that this approach worked as well as present evidence, supporting our working hypothesis.

At large, a decrease in shunting inhibition rendered an under baseline conditions im-

### 5.1 Selective Recruitment of CA1 Pyramidal Cells into SPW-R-Ensembles *in vitro*

peding anatomy, meaning the nonAcD less relevant for the network-driven selectivity of single pyramidal cells. In contrast, intact SPW-R-entrained perisomatic shunting prevented nonAcD cells from participating in hippocampal ensembles. Only AcD cells were able to circumvent this constricting network activity.

#### 5.1.3 Functional Consequences for the Information Processing in the Hippocampus

Recently, it was shown illustrated that in AcD cells the axon is preferentially located at basal dendrites (Thome et al., 2014). Moreover, in our somatic recordings we did not observe differences in network-entrained excitatory inputs between AcD and nonAcD cells. Distinct firing behaviors of the two cell groups relied on the location of excitatory inputs to respective basal dendrites. Thinking ahead, this points towards the possibility that excitatory inputs to apical dendrites might serve as a general excitation rather than being leveled cell specifically. The location of excitation to the basal dendrites, however, could be decisive for neuronal output generation. The AcD input route could be more effective and therefore AcD cells would be privileged as opposed to nonAcD cells, during SPW-R oscillations.

Furthermore, the here described functional separation of AcD and nonAcD cells might also resemble a recruitment mechanism of single cells into other network state-dependent neuronal ensembles. Interestingly, Epsztein et al. (2010) observed that in exploring rats, 7 out of 16 hippocampal CA1 pyramidal cells elicited APs, with exceedingly fast rising phases while the other 9 cells showed canonical APs only, *in vivo*. This number resembles the total proportion of hippocampal CA1 AcD cells (Thome et al., 2014), indicating a potential role of the here proposed AcD-based mechanism. Probable AcD cells fired ectopic-like APs at higher frequency inside than outside their respective place field. The observation of such a peculiar AP waveform during theta rhythms, in conjunction with the here shown data during SPW-R oscillations, indicates a broader importance of the proposed mechanism in

memory encoding in the hippocampus.

Intriguingly, other approaches did not lead to SPW-R-entrained ectopic-like APs in hippocampal CA1 pyramidal cell, *in vivo* (English et al., 2014). Moreover, *in vitro* the spiking behavior of pyramidal cells can be classified into two groups, either only firing canonical APs or eliciting ectopic-like as well as canonical APs, depending on the spatial position of the animals (Epsztein et al., 2010). We suggest that these findings underline the nonexclusive nature of the here presented anatomy-based integration mechanism. We propose that the here illustrated mechanism rather offers an additional recruitment option of principal cells into hippocampal ensemble activity. As described by Memmesheimer (2010), nonlinear dendritic integration constitutes a mechanism that theoretically leads to the recruitment of individual pyramidal cells into SPW-R ensembles. Supralinear dendritic integration can result from the activation of voltage-gated sodium (Ariav et al., 2003; Gasparini and Magee, 2006; Gasparini et al., 2004; Nevian et al., 2007), potassium channels (Johnston et al., 2000), as well as NMDA receptors (Grienberger et al., 2014; Schiller et al., 2000). In our recordings, we observed a time difference of peak SPW-R-evoked excitation between AcD and nonAcD cells, being about 6.625 ms later in the latter ones. This distinction can potentially be explained by differences in dendritic supralinear integration processes. In AcD cells these might mainly rely on sodium channels, which only allow a small time window of about 3 ms for nonlinear input integration (Magee and Cook, 2000; Memmesheimer, 2010). In nonAcD cells on the other hand, potassium channels could provide a larger time window of about 10 ms for dendritic coincidence detection of pre- and postsynaptic activity (Johnston et al., 2000; London and Hausser, 2005). Indeed, an enhanced supralinear integration in axon-carrying versus non-axon-carrying dendrites was shown (Thome et al., 2014). Hence, differences in nonlinear dendritic processes are observed, indicating a distinct ionic prevalence and distribution of respective ion conductances in between AcD and nonAcD cells. Further, the here proposed selectivity mechanism of single hippocampal pyramidal cells during network oscillations is unlikely to work digitally, meaning. First, AcD cells constitute 50 % of CA1 pyramidal cells (Thome et al., 2014). It is thus unlikely that the proposed mechanism works in a nonexclusive all or nothing

### 5.1 Selective Recruitment of CA1 Pyramidal Cells into SPW-R-Ensembles *in vitro*

pattern. As shown by computational modeling, the shunting impact of perisomatic inhibition depends on the distance of the axon, branching from a dendrite, to the soma (Thome et al., 2014). Consequently, plasticity mechanisms can influence the impact of perisomatic inhibition on the output, by modulating the positioning of the axon, relative to the soma. It has already been shown that the AIS positioning and length can be modulated in an activity-dependent manner (Grubb and Burrone, 2010; Kuba et al., 2010, 2015), indicating that so far unknown plasticity mechanisms potentially regulate the AcD anatomy.

#### 5.1.4 Potential Impact of the *in vitro* Condition on Observed Spiking Pyramidal Cells Behaviors

Data presented in this work was obtained from *in vitro* experiments, recording intra- and extracellular voltage fluctuations in 400  $\mu\text{m}$  thick hippocampal brain slices. Due to the slicing process, dendritic as well as axonic branches were pruned away, which is likely to have resulted in diminished cellular inputs to the targeted CA1 pyramidal cells. The resulting lack of network connections can potentially explain the observed discrepancy between participating and nonparticipating AcD cells. However, although only half of AcD cells elicited SPW-R-entrained APs, all identified nonAcD pyramidal cells remained silent during SPW-Rs.

Furthermore, a comparison of the peak inhibition to excitatory conductances *in vitro* to *in vivo* indicated an increase in the latter condition. This could provide an explanation of the observed ectopic-like waveform of all pyramidal APs that were elicited within SPW-Rs, while English et al. (2014) only reported canonical APs. Stronger perisomatic inhibition can result in an increased SPW-R-driven hyperpolarization of somatic membrane potentials. Back-propagating APs are therefore more likely to be recorded as ectopic.

## 5.2 Selective Neuromodulatory Effects of Oxytocin on Hippocampal Network Oscillations *in vitro*

After investigating the newly proposed mechanism of spontaneous ensemble formation, we took our investigation of neuronal ensemble activity during network oscillations a step further. We aimed for a more detailed understanding of the impact of the neuromodulator oxytocin on hippocampal network states (section 4.2). We investigated the effect and specificity of an oxytocin receptor activation on spontaneous SPW-Rs and multiple gamma oscillation models.

It appears interesting that oxytocin caused a profound suppression of SPW-Rs, while leaving gamma oscillations mostly unchanged. Both hippocampal network states are mutually exclusive, hinting a specific neuromodulatory role of oxytocin.

### 5.2.1 Oxytocin Receptor Activation Affected Spontaneous SPW-Rs

*In vitro*, SPW-Rs consist of a positive field potential deflection with superimposed fast ripple oscillations, when recorded in stratum pyramidale of the CA region. Interestingly, we found that the oxytocin receptor agonist TGOT modulates the aforementioned SPW-R characteristics.

TGOT decreased SPW-R amplitudes, which can potentially be explained by two mechanisms. On the one hand, blocking GABA<sub>A</sub> receptors diminishes positive SPW-Rs components in stratum pyramidale (Schonberger et al., 2014). In accordance with that TGOT increases the firing of inhibitory interneurons in the hippocampus (Owen et al., 2013). Tonic inhibition is elevated while phasic inhibition decreases due to use-dependent depression of interneuron-pyramidal cell synapses (Owen et al., 2013). This indicates that TGOT reduced phasic inhibitory synaptic transmission, which led to smaller SPW-R am-

## 5.2 Selective Neuromodulatory Effects of Oxytocin on Hippocampal Network Oscillations *in vitro*

plitudes. On the other hand, it is suggested that CA3 pyramidal cells provide bursts of excitatory inputs to the CA1 area, generating positive SPW-R deflection in stratum pyramidale (Buzsaki, 1986, 2015; Sullivan et al., 2011). In this context, TGOT might hinder the excitation from emanating through the CA areas.

In addition to SPW-R amplitudes, TGOT also reduced the incidence of SPW-Rs. As stated above phasic and tonic inhibition appear to modulate SPW-R amplitudes. Moreover, the two components of inhibition define a time window for SPW-R generation (Bahner et al., 2011; Ellender et al., 2010; Viereckel et al., 2013). SPW-R incidence can be modulated by the GABA receptor subtypes A and B (Hollnagel et al., 2014; Nimmrich et al., 2005). Prolongation of the GABA<sub>A</sub> decay time constant suppresses the frequency of SPW-R occurrence (Viereckel et al., 2013). Interestingly, tonic inhibition appears to be required for SPW-R activity. Low concentrations of GABA<sub>A</sub> receptor blockers fully abolish SPW-R occurrence (Ellender et al., 2010). Agonizing GABA<sub>B</sub> receptors suppresses SPW-R incidence as well (Hollnagel et al., 2014). In line with Viereckel et al. (2013) and Owen et al. (2013), SPW-R reduction by TGOT might also occur due to inhibition of pyramidal cell targeting inhibitory interneurons (Muhlethaler et al., 1984).

Further, we found that TGOT reduced ripple energy as well as the number of ripple cycles of SPW-Rs. Again the modulation of fast-spiking interneurons by oxytocin can present a potential mechanistic explanation for the this finding (Owen et al., 2013). Through inhibitory interneuron firing, oxytocin sharpens excitation-spike coupling while suppressing background pyramidal cell activity (Owen et al., 2013). In the field less pyramidal cell firing can potentially be observed as diminished negative deflections. Alteration of synaptic transmission bears the potential to modulate spiking precision. However, the underlying mechanism of interneuron-pyramidal cell phase-coupling remains to be explained (Csicsvari et al., 1999b; Memmesheimer, 2010; Schmitz et al., 2001).

Strikingly, TGOT application reduced all SPW-R characteristics except for the ripple frequency. This observation contradicts the presumed role of GABAergic inhibition in ripple generation, supporting other possible mechanisms (Memmesheimer, 2010; Schmitz et al., 2001). Similarly, other approaches also report that a change of synaptic transmis-

sion leaves the ripple frequency unchanged (Bahner et al., 2011; Schonberger et al., 2014; Viereckel et al., 2013).

### 5.2.2 Oxytocin Receptor Activation Spared Induced Gamma Oscillations

In contrast to the effect on SPW-Rs, TGOT failed to modulate most features of the applied gamma rhythms. Gamma power and frequency of all pharmacologically and optogenetically induced gamma oscillations did not change upon TGOT application. However, Owen et al. (2013) shows evidence that the kainate-induced gamma oscillation is sensitive to oxytocin receptor activation due to an increased amplitude of the evoked population spike. In line with this, we observed that TGOT enhanced gamma amplitude and reduced half width maximum during kainate-induced gamma. We further employed an interneuron gamma model during which ionotropic glutamate receptors were blocked. Similar to the carbachol gamma model, the interneuron gamma model was insensitive to TGOT. Taking a step further and eliminating neuromodulatory interferences, we next applied an optogenetical gamma model. Due to ChR2 expression the presentation of ramp-like light patterns stimulated pyramidal cells in a theta rhythm. The resulting gamma oscillation was not affected by TGOT.

The presented evidence points towards the conclusion that hippocampal gamma oscillations are largely insensitive to oxytocin receptor activation. This profound discrepancy in oxytocin receptor sensitivity between spontaneous SPW-Rs and induced gamma oscillations appears crucial. It might reflect functional differences between the two network rhythms and could thus be explained by these.

The first possible reason for the observed differences might lie in the differing role of tonic and phasic inhibition during SPW-Rs and gamma oscillations. A modulation of inhibition could therefore result in distinct impacts, being less effective during gamma gamma oscillations. Oxytocin increases the firing frequency of fast-spiking interneurons (FSI) and



## 5.2 Selective Neuromodulatory Effects of Oxytocin on Hippocampal Network Oscillations *in vitro*

thereby modulates phasic and tonic inhibition (Owen et al., 2013).

*In vitro*, during SPW-R oscillation FSI fire at around 6 Hz (Bahner et al., 2011) while being active with 30-45 Hz during gamma oscillations (Bartos et al., 2007; Butler et al., 2016). Hence, the rhythm related differences in the responsiveness to oxytocin that we observed, might reflect distinct oxytocin induced firing frequency modulations of FSI. At baseline conditions FSI fire at a lower frequency during SPW-R than during gamma oscillations (Bahner et al., 2011; Bartos et al., 2007; Butler et al., 2016). Oxytocin could thus have a stronger relative impact in enhancing FSI activity during SPW-Rs, resulting in a higher increase in discharges. During gamma oscillations FSI firing frequency has reached a relatively high level already at baseline conditions. Oxytocin might not be potent enough to increase it further. There is a correlation between FSI discharges and the states of phasic as well as tonic inhibition (Owen et al., 2013). Differently affected FSI action potential activity during both types of network rhythms might therefore also result in diverging modulations of phasic and tonic inhibition. If oxytocin modulates the balance of both inhibitory components less during gamma oscillations, distinct oscillation related inhibition can be an explanation for our observation that oxytocin modulated SPW-R but not gamma oscillations.

A second explanation for the observed differences in the sensitivity of SPW-Rs versus gamma rhythms might lie in the distinct local networks that are formed by hippocampal inhibitory interneurons, amongst each other and together with pyramidal cells (Csicsvari et al., 1999b; Klausberger and Somogyi, 2008). Oxytocin could have selective effects on such local connections, depending on the types of interneurons involved and the nature of the occurring network oscillation (Memmesheimer, 2010; Whittington et al., 2011). During a SPW-R, evidence suggests that perisomatic PV<sup>+</sup> basket and bistratified cells increased their firing frequency (Buhl et al., 1994; Klausberger et al., 2003; Varga et al., 2014; Ylinen et al., 1995), while axo-axonic, cholecystokinin expressing and oriens-lacunosum moleculare GABAergic cells are silenced (Klausberger et al., 2003, 2005). However, such a digital on/off feature of certain interneuron types is not observed during gamma oscillations. Evidence suggested that all identified inhibitory interneurons are activated during theta-nested

gamma oscillation (Klausberger and Somogyi, 2008). Interestingly, in CA3 a similar situation can also be observed during SPW-Rs (Hajos et al., 2013). Consequently, if distinct interneuron types participate during the two network oscillations, it is possible that oxytocin modulates these differently and thus changes network rhythms depending on their frequency.

In this work, we provide striking evidence that oxytocin affects different network oscillations distinctly. Projecting these results to the behavioral level oxytocin might also play a profound role in social cognition, cognitive performance as well as psychiatric diseases (Feifel et al., 2012, 2010; Guastella et al., 2010; Pedersen et al., 2011). Further studies have thus to be conducted to understand the network effects of oxytocin on behavioral states fully.

### **5.3 Neuroprotection by Amyloid Precursor Protein during Hypoxic Stress**

The preservation of a precisely neuronal ensemble activity is vital for reliable memory processes. Sudden incidences like brain ischemia can impact crucial network oscillations negatively. Thus, under normal conditions reliable mechanism can suddenly be malfunctioning. However, neuronal networks provide protection mechanisms, that support fast recovery from disturbing incidences.

#### **5.3.1 Soluble Amyloid Precursor Protein Alpha Exerted a Neuroprotective Role through L-Type Calcium Channels**

In this work, we present evidence that APP has a neuroprotective effect, underlining previously published *in vitro* (Kogel et al., 2012) and *in vivo* (Clarke et al., 2007; Koike et al., 2012) studies (section 4.3). APP and its cleavage products are strongly involved in

### 5.3 Neuroprotection by Amyloid Precursor Protein during Hypoxic Stress

Alzheimer's disease (O'Brien and Wong, 2011). However, the exact role in neurons' viability is still unknown. Our calcium imaging approach demonstrated that during hypoxia hippocampal brain slices from APP<sup>-/-</sup> mice showed an increased calcium influx as compared to WT animals. This difference between APP<sup>-/-</sup> and WT mice could be abolished by antagonizing L-type calcium channels with nifedipine. Importantly, tissue of both genotypes was treated with nifedipine. Unspecific hypoxic effects were therefore not responsible for the observed deficits of APP<sup>-/-</sup> neuronal tissue. We argue that the lack of APP in APP<sup>-/-</sup> mice enhanced the LTCC-dependent rise of intracellular calcium levels during hypoxia. In accordance with our argumentation, Yang et al. (2009) demonstrated that APP interacts with Ca<sub>v</sub>1.2 LTCCs, which as a result suppresses neuronal voltage-dependent calcium influx. Taking a step further, Anekonda et al. (2011) as well as Anekonda and Quinn (2011) suggested the blockage of calcium channels as a prospective neuroprotective treatment of Alzheimer's disease. Generally, increased intracellular calcium have been shown to cause dysfunctional and damaging effects (Thibault et al., 2007; Zhang et al., 2002).

Strikingly, in our experiments APPs $\alpha$ -KI and WT mice showed no difference in calcium influx through LTCCs during hypoxia. In line with previous studies (Smith-Swintosky et al., 1994; Thornton et al., 2006), we thus suggest that the observed hypoxia-dependent neurodamaging effects appeared to be mostly mediated by a lack of the soluble extracellular domain APPs $\alpha$ . APPs $\alpha$  has been shown to abolish amyloid- $\beta$ -dependent toxic effects (Fol et al., 2016; Obregon et al., 2012) and to rescue APP-induced deficits (Hick et al., 2015; Ring et al., 2007). Our evidence strongly suggests that APPs $\alpha$  diminished calcium influx through LTCCs. Whereas amyloid peptides the expression (Webster et al., 2006) and consequently the potential calcium influx increases. APPs $\alpha$  potentially affects LTCCs extracellularly, while APP could interact with LTCCs intracellularly (Yang et al., 2009).

Our evidence suggests a neuroprotective role of APP and APPs $\alpha$  against damaging impacts of hypoxia. For future clinical approaches against Alzheimer's disease or vascular diseases, reconstituting neuronal calcium homeostasis diminishing damaging rise of intracellular calcium levels might be promising therapeutic therapies.

## 6 Outlook

In this work, we answered prominent questions about the following three major issues. We showed a recruitment mechanism of single pyramidal cells into neuronal ensembles, presented the extend of an oxytocin-based modulation of oscillatory ensemble activity as well as described the neuroprotective impact of the amyloid precursor protein on calcium dynamics during SPW-R oscillations. Nevertheless, there are still open questions regarding the detailed mechanisms behind the observed findings. This section will provide insights into possible experiments and ideas, targeting some of these issues.

### **Privileged Recruitment of AcD Cells into SPW-R Oscillations - Next Step: Studying the Functional Role**

We present evidence that AcD pyramidal cells were preferentially recruited during SPW-R oscillations in hippocampal CA1 *in vitro*, whereas nonAcD pyramidal cells generally remained silent. Our data suggests that this exclusive SPW-R-entrained spiking behavior of AcD cells represents a possible, so far unknown mechanism to include individual cells into functional ensembles. In this way, AcD cells were potentially activated during SPW-Rs because their axons were decoupled from the soma, allowing specific excitatory dendritic input to circumvent SPW-R-entrained perisomatic inhibition *in vitro*. However, as prominent as the AcD-based selection mechanism was observed to be, future experiments will have to show the relevance of an AcD-based recruitment mechanism *in vivo*. One could

repeat the here presented recordings from single pyramidal cells in conjunction with field potential measurements in freely moving rodents and obtain the anatomy of recorded cells afterwards. This approach could confirm the importance of the AcD anatomy of pyramidal cells that participate in SPW-Rs.

In the hippocampus, about 50 % of CA1 pyramidal cells are described to be AcD cells (Thome et al., 2014). Therefore, during SPW-R oscillations the AcD-based recruitment mechanism reduced the cell population pool that is able to be recruited to only 50 % of all CA1 pyramidal cells. However, this pool of cells is unlikely to be the same for all network oscillations. Therefore, future studies will have to provide insights into recruitment mechanisms and the regarding cell pool during other oscillation types. Additionally, while we observed a distinct network-entrained firing behavior in AcD versus nonAcD cells, both groups received similar synaptic inputs during SPW-R oscillations. Future approaches will also have to describe if this holds true for other network oscillations. *In vitro*, these two issues, the digital AcD versus nonAcD spiking as well as the estimation of synaptic inputs, could be investigated during gamma oscillations by either inducing gamma rhythms pharmacologically or optogenetically, as presented in this work.

Moreover, the axon to soma distance might modulate the AcD-based recruitment mechanism during SPW-R oscillations (Thome et al., 2014), since synaptic potentials are shown to decrease with distance intracellularly (Magee, 2000). Therefore, future studies might be able to decipher potential correlation between the axonal distance to the soma and functional consequences.

Furthermore, if the AcD-based recruitment mechanism is as vital as we observed it to be during hippocampal network oscillations, the AcD anatomy could be modulated at a certain developmental stage or even continuously throughout life. Further studies could investigate an AcD plasticity during *in vivo* behavioral tasks. Live imaging of the AIS could be conducted via genetically-encoded fusion of a fluorescent protein to AIS-specific voltage-gated sodium channels (Dumitrescu et al., 2016).

We confirmed that SPW-R-entrained APs depicted an ectopic-like waveform *in vitro*

(Bahner et al., 2011). In contrast, *in vivo* SPW-R-driven APs are described as orthodromic (English et al., 2014). A possible explanation for this lack of an ectopic-like waveform could be found in a lower inhibition to excitation ratio *in vivo*, which would result in a less hyperpolarized soma during SPW-R oscillations. Therefore, the relevance of the AcD-based recruitment mechanism could be underlined by paired recordings from the soma and the axon. These could show a larger delay in the AP generation between both compartments in AcD versus nonAcD cells.

### **Modulation of Hippocampal Oscillations by Oxytocin - Next Step: Going Beyond Mere Description**

We showed the selective modulation of hippocampal network oscillations by oxytocin *in vitro*. While oxytocin reduced spontaneous SPW-R oscillations, it did not alter gamma oscillations. In addition, future approaches could study this modulation *in vivo*, also targeting the question about its relevance for memory consolidation versus encoding.

The modulation selectivity of oxytocin was most likely observed due to a differing role of tonic and phasic inhibition during SPW-Rs and gamma oscillations. Single cell recordings from inhibitory interneurons could decipher the modulatory impact of oxytocin on tonic and phasic inhibition during both oscillation types. Moreover, inhibitory interneurons show distinctive spiking behaviors during SPW-R versus gamma oscillations. While perisomatic PV<sup>+</sup> basket and bistratified cells increase their spiking frequency during SPW-R oscillations, a broad activation in interneurons is observed during gamma oscillations (Buhl et al., 1994; Klausberger et al., 2003, 2005; Varga et al., 2014; Ylinen et al., 1995). Therefore, targeted intracellular recordings from different interneuron classes could provide insights into the differential modulation of them by oxytocin.

## **Modulation of Intracellular Calcium Dynamics by Amyloid Precursor Protein - Next Step: Studying the Effect on Memory**

In this work, we confirmed that a disrupted calcium homeostasis in APP<sup>-/-</sup> mice could be rescued by blocking L-type calcium channels. Moreover, the larger calcium influx in APP<sup>-/-</sup> as compared to APP<sup>sα</sup> mice could explain the protective role of the APP fragment APP<sup>sα</sup> during hypoxic conditions. We presented data that suggest the blockage of L-type calcium channels to be a promising neuroprotective treatment against ischemic brain injuries as well as Alzheimer's disease. However, future studies could evaluate the extent of neuroprotection of a selective antagonization of L-type calcium channels *in vivo*. Taking a step further, clinical studies could provide insights into the protective impact of memory during Alzheimer's disease.





# Bibliography

- Akam, T., Oren, I., Mantoan, L., Ferenczi, E., and Kullmann, D. M. (2012). Oscillatory dynamics in the hippocampus support dentate gyrus-ca3 coupling. *Nat Neurosci*, 15(5):763–8.
- Alle, H. and Geiger, J. R. (2006). Combined analog and action potential coding in hippocampal mossy fibers. *Science*, 311(5765):1290–3.
- Althammer, F. and Grinevich, V. (2017). Diversity of oxytocin neurons: beyond magno- and parvocellular cell types? *J Neuroendocrinol*.
- Amaral, D., Andersen, P., Bliss, T., Morris, R., and O’Keefe, J. (2007). *Historical perspective: proposed functions, biological characteristics, and neurobiological models of the hippocampus*, pages 9–36. Oxford University Press.
- Amaral, D. and Lavenex, P. (2007). *Hippocampal neuroanatomy*, page 37–114. Oxford University Press.
- Amaral, D. G. and Witter, M. P. (1989). The three-dimensional organization of the hippocampal formation: a review of anatomical data. *Neuroscience*, 31(3):571–91.
- Andersen, P., Bliss, T. V., and Skrede, K. K. (1971). Lamellar organization of hippocampal excitatory pathways. *Exp Brain Res*, 13(2):222–38.
- Anekonda, T. S. and Quinn, J. F. (2011). Calcium channel blocking as a therapeutic strategy for alzheimer’s disease: the case for isradipine. *Biochim Biophys Acta*, 1812(12):1584–90.

- Anekonda, T. S., Quinn, J. F., Harris, C., Frahler, K., Wadsworth, T. L., and Woltjer, R. L. (2011). L-type voltage-gated calcium channel blockade with isradipine as a therapeutic strategy for alzheimer's disease. *Neurobiol Dis*, 41(1):62–70.
- Ariav, G., Polsky, A., and Schiller, J. (2003). Submillisecond precision of the input-output transformation function mediated by fast sodium dendritic spikes in basal dendrites of ca1 pyramidal neurons. *J Neurosci*, 23(21):7750–8.
- Aschauer, D. F., Kreuz, S., and Rumpel, S. (2013). Analysis of transduction efficiency, tropism and axonal transport of aav serotypes 1, 2, 5, 6, 8 and 9 in the mouse brain. *PLoS One*, 8(9):e76310.
- Bahner, F., Weiss, E. K., Birke, G., Maier, N., Schmitz, D., Rudolph, U., Frotscher, M., Traub, R. D., Both, M., and Draguhn, A. (2011). Cellular correlate of assembly formation in oscillating hippocampal networks in vitro. *Proc Natl Acad Sci U S A*, 108(35):E607–16.
- Bartos, M., Vida, I., and Jonas, P. (2007). Synaptic mechanisms of synchronized gamma oscillations in inhibitory interneuron networks. *Nat Rev Neurosci*, 8(1):45–56.
- Belluscio, M. A., Mizuseki, K., Schmidt, R., Kempter, R., and Buzsaki, G. (2012). Cross-frequency phase-phase coupling between theta and gamma oscillations in the hippocampus. *J Neurosci*, 32(2):423–35.
- Benda, J., Gollisch, T., Machens, C. K., and Herz, A. V. (2007). From response to stimulus: adaptive sampling in sensory physiology. *Curr Opin Neurobiol*, 17(4):430–6.
- Berridge, M. J. (2010). Calcium hypothesis of alzheimer's disease. *Pflugers Arch*, 459(3):441–9.
- Bi, G. Q. and Poo, M. M. (1998). Synaptic modifications in cultured hippocampal neurons: dependence on spike timing, synaptic strength, and postsynaptic cell type. *J Neurosci*, 18(24):10464–72.
- Bieri, K. W., Bobbitt, K. N., and Colgin, L. L. (2014). Slow and fast gamma rhythms

- coordinate different spatial coding modes in hippocampal place cells. *Neuron*, 82(3):670–81.
- Blackstad, T. W., Brink, K., Hem, J., and Jeune, B. (1970). Distribution of hippocampal mossy fibers in the rat. an experimental study with silver impregnation methods. *J Comp Neurol*, 138(4):433–49.
- Blevins, J. E., Schwartz, M. W., and Baskin, D. G. (2004). Evidence that paraventricular nucleus oxytocin neurons link hypothalamic leptin action to caudal brain stem nuclei controlling meal size. *Am J Physiol Regul Integr Comp Physiol*, 287(1):R87–96.
- Borg-Graham, L. J., Monier, C., and Fregnac, Y. (1998). Visual input evokes transient and strong shunting inhibition in visual cortical neurons. *Nature*, 393(6683):369–73.
- Boyden, E. S., Zhang, F., Bamberg, E., Nagel, G., and Deisseroth, K. (2005). Millisecond-timescale, genetically targeted optical control of neural activity. *Nat Neurosci*, 8(9):1263–8.
- Bragin, A., Jando, G., Nadasdy, Z., Hetke, J., Wise, K., and Buzsaki, G. (1995). Gamma (40-100 hz) oscillation in the hippocampus of the behaving rat. *J Neurosci*, 15(1 Pt 1):47–60.
- Brunel, N. and Wang, X. J. (2003). What determines the frequency of fast network oscillations with irregular neural discharges? i. synaptic dynamics and excitation-inhibition balance. *J Neurophysiol*, 90(1):415–30.
- Buhl, E. H., Halasy, K., and Somogyi, P. (1994). Diverse sources of hippocampal unitary inhibitory postsynaptic potentials and the number of synaptic release sites. *Nature*, 368(6474):823–8.
- Burger, C., Gorbatyuk, O. S., Velardo, M. J., Peden, C. S., Williams, P., Zolotukhin, S., Reier, P. J., Mandel, R. J., and Muzyczka, N. (2004). Recombinant aav viral vectors pseudotyped with viral capsids from serotypes 1, 2, and 5 display differential efficiency

- and cell tropism after delivery to different regions of the central nervous system. *Mol Ther*, 10(2):302–17.
- Busnelli, M., Bulgheroni, E., Manning, M., Kleinau, G., and Chini, B. (2013). Selective and potent agonists and antagonists for investigating the role of mouse oxytocin receptors. *J Pharmacol Exp Ther*, 346(2):318–27.
- Butler, J. L., Mendonca, P. R., Robinson, H. P., and Paulsen, O. (2016). Intrinsic cornu ammonis area 1 theta-nested gamma oscillations induced by optogenetic theta frequency stimulation. *J Neurosci*, 36(15):4155–69.
- Buzsaki, G. (1986). Hippocampal sharp waves: their origin and significance. *Brain Res*, 398(2):242–52.
- Buzsaki, G. (1989). Two-stage model of memory trace formation: a role for "noisy" brain states. *Neuroscience*, 31(3):551–70.
- Buzsaki, G. (2015). Hippocampal sharp wave-ripple: A cognitive biomarker for episodic memory and planning. *Hippocampus*.
- Buzsaki, G. and Chrobak, J. J. (1995). Temporal structure in spatially organized neuronal ensembles: a role for interneuronal networks. *Curr Opin Neurobiol*, 5(4):504–10.
- Buzsaki, G. and Draguhn, A. (2004). Neuronal oscillations in cortical networks. *Science*, 304(5679):1926–9.
- Buzsaki, G., Horvath, Z., Urioste, R., Hetke, J., and Wise, K. (1992). High-frequency network oscillation in the hippocampus. *Science*, 256(5059):1025–7.
- Buzsaki, G., Leung, L. W., and Vanderwolf, C. H. (1983). Cellular bases of hippocampal eeg in the behaving rat. *Brain Res*, 287(2):139–71.
- Chini, B. and Manning, M. (2007). Agonist selectivity in the oxytocin/vasopressin receptor family: new insights and challenges. *Biochem Soc Trans*, 35(Pt 4):737–41.

- Clark, B. A., Monsivais, P., Branco, T., London, M., and Hausser, M. (2005). The site of action potential initiation in cerebellar purkinje neurons. *Nat Neurosci*, 8(2):137–9.
- Clarke, J., Thornell, A., Corbett, D., Soininen, H., Hiltunen, M., and Jolkkonen, J. (2007). Overexpression of app provides neuroprotection in the absence of functional benefit following middle cerebral artery occlusion in rats. *Eur J Neurosci*, 26(7):1845–52.
- Colgin, L. L. (2016). Rhythms of the hippocampal network. *Nat Rev Neurosci*, 17(4):239–49.
- Colgin, L. L., Denninger, T., Fyhn, M., Hafting, T., Bonnevie, T., Jensen, O., Moser, M. B., and Moser, E. I. (2009). Frequency of gamma oscillations routes flow of information in the hippocampus. *Nature*, 462(7271):353–7.
- Cousins, S. L., Hoey, S. E., Anne Stephenson, F., and Perkinson, M. S. (2009). Amyloid precursor protein 695 associates with assembled nr2a- and nr2b-containing nmda receptors to result in the enhancement of their cell surface delivery. *J Neurochem*, 111(6):1501–13.
- Csicsvari, J. and Dupret, D. (2014). Sharp wave/ripple network oscillations and learning-associated hippocampal maps. *Philos Trans R Soc Lond B Biol Sci*, 369(1635):20120528.
- Csicsvari, J., Hirase, H., Czurko, A., Mamiya, A., and Buzsaki, G. (1999a). Fast network oscillations in the hippocampal ca1 region of the behaving rat. *J Neurosci*, 19(16):RC20.
- Csicsvari, J., Hirase, H., Czurko, A., Mamiya, A., and Buzsaki, G. (1999b). Oscillatory coupling of hippocampal pyramidal cells and interneurons in the behaving rat. *J Neurosci*, 19(1):274–87.
- Csicsvari, J., Hirase, H., Mamiya, A., and Buzsaki, G. (2000). Ensemble patterns of hippocampal ca3-ca1 neurons during sharp wave-associated population events. *Neuron*, 28(2):585–94.
- Csicsvari, J., Jamieson, B., Wise, K. D., and Buzsaki, G. (2003). Mechanisms of gamma oscillations in the hippocampus of the behaving rat. *Neuron*, 37(2):311–22.

- Doller, H. J. and Weight, F. F. (1982). Perforant pathway activation of hippocampal ca1 stratum pyramidale neurons: electrophysiological evidence for a direct pathway. *Brain Res*, 237(1):1–13.
- Draguhn, A., Traub, R. D., Schmitz, D., and Jefferys, J. G. (1998). Electrical coupling underlies high-frequency oscillations in the hippocampus in vitro. *Nature*, 394(6689):189–92.
- Du Vigneaud, V., Ressler, C., and Trippett, S. (1953). The sequence of amino acids in oxytocin, with a proposal for the structure of oxytocin. *J Biol Chem*, 205(2):949–57.
- Dumitrescu, A. S., Evans, M. D., and Grubb, M. S. (2016). Evaluating tools for live imaging of structural plasticity at the axon initial segment. *Front Cell Neurosci*, 10:268.
- Ego-Stengel, V. and Wilson, M. A. (2010). Disruption of ripple-associated hippocampal activity during rest impairs spatial learning in the rat. *Hippocampus*, 20(1):1–10.
- Elezgarai, I., Diez, J., Puente, N., Azkue, J. J., Benitez, R., Bilbao, A., Knopfel, T., Donate-Oliver, F., and Grandes, P. (2003). Subcellular localization of the voltage-dependent potassium channel kv3.1b in postnatal and adult rat medial nucleus of the trapezoid body. *Neuroscience*, 118(4):889–98.
- Ellender, T. J., Nissen, W., Colgin, L. L., Mann, E. O., and Paulsen, O. (2010). Priming of hippocampal population bursts by individual perisomatic-targeting interneurons. *J Neurosci*, 30(17):5979–91.
- Engel, A. K., Fries, P., and Singer, W. (2001). Dynamic predictions: oscillations and synchrony in top-down processing. *Nat Rev Neurosci*, 2(10):704–16.
- English, D. F., Peyrache, A., Stark, E., Roux, L., Vallentin, D., Long, M. A., and Buzsaki, G. (2014). Excitation and inhibition compete to control spiking during hippocampal ripples: intracellular study in behaving mice. *J Neurosci*, 34(49):16509–17.
- Epsztein, J., Lee, A. K., Chorev, E., and Brecht, M. (2010). Impact of spikelets on hip-

- pocampal ca1 pyramidal cell activity during spatial exploration. *Science*, 327(5964):474–7.
- Feifel, D., Macdonald, K., Cobb, P., and Minassian, A. (2012). Adjunctive intranasal oxytocin improves verbal memory in people with schizophrenia. *Schizophr Res*, 139(1-3):207–10.
- Feifel, D., Macdonald, K., Nguyen, A., Cobb, P., Warlan, H., Galangue, B., Minassian, A., Becker, O., Cooper, J., Perry, W., Lefebvre, M., Gonzales, J., and Hadley, A. (2010). Adjunctive intranasal oxytocin reduces symptoms in schizophrenia patients. *Biol Psychiatry*, 68(7):678–80.
- Feldman, R., Gordon, I., Schneiderman, I., Weisman, O., and Zagoory-Sharon, O. (2010). Natural variations in maternal and paternal care are associated with systematic changes in oxytocin following parent-infant contact. *Psychoneuroendocrinology*, 35(8):1133–41.
- Feldman, R., Gordon, I., and Zagoory-Sharon, O. (2011). Maternal and paternal plasma, salivary, and urinary oxytocin and parent-infant synchrony: considering stress and affiliation components of human bonding. *Dev Sci*, 14(4):752–61.
- Feldman, R., Weller, A., Zagoory-Sharon, O., and Levine, A. (2007). Evidence for a neuroendocrinological foundation of human affiliation: plasma oxytocin levels across pregnancy and the postpartum period predict mother-infant bonding. *Psychol Sci*, 18(11):965–70.
- Fellous, J. M. and Sejnowski, T. J. (2000). Cholinergic induction of oscillations in the hippocampal slice in the slow (0.5-2 Hz), theta (5-12 Hz), and gamma (35-70 Hz) bands. *Hippocampus*, 10(2):187–97.
- Feng, T., Silva, D., and Foster, D. J. (2015). Dissociation between the experience-dependent development of hippocampal theta sequences and single-trial phase precession. *J Neurosci*, 35(12):4890–902.
- Fink, G., Robinson, I. C., and Tannahill, L. A. (1988). Effects of adrenalectomy and

- glucocorticoids on the peptides crf-41, avp and oxytocin in rat hypophysial portal blood. *J Physiol*, 401:329–45.
- Fisahn, A., Contractor, A., Traub, R. D., Buhl, E. H., Heinemann, S. F., and McBain, C. J. (2004). Distinct roles for the kainate receptor subunits *glur5* and *glur6* in kainate-induced hippocampal gamma oscillations. *J Neurosci*, 24(43):9658–68.
- Fisahn, A., Pike, F. G., Buhl, E. H., and Paulsen, O. (1998). Cholinergic induction of network oscillations at 40 hz in the hippocampus in vitro. *Nature*, 394(6689):186–9.
- Fleidervish, I. A., Lasser-Ross, N., Gutnick, M. J., and Ross, W. N. (2010). Na<sup>+</sup> imaging reveals little difference in action potential-evoked na<sup>+</sup> influx between axon and soma. *Nat Neurosci*, 13(7):852–60.
- Fol, R., Braudeau, J., Ludewig, S., Abel, T., Weyer, S. W., Roederer, J. P., Brod, F., Audrain, M., Bemelmans, A. P., Buchholz, C. J., Korte, M., Cartier, N., and Muller, U. C. (2016). Viral gene transfer of *apps*alpha rescues synaptic failure in an alzheimer’s disease mouse model. *Acta Neuropathol*, 131(2):247–266.
- Freund, T. F. and Antal, M. (1988). Gaba-containing neurons in the septum control inhibitory interneurons in the hippocampus. *Nature*, 336(6195):170–3.
- Fuchs, E. C., Zivkovic, A. R., Cunningham, M. O., Middleton, S., Lebeau, F. E., Bannerman, D. M., Rozov, A., Whittington, M. A., Traub, R. D., Rawlins, J. N., and Monyer, H. (2007). Recruitment of parvalbumin-positive interneurons determines hippocampal function and associated behavior. *Neuron*, 53(4):591–604.
- Fyhn, M., Molden, S., Hollup, S., Moser, M. B., and Moser, E. (2002). Hippocampal neurons responding to first-time dislocation of a target object. *Neuron*, 35(3):555–66.
- Gakhar-Koppole, N., Hundeshagen, P., Mandl, C., Weyer, S. W., Allinquant, B., Muller, U., and Ciccolini, F. (2008). Activity requires soluble amyloid precursor protein alpha to promote neurite outgrowth in neural stem cell-derived neurons via activation of the mapk pathway. *Eur J Neurosci*, 28(5):871–82.



- Gan, J., Weng, S. M., Pernia-Andrade, A. J., Csicsvari, J., and Jonas, P. (2017). Phase-locked inhibition, but not excitation, underlies hippocampal ripple oscillations in awake mice in vivo. *Neuron*, 93(2):308–314.
- Garaschuk, O., Milos, R. I., and Konnerth, A. (2006). Targeted bulk-loading of fluorescent indicators for two-photon brain imaging in vivo. *Nat Protoc*, 1(1):380–6.
- Garner, A. R., Rowland, D. C., Hwang, S. Y., Baumgaertel, K., Roth, B. L., Kentros, C., and Mayford, M. (2012). Generation of a synthetic memory trace. *Science*, 335(6075):1513–6.
- Gasparini, S. and Magee, J. C. (2006). State-dependent dendritic computation in hippocampal ca1 pyramidal neurons. *J Neurosci*, 26(7):2088–100.
- Gasparini, S., Migliore, M., and Magee, J. C. (2004). On the initiation and propagation of dendritic spikes in ca1 pyramidal neurons. *J Neurosci*, 24(49):11046–56.
- Geiger, J. R. and Jonas, P. (2000). Dynamic control of presynaptic ca(2+) inflow by fast-inactivating k(+) channels in hippocampal mossy fiber boutons. *Neuron*, 28(3):927–39.
- Geisler, C., Brunel, N., and Wang, X. J. (2005). Contributions of intrinsic membrane dynamics to fast network oscillations with irregular neuronal discharges. *J Neurophysiol*, 94(6):4344–61.
- Gerchberg, R. and Saxton, W. (1972). A practical algorithm for the determination of phase from image and diffraction plane pictures. *Optik*, 35(2):237–246.
- Geschwill, P., Kaiser, M. E., Draguhn, A., and Both, M. (2018). Activity-dependent switches between different oscillatory states of hippocampal networks. *In preparation*, Shared first authorship.
- Girardeau, G., Benchenane, K., Wiener, S. I., Buzsaki, G., and Zugaro, M. B. (2009). Selective suppression of hippocampal ripples impairs spatial memory. *Nat Neurosci*, 12(10):1222–3.

- Goutagny, R., Gu, N., Cavanagh, C., Jackson, J., Chabot, J. G., Quirion, R., Krantic, S., and Williams, S. (2013). Alterations in hippocampal network oscillations and theta-gamma coupling arise before abeta overproduction in a mouse model of alzheimer's disease. *Eur J Neurosci*, 37(12):1896–902.
- Goutagny, R., Jackson, J., and Williams, S. (2009). Self-generated theta oscillations in the hippocampus. *Nat Neurosci*, 12(12):1491–3.
- Goutman, J. D. and Calvo, D. J. (2004). Studies on the mechanisms of action of picrotoxin, quercetin and pregnanolone at the gaba rho 1 receptor. *Br J Pharmacol*, 141(4):717–27.
- Grienberger, C., Chen, X., and Konnerth, A. (2014). Nmda receptor-dependent multidendrite  $Ca^{2+}$  spikes required for hippocampal burst firing in vivo. *Neuron*, 81(6):1274–1281.
- Grubb, M. S. and Burrone, J. (2010). Activity-dependent relocation of the axon initial segment fine-tunes neuronal excitability. *Nature*, 465(7301):1070–4.
- Grubb, M. S., Shu, Y., Kuba, H., Rasband, M. N., Wimmer, V. C., and Bender, K. J. (2011). Short- and long-term plasticity at the axon initial segment. *J Neurosci*, 31(45):16049–55.
- Guastella, A. J., Einfeld, S. L., Gray, K. M., Rinehart, N. J., Tonge, B. J., Lambert, T. J., and Hickie, I. B. (2010). Intranasal oxytocin improves emotion recognition for youth with autism spectrum disorders. *Biol Psychiatry*, 67(7):692–4.
- Gulyas, A. I., Szabo, G. G., Ulbert, I., Holderith, N., Monyer, H., Erdelyi, F., Szabo, G., Freund, T. F., and Hajos, N. (2010). Parvalbumin-containing fast-spiking basket cells generate the field potential oscillations induced by cholinergic receptor activation in the hippocampus. *J Neurosci*, 30(45):15134–45.
- Haas, H. L., Schaerer, B., and Vosmansky, M. (1979). A simple perfusion chamber for the study of nervous tissue slices in vitro. *J Neurosci Methods*, 1(4):323–5.
- Hajos, N., Ellender, T. J., Zemankovics, R., Mann, E. O., Exley, R., Cragg, S. J., Freund,

- T. F., and Paulsen, O. (2009). Maintaining network activity in submerged hippocampal slices: importance of oxygen supply. *Eur J Neurosci*, 29(2):319–27.
- Hajos, N., Karlocai, M. R., Nemeth, B., Ulbert, I., Monyer, H., Szabo, G., Erdelyi, F., Freund, T. F., and Gulyas, A. I. (2013). Input-output features of anatomically identified ca3 neurons during hippocampal sharp wave/ripple oscillation in vitro. *J Neurosci*, 33(28):11677–91.
- Hammock, E. A. and Levitt, P. (2013). Oxytocin receptor ligand binding in embryonic tissue and postnatal brain development of the c57bl/6j mouse. *Front Behav Neurosci*, 7:195.
- Hasselmo, M. E., Bodelon, C., and Wyble, B. P. (2002). A proposed function for hippocampal theta rhythm: separate phases of encoding and retrieval enhance reversal of prior learning. *Neural Comput*, 14(4):793–817.
- Hasselmo, M. E. and Schnell, E. (1994). Laminar selectivity of the cholinergic suppression of synaptic transmission in rat hippocampal region ca1: computational modeling and brain slice physiology. *J Neurosci*, 14(6):3898–914.
- Hausser, M., Stuart, G., Racca, C., and Sakmann, B. (1995). Axonal initiation and active dendritic propagation of action potentials in substantia nigra neurons. *Neuron*, 15(3):637–47.
- Hebb, D. (1949). Organization of behavior. *Journal of Clinical Psychology*, 6(3):307–307.
- Hedstrom, K. L., Xu, X., Ogawa, Y., Frischknecht, R., Seidenbecher, C. I., Shrager, P., and Rasband, M. N. (2007). Neurofascin assembles a specialized extracellular matrix at the axon initial segment. *J Cell Biol*, 178(5):875–86.
- Hefter, D., Kaiser, M., Weyer, S. W., Papageorgiou, I. E., Both, M., Kann, O., Muller, U. C., and Draguhn, A. (2016). Amyloid precursor protein protects neuronal network function after hypoxia via control of voltage-gated calcium channels. *J Neurosci*, 36(32):8356–71.

- Heinrichs, M., Baumgartner, T., Kirschbaum, C., and Ehlert, U. (2003). Social support and oxytocin interact to suppress cortisol and subjective responses to psychosocial stress. *Biol Psychiatry*, 54(12):1389–98.
- Heinrichs, M., Meinlschmidt, G., Wippich, W., Ehlert, U., and Hellhammer, D. H. (2004). Selective amnesic effects of oxytocin on human memory. *Physiol Behav*, 83(1):31–8.
- Herde, M. K., Iremonger, K. J., Constantin, S., and Herbison, A. E. (2013). GnRH neurons elaborate a long-range projection with shared axonal and dendritic functions. *J Neurosci*, 33(31):12689–97.
- Hick, M., Herrmann, U., Weyer, S. W., Mallm, J. P., Tschape, J. A., Borgers, M., Mercken, M., Roth, F. C., Draguhn, A., Slomianka, L., Wolfer, D. P., Korte, M., and Müller, U. C. (2015). Acute function of secreted amyloid precursor protein fragment app $\alpha$  in synaptic plasticity. *Acta Neuropathol*, 129(1):21–37.
- Hodgkin, A. L. and Huxley, A. F. (1952). A quantitative description of membrane current and its application to conduction and excitation in nerve. *J Physiol*, 117(4):500–44.
- Hollnagel, J. O., Maslarova, A., Haq, R. U., and Heinemann, U. (2014). Gabab receptor dependent modulation of sharp wave-ripple complexes in the rat hippocampus in vitro. *Neurosci Lett*, 574:15–20.
- Hu, H., Vervaeke, K., and Storm, J. F. (2002). Two forms of electrical resonance at theta frequencies, generated by m-current, h-current and persistent  $Na^+$  current in rat hippocampal pyramidal cells. *J Physiol*, 545(Pt 3):783–805.
- Hu, W., Tian, C., Li, T., Yang, M., Hou, H., and Shu, Y. (2009). Distinct contributions of  $Na_v1.6$  and  $Na_v1.2$  in action potential initiation and backpropagation. *Nat Neurosci*, 12(8):996–1002.
- Huerta, P. T. and Lisman, J. E. (1995). Bidirectional synaptic plasticity induced by a single burst during cholinergic theta oscillation in CA1 in vitro. *Neuron*, 15(5):1053–63.

- Inomata, N., Tokutomi, N., Oyama, Y., and Akaike, N. (1988). Intracellular picrotoxin blocks pentobarbital-gated cl- conductance. *Neurosci Res*, 6(1):72–5.
- Ishizuka, N., Cowan, W. M., and Amaral, D. G. (1995). A quantitative analysis of the dendritic organization of pyramidal cells in the rat hippocampus. *J Comp Neurol*, 362(1):17–45.
- Jahnke, S., Timme, M., and Memmesheimer, R. M. (2015). A unified dynamic model for learning, replay, and sharp-wave/ripples. *J Neurosci*, 35(49):16236–58.
- Jensen, O. and Colgin, L. L. (2007). Cross-frequency coupling between neuronal oscillations. *Trends Cogn Sci*, 11(7):267–9.
- Ji, J. and Maren, S. (2008). Differential roles for hippocampal areas ca1 and ca3 in the contextual encoding and retrieval of extinguished fear. *Learn Mem*, 15(4):244–51.
- Johnston, D., Hoffman, D. A., Magee, J. C., Poolos, N. P., Watanabe, S., Colbert, C. M., and Migliore, M. (2000). Dendritic potassium channels in hippocampal pyramidal neurons. *J Physiol*, 525 Pt 1:75–81.
- Johnston, J., Forsythe, I. D., and Kopp-Scheinpflug, C. (2010). Going native: voltage-gated potassium channels controlling neuronal excitability. *J Physiol*, 588(Pt 17):3187–200.
- Jouvet, M. (1969). Biogenic amines and the states of sleep. *Science*, 163(3862):32–41.
- Jutras, M. J., Fries, P., and Buffalo, E. A. (2009). Gamma-band synchronization in the macaque hippocampus and memory formation. *J Neurosci*, 29(40):12521–31.
- Kali, S. and Dayan, P. (2004). Off-line replay maintains declarative memories in a model of hippocampal-neocortical interactions. *Nat Neurosci*, 7(3):286–94.
- Karlsson, M. P. and Frank, L. M. (2009). Awake replay of remote experiences in the hippocampus. *Nat Neurosci*, 12(7):913–8.
- Katsoyannis, P. G. and Du Vigneaud, V. (1958). Arginine-vasotocin, a synthetic analogue

- of the posterior pituitary hormones containing the ring of oxytocin and the side chain of vasopressin. *J Biol Chem*, 233(6):1352–4.
- Kirazov, L., Loffler, T., Schliebs, R., and Bigl, V. (1997). Glutamate-stimulated secretion of amyloid precursor protein from cortical rat brain slices. *Neurochem Int*, 30(6):557–63.
- Kirsch, P., Esslinger, C., Chen, Q., Mier, D., Lis, S., Siddhanti, S., Gruppe, H., Mattay, V. S., Gallhofer, B., and Meyer-Lindenberg, A. (2005). Oxytocin modulates neural circuitry for social cognition and fear in humans. *J Neurosci*, 25(49):11489–93.
- Klausberger, T., Magill, P. J., Marton, L. F., Roberts, J. D., Cobden, P. M., Buzsaki, G., and Somogyi, P. (2003). Brain-state- and cell-type-specific firing of hippocampal interneurons in vivo. *Nature*, 421(6925):844–8.
- Klausberger, T., Marton, L. F., O’Neill, J., Huck, J. H., Dalezios, Y., Fuentealba, P., Suen, W. Y., Papp, E., Kaneko, T., Watanabe, M., Csicsvari, J., and Somogyi, P. (2005). Complementary roles of cholecystinin- and parvalbumin-expressing gabaergic neurons in hippocampal network oscillations. *J Neurosci*, 25(42):9782–93.
- Klausberger, T. and Somogyi, P. (2008). Neuronal diversity and temporal dynamics: the unity of hippocampal circuit operations. *Science*, 321(5885):53–7.
- Knobloch, H. S., Charlet, A., Hoffmann, L. C., Eliava, M., Khrulev, S., Cetin, A. H., Osten, P., Schwarz, M. K., Seeburg, P. H., Stoop, R., and Grinevich, V. (2012). Evoked axonal oxytocin release in the central amygdala attenuates fear response. *Neuron*, 73(3):553–66.
- Knobloch, H. S. and Grinevich, V. (2014). Evolution of oxytocin pathways in the brain of vertebrates. *Front Behav Neurosci*, 8:31.
- Koch, C., Douglas, R., and Wehmeier, U. (1990). Visibility of synaptically induced conductance changes: theory and simulations of anatomically characterized cortical pyramidal cells. *J Neurosci*, 10(6):1728–44.
- Kogel, D., Deller, T., and Behl, C. (2012). Roles of amyloid precursor protein family members in neuroprotection, stress signaling and aging. *Exp Brain Res*, 217(3-4):471–9.

- Koike, M. A., Lin, A. J., Pham, J., Nguyen, E., Yeh, J. J., Rahimian, R., Tromberg, B. J., Choi, B., Green, K. N., and LaFerla, F. M. (2012). App knockout mice experience acute mortality as the result of ischemia. *PLoS One*, 7(8):e42665.
- Kole, M. H., Letzkus, J. J., and Stuart, G. J. (2007). Axon initial segment kv1 channels control axonal action potential waveform and synaptic efficacy. *Neuron*, 55(4):633–47.
- Kole, M. H. and Stuart, G. J. (2008). Is action potential threshold lowest in the axon? *Nat Neurosci*, 11(11):1253–5.
- Kole, M. H. and Stuart, G. J. (2012). Signal processing in the axon initial segment. *Neuron*, 73(2):235–47.
- Komada, M. and Soriano, P. (2002). [beta]iv-spectrin regulates sodium channel clustering through ankyrin-g at axon initial segments and nodes of ranvier. *J Cell Biol*, 156(2):337–48.
- Kordeli, E., Lambert, S., and Bennett, V. (1995). Ankyring. a new ankyrin gene with neural-specific isoforms localized at the axonal initial segment and node of ranvier. *Journal of Biological Chemistry*, 270:2352–2359.
- Kosfeld, M., Heinrichs, M., Zak, P. J., Fischbacher, U., and Fehr, E. (2005). Oxytocin increases trust in humans. *Nature*, 435(7042):673–6.
- Kuba, H., Adachi, R., and Ohmori, H. (2014). Activity-dependent and activity-independent development of the axon initial segment. *J Neurosci*, 34(9):3443–53.
- Kuba, H., Oichi, Y., and Ohmori, H. (2010). Presynaptic activity regulates na(+) channel distribution at the axon initial segment. *Nature*, 465(7301):1075–8.
- Kuba, H., Yamada, R., Ishiguro, G., and Adachi, R. (2015). Redistribution of kv1 and kv7 enhances neuronal excitability during structural axon initial segment plasticity. *Nat Commun*, 6:8815.
- Kumar, A., Rotter, S., and Aertsen, A. (2010). Spiking activity propagation in neu-

- ronal networks: reconciling different perspectives on neural coding. *Nat Rev Neurosci*, 11(9):615–27.
- Lasztocki, B. and Klausberger, T. (2014). Layer-specific gabaergic control of distinct gamma oscillations in the ca1 hippocampus. *Neuron*, 81(5):1126–1139.
- Lasztocki, B. and Klausberger, T. (2017). Distinct gamma oscillations in the distal dendritic fields of the dentate gyrus and the ca1 area of mouse hippocampus. *Brain Struct Funct*.
- Lawrence, J. J., Haario, H., and Stone, E. F. (2015). Presynaptic cholinergic neuromodulation alters the temporal dynamics of short-term depression at parvalbumin-positive basket cell synapses from juvenile ca1 mouse hippocampus. *J Neurophysiol*, 113(7):2408–19.
- Lee, A. K. and Wilson, M. A. (2002). Memory of sequential experience in the hippocampus during slow wave sleep. *Neuron*, 36(6):1183–94.
- Lee, I., Yoganarasimha, D., Rao, G., and Knierim, J. J. (2004). Comparison of population coherence of place cells in hippocampal subfields ca1 and ca3. *Nature*, 430(6998):456–9.
- Levey, A. I., Kitt, C. A., Simonds, W. F., Price, D. L., and Brann, M. R. (1991). Identification and localization of muscarinic acetylcholine receptor proteins in brain with subtype-specific antibodies. *J Neurosci*, 11(10):3218–26.
- Liu, X. B. and Jones, E. G. (1996). Localization of alpha type ii calcium calmodulin-dependent protein kinase at glutamatergic but not gamma-aminobutyric acid (gabaergic) synapses in thalamus and cerebral cortex. *Proc Natl Acad Sci U S A*, 93(14):7332–6.
- Lobner, D. and Lipton, P. (1993). Intracellular calcium levels and calcium fluxes in the ca1 region of the rat hippocampal slice during in vitro ischemia: relationship to electrophysiological cell damage. *J Neurosci*, 13(11):4861–71.
- London, M. and Hausser, M. (2005). Dendritic computation. *Annu Rev Neurosci*, 28:503–32.



- Lorente De Nó, R. (1938). Analysis of the activity of the chains of internuncial neurons. *Journal of Neurophysiology*, 1(3):207–244.
- Lorincz, A. and Nusser, Z. (2008). Cell-type-dependent molecular composition of the axon initial segment. *J Neurosci*, 28(53):14329–40.
- Lorincz, A. and Nusser, Z. (2010). Molecular identity of dendritic voltage-gated sodium channels. *Science*, 328(5980):906–9.
- Lowel, S. and Singer, W. (1992). Selection of intrinsic horizontal connections in the visual cortex by correlated neuronal activity. *Science*, 255(5041):209–12.
- Mack, S. O., Kc, P., Wu, M., Coleman, B. R., Tolentino-Silva, F. P., and Haxhiu, M. A. (2002). Paraventricular oxytocin neurons are involved in neural modulation of breathing. *J Appl Physiol (1985)*, 92(2):826–34.
- Maex, R. and De Schutter, E. (2007). Mechanism of spontaneous and self-sustained oscillations in networks connected through axo-axonal gap junctions. *Eur J Neurosci*, 25(11):3347–58.
- Magee, J. C. (2000). Dendritic integration of excitatory synaptic input. *Nat Rev Neurosci*, 1(3):181–90.
- Magee, J. C. and Cook, E. P. (2000). Somatic epsp amplitude is independent of synapse location in hippocampal pyramidal neurons. *Nat Neurosci*, 3(9):895–903.
- Magon, N. and Kalra, S. (2011). The orgasmic history of oxytocin: Love, lust, and labor. *Indian J Endocrinol Metab*, 15 Suppl 3:S156–61.
- Maier, N., Morris, G., Johenning, F. W., and Schmitz, D. (2009). An approach for reliably investigating hippocampal sharp wave-ripples in vitro. *PLoS One*, 4(9):e6925.
- Maier, N., Nimmrich, V., and Draguhn, A. (2003). Cellular and network mechanisms underlying spontaneous sharp wave-ripple complexes in mouse hippocampal slices. *J Physiol*, 550(Pt 3):873–87.

- Maier, P., Kaiser, M. E., Grinevich, V., Draguhn, A., and Both, M. (2016). Differential effects of oxytocin on mouse hippocampal oscillations in vitro. *Eur J Neurosci*, 44(11):2885–2898.
- Markram, H., Lubke, J., Frotscher, M., and Sakmann, B. (1997). Regulation of synaptic efficacy by coincidence of postsynaptic epsps and epsps. *Science*, 275(5297):213–5.
- Marlin, B. J. and Froemke, R. C. (2017). Oxytocin modulation of neural circuits for social behavior. *Dev Neurobiol*, 77(2):169–189.
- Martina, M., Vida, I., and Jonas, P. (2000). Distal initiation and active propagation of action potentials in interneuron dendrites. *Science*, 287(5451):295–300.
- Matsuzaki, M., Honkura, N., Ellis-Davies, G. C., and Kasai, H. (2004). Structural basis of long-term potentiation in single dendritic spines. *Nature*, 429(6993):761–6.
- Meeks, J. P. and Mennerick, S. (2007). Action potential initiation and propagation in ca3 pyramidal axons. *J Neurophysiol*, 97(5):3460–72.
- Memmesheimer, R. M. (2010). Quantitative prediction of intermittent high-frequency oscillations in neural networks with supralinear dendritic interactions. *Proc Natl Acad Sci U S A*, 107(24):11092–7.
- Memmesheimer, R. M. and Timme, M. (2012). Non-additive coupling enables propagation of synchronous spiking activity in purely random networks. *PLoS Comput Biol*, 8(4):e1002384.
- Meziane, H., Dodart, J. C., Mathis, C., Little, S., Clemens, J., Paul, S. M., and Ungerer, A. (1998). Memory-enhancing effects of secreted forms of the beta-amyloid precursor protein in normal and amnesic mice. *Proc Natl Acad Sci U S A*, 95(21):12683–8.
- Mitre, M., Marlin, B. J., Schiavo, J. K., Morina, E., Norden, S. E., Hackett, T. A., Aoki, C. J., Chao, M. V., and Froemke, R. C. (2016). A distributed network for social cognition enriched for oxytocin receptors. *J Neurosci*, 36(8):2517–35.

- Mizumori, S. J., Perez, G. M., Alvarado, M. C., Barnes, C. A., and McNaughton, B. L. (1990). Reversible inactivation of the medial septum differentially affects two forms of learning in rats. *Brain Res*, 528(1):12–20.
- Montgomery, S. M. and Buzsaki, G. (2007). Gamma oscillations dynamically couple hippocampal ca3 and ca1 regions during memory task performance. *Proc Natl Acad Sci U S A*, 104(36):14495–500.
- Muhlethaler, M., Charpak, S., and Dreifuss, J. J. (1984). Contrasting effects of neurohypophysial peptides on pyramidal and non-pyramidal neurones in the rat hippocampus. *Brain Res*, 308(1):97–107.
- Murphy, M. P. and LeVine, H., r. (2010). Alzheimer’s disease and the amyloid-beta peptide. *J Alzheimers Dis*, 19(1):311–23.
- Nagel, G., Brauner, M., Liewald, J. F., Adeishvili, N., Bamberg, E., and Gottschalk, A. (2005). Light activation of channelrhodopsin-2 in excitable cells of caenorhabditis elegans triggers rapid behavioral responses. *Curr Biol*, 15(24):2279–84.
- Nagel, G., Szellas, T., Huhn, W., Kateriya, S., Adeishvili, N., Berthold, P., Ollig, D., Hegemann, P., and Bamberg, E. (2003). Channelrhodopsin-2, a directly light-gated cation-selective membrane channel. *Proc Natl Acad Sci U S A*, 100(24):13940–5.
- Nakajima, Y., Nakajima, S., Leonard, R. J., and Yamaguchi, K. (1986). Acetylcholine raises excitability by inhibiting the fast transient potassium current in cultured hippocampal neurons. *Proc Natl Acad Sci U S A*, 83(9):3022–6.
- Neff, J., Athale, R., and Lee, S. (1990). Two-dimensional spatial light modulators: a tutorial. *Proceedings of the IEEE*, 78(5).
- Nevian, T., Larkum, M. E., Polsky, A., and Schiller, J. (2007). Properties of basal dendrites of layer 5 pyramidal neurons: a direct patch-clamp recording study. *Nat Neurosci*, 10(2):206–14.

- Nicolas, M. and Hassan, B. A. (2014). Amyloid precursor protein and neural development. *Development*, 141(13):2543–8.
- Nimmrich, V., Maier, N., Schmitz, D., and Draguhn, A. (2005). Induced sharp wave-ripple complexes in the absence of synaptic inhibition in mouse hippocampal slices. *J Physiol*, 563(Pt 3):663–70.
- Obregon, D., Hou, H., Deng, J., Giunta, B., Tian, J., Darlington, D., Shahaduzzaman, M., Zhu, Y., Mori, T., Mattson, M. P., and Tan, J. (2012). Soluble amyloid precursor protein- $\alpha$  modulates beta-secretase activity and amyloid- $\beta$  generation. *Nat Commun*, 3:777.
- O’Brien, R. J. and Wong, P. C. (2011). Amyloid precursor protein processing and alzheimer’s disease. *Annu Rev Neurosci*, 34:185–204.
- Ogawa, Y. and Rasband, M. N. (2008). The functional organization and assembly of the axon initial segment. *Curr Opin Neurobiol*, 18(3):307–13.
- O’Keefe, J. (1976). Place units in the hippocampus of the freely moving rat. *Exp Neurol*, 51(1):78–109.
- O’Keefe, J. and Dostrovsky, J. (1971). The hippocampus as a spatial map. preliminary evidence from unit activity in the freely-moving rat. *Brain Res*, 34(1):171–5.
- O’Keefe, J. and Nadel, L. (1978). The hippocampus as a cognitive map. *Oxford University Press*.
- O’Keefe, J. and Recce, M. L. (1993). Phase relationship between hippocampal place units and the eeg theta rhythm. *Hippocampus*, 3(3):317–30.
- Oliva, A., Fernandez-Ruiz, A., Buzsaki, G., and Berenyi, A. (2016). Role of hippocampal ca2 region in triggering sharp-wave ripples. *Neuron*, 91(6):1342–1355.
- Ovsepian, S. V. (2006). Enhancement of the synchronized firing of ca1 pyramidal cells by

- medial septum preconditioning: time-dependent involvement of muscarinic cholinergic receptors and gabab receptors. *Neurosci Lett*, 393(1):1–6.
- Owen, S. F., Tuncdemir, S. N., Bader, P. L., Tirko, N. N., Fishell, G., and Tsien, R. W. (2013). Oxytocin enhances hippocampal spike transmission by modulating fast-spiking interneurons. *Nature*, 500(7463):458–62.
- Palmer, L. M. and Stuart, G. J. (2006). Site of action potential initiation in layer 5 pyramidal neurons. *J Neurosci*, 26(6):1854–63.
- Papagiakoumou, E., Anselmi, F., Begue, A., de Sars, V., Gluckstad, J., Isacoff, E. Y., and Emiliani, V. (2010). Scanless two-photon excitation of channelrhodopsin-2. *Nat Methods*, 7(10):848–54.
- Pastoll, H., Solanka, L., van Rossum, M. C., and Nolan, M. F. (2013). Feedback inhibition enables theta-nested gamma oscillations and grid firing fields. *Neuron*, 77(1):141–54.
- Pavlidis, C. and Winson, J. (1989). Influences of hippocampal place cell firing in the awake state on the activity of these cells during subsequent sleep episodes. *J Neurosci*, 9(8):2907–18.
- Pedersen, C. A., Gibson, C. M., Rau, S. W., Salimi, K., Smedley, K. L., Casey, R. L., Leserman, J., Jarskog, L. F., and Penn, D. L. (2011). Intranasal oxytocin reduces psychotic symptoms and improves theory of mind and social perception in schizophrenia. *Schizophr Res*, 132(1):50–3.
- Pernice, V., Deger, M., Cardanobile, S., and Rotter, S. (2013). The relevance of network micro-structure for neural dynamics. *Front Comput Neurosci*, 7:72.
- Peters, A., Proskauer, C. C., and Kaiserman-Abramof, I. R. (1968). The small pyramidal neuron of the rat cerebral cortex. the axon hillock and initial segment. *J Cell Biol*, 39(3):604–19.
- Pfeiffer, T., Draguhn, A., Reichinnek, S., and Both, M. (2014). Optimized temporally

- deconvolved  $ca(2)(+)$  imaging allows identification of spatiotemporal activity patterns of  $ca1$  hippocampal ensembles. *Neuroimage*, 94:239–49.
- Plummer, S., Van den Heuvel, C., Thornton, E., Corrigan, F., and Cappai, R. (2016). The neuroprotective properties of the amyloid precursor protein following traumatic brain injury. *Aging Dis*, 7(2):163–79.
- Priebe, N. J. and Ferster, D. (2005). Direction selectivity of excitation and inhibition in simple cells of the cat primary visual cortex. *Neuron*, 45(1):133–45.
- Prince, M., Wimo, A., Guerchet, M., Gemma-Claire, A., Wu, Y.-T., and Prina, M. (2015). The world alzheimer report 2015: The global impact of dementia-an analysis of prevalence, incidence, cost and trends. *London: Alzheimer's Disease International*.
- Raam, T., McAvoy, K. M., Besnard, A., Veenema, A., and Sahay, A. (2017). Hippocampal oxytocin receptors are necessary for discrimination of social stimuli. *Nat Commun*, 8(1):2001.
- Racz, A., Ponomarenko, A. A., Fuchs, E. C., and Monyer, H. (2009). Augmented hippocampal ripple oscillations in mice with reduced fast excitation onto parvalbumin-positive cells. *J Neurosci*, 29(8):2563–8.
- Ramadan, W., Eschenko, O., and Sara, S. J. (2009). Hippocampal sharp wave/ripples during sleep for consolidation of associative memory. *PLoS One*, 4(8):e6697.
- Rash, J. A., Aguirre-Camacho, A., and Campbell, T. S. (2014). Oxytocin and pain: a systematic review and synthesis of findings. *Clin J Pain*, 30(5):453–62.
- Reichinnek, S., von Kameke, A., Hagenston, A. M., Freitag, E., Roth, F. C., Bading, H., Hasan, M. T., Draguhn, A., and Both, M. (2012). Reliable optical detection of coherent neuronal activity in fast oscillating networks in vitro. *Neuroimage*, 60(1):139–52.
- Ring, S., Weyer, S. W., Kilian, S. B., Waldron, E., Pietrzik, C. U., Filippov, M. A., Herms, J., Buchholz, C., Eckman, C. B., Korte, M., Wolfer, D. P., and Muller, U. C. (2007). The secreted beta-amyloid precursor protein ectodomain  $app_{s\alpha}$  is sufficient to rescue the

- anatomical, behavioral, and electrophysiological abnormalities of app-deficient mice. *J Neurosci*, 27(29):7817–26.
- Risher, W. C., Ard, D., Yuan, J., and Kirov, S. A. (2010). Recurrent spontaneous spreading depolarizations facilitate acute dendritic injury in the ischemic penumbra. *J Neurosci*, 30(29):9859–68.
- Robinson, H. P. and Kawai, N. (1993). Injection of digitally synthesized synaptic conductance transients to measure the integrative properties of neurons. *J Neurosci Methods*, 49(3):157–65.
- Rolls, E. T. (1996). A theory of hippocampal function in memory. *Hippocampus*, 6(6):601–20.
- Rolls, E. T. (2013). The mechanisms for pattern completion and pattern separation in the hippocampus. *Front Syst Neurosci*, 7:74.
- Ross, H. E. and Young, L. J. (2009). Oxytocin and the neural mechanisms regulating social cognition and affiliative behavior. *Front Neuroendocrinol*, 30(4):534–47.
- Salinas, E. and Sejnowski, T. J. (2001). Correlated neuronal activity and the flow of neural information. *Nat Rev Neurosci*, 2(8):539–50.
- Schiller, J., Major, G., Koester, H. J., and Schiller, Y. (2000). Nmda spikes in basal dendrites of cortical pyramidal neurons. *Nature*, 404(6775):285–9.
- Schlingloff, D., Kali, S., Freund, T. F., Hajos, N., and Gulyas, A. I. (2014). Mechanisms of sharp wave initiation and ripple generation. *J Neurosci*, 34(34):11385–98.
- Schmidt-Hieber, C. and Bischofberger, J. (2010). Fast sodium channel gating supports localized and efficient axonal action potential initiation. *J Neurosci*, 30(30):10233–42.
- Schmidt-Hieber, C., Jonas, P., and Bischofberger, J. (2008). Action potential initiation and propagation in hippocampal mossy fibre axons. *J Physiol*, 586(7):1849–57.
- Schmitz, D., Schuchmann, S., Fisahn, A., Draguhn, A., Buhl, E. H., Petrasch-Parwez, E.,

- Dermietzel, R., Heinemann, U., and Traub, R. D. (2001). Axo-axonal coupling. a novel mechanism for ultrafast neuronal communication. *Neuron*, 31(5):831–40.
- Schomburg, E. W., Fernandez-Ruiz, A., Mizuseki, K., Berenyi, A., Anastassiou, C. A., Koch, C., and Buzsaki, G. (2014). Theta phase segregation of input-specific gamma patterns in entorhinal-hippocampal networks. *Neuron*, 84(2):470–85.
- Schonberger, J., Draguhn, A., and Both, M. (2014). Lamina-specific contribution of glutamatergic and gabaergic potentials to hippocampal sharp wave-ripple complexes. *Front Neural Circuits*, 8:103.
- Scott, L., Feng, J., Kiss, T., Needle, E., Atchison, K., Kawabe, T. T., Milici, A. J., Hajos-Korcsok, E., Riddell, D., and Hajos, M. (2012). Age-dependent disruption in hippocampal theta oscillation in amyloid-beta overproducing transgenic mice. *Neurobiol Aging*, 33(7):1481 e13–23.
- Sharp, A. A., O’Neil, M. B., Abbott, L. F., and Marder, E. (1993). Dynamic clamp: computer-generated conductances in real neurons. *J Neurophysiol*, 69(3):992–5.
- Shu, Y., Yu, Y., Yang, J., and McCormick, D. A. (2007). Selective control of cortical axonal spikes by a slowly inactivating  $k^+$  current. *Proc Natl Acad Sci U S A*, 104(27):11453–8.
- Siapas, A. G. and Wilson, M. A. (1998). Coordinated interactions between hippocampal ripples and cortical spindles during slow-wave sleep. *Neuron*, 21(5):1123–8.
- Skaggs, W. E., McNaughton, B. L., Wilson, M. A., and Barnes, C. A. (1996). Theta phase precession in hippocampal neuronal populations and the compression of temporal sequences. *Hippocampus*, 6(2):149–72.
- Smith-Swintosky, V. L., Pettigrew, L. C., Craddock, S. D., Culwell, A. R., Rydel, R. E., and Mattson, M. P. (1994). Secreted forms of beta-amyloid precursor protein protect against ischemic brain injury. *J Neurochem*, 63(2):781–4.
- Somjen, G. G. (2001). Mechanisms of spreading depression and hypoxic spreading depression-like depolarization. *Physiol Rev*, 81(3):1065–96.



- Somogyi, P., Katona, L., Klausberger, T., Lasztozci, B., and Viney, T. J. (2014). Temporal redistribution of inhibition over neuronal subcellular domains underlies state-dependent rhythmic change of excitability in the hippocampus. *Philos Trans R Soc Lond B Biol Sci*, 369(1635):20120518.
- Song, S., Sjöström, P. J., Reigl, M., Nelson, S., and Chklovskii, D. B. (2005). Highly non-random features of synaptic connectivity in local cortical circuits. *PLoS Biol*, 3(3):e68.
- Spoljaric, A., Seja, P., Spoljaric, I., Virtanen, M. A., Lindfors, J., Uvarov, P., Summanen, M., Crow, A. K., Hsueh, B., Puskarjov, M., Ruusuvuori, E., Voipio, J., Deisseroth, K., and Kaila, K. (2017). Vasopressin excites interneurons to suppress hippocampal network activity across a broad span of brain maturity at birth. *Proc Natl Acad Sci U S A*, 114(50):E10819–E10828.
- Squire, L. R. (1992). Memory and the hippocampus: a synthesis from findings with rats, monkeys, and humans. *Psychol Rev*, 99(2):195–231.
- Squire, L. R., Stark, C. E., and Clark, R. E. (2004). The medial temporal lobe. *Annu Rev Neurosci*, 27:279–306.
- Stark, E., Roux, L., Eichler, R., Senzai, Y., Royer, S., and Buzsáki, G. (2014). Pyramidal cell-interneuron interactions underlie hippocampal ripple oscillations. *Neuron*, 83(2):467–80.
- Sullivan, D., Csicsvari, J., Mizuseki, K., Montgomery, S., Diba, K., and Buzsáki, G. (2011). Relationships between hippocampal sharp waves, ripples, and fast gamma oscillation: influence of dentate and entorhinal cortical activity. *J Neurosci*, 31(23):8605–16.
- Sun, Y., Nguyen, A. Q., Nguyen, J. P., Le, L., Saur, D., Choi, J., Callaway, E. M., and Xu, X. (2014). Cell-type-specific circuit connectivity of hippocampal ca1 revealed through cre-dependent rabies tracing. *Cell Rep*, 7(1):269–80.
- Swanson, L. W. and Kuypers, H. G. (1980). The paraventricular nucleus of the hypothalamus: cytoarchitectonic subdivisions and organization of projections to the pituitary,

- dorsal vagal complex, and spinal cord as demonstrated by retrograde fluorescence double-labeling methods. *J Comp Neurol*, 194(3):555–70.
- Swanson, L. W. and Sawchenko, P. E. (1983). Hypothalamic integration: organization of the paraventricular and supraoptic nuclei. *Annu Rev Neurosci*, 6:269–324.
- Swanson, L. W., Wyss, J. M., and Cowan, W. M. (1978). An autoradiographic study of the organization of intrahippocampal association pathways in the rat. *J Comp Neurol*, 181(4):681–715.
- Taxidis, J., Coombes, S., Mason, R., and Owen, M. R. (2012). Modeling sharp wave-ripple complexes through a ca3-ca1 network model with chemical synapses. *Hippocampus*, 22(5):995–1017.
- Thibault, O., Gant, J. C., and Landfield, P. W. (2007). Expansion of the calcium hypothesis of brain aging and alzheimer’s disease: minding the store. *Aging Cell*, 6(3):307–17.
- Thome, C., Kelly, T., Yanez, A., Schultz, C., Engelhardt, M., Cambridge, S. B., Both, M., Draguhn, A., Beck, H., and Egorov, A. V. (2014). Axon-carrying dendrites convey privileged synaptic input in hippocampal neurons. *Neuron*, 83(6):1418–30.
- Thornton, E., Vink, R., Blumbergs, P. C., and Van Den Heuvel, C. (2006). Soluble amyloid precursor protein alpha reduces neuronal injury and improves functional outcome following diffuse traumatic brain injury in rats. *Brain Res*, 1094(1):38–46.
- Tomizawa, K., Iga, N., Lu, Y. F., Moriwaki, A., Matsushita, M., Li, S. T., Miyamoto, O., Itano, T., and Matsui, H. (2003). Oxytocin improves long-lasting spatial memory during motherhood through map kinase cascade. *Nat Neurosci*, 6(4):384–90.
- Traub, R. D. and Bibbig, A. (2000). A model of high-frequency ripples in the hippocampus based on synaptic coupling plus axon-axon gap junctions between pyramidal neurons. *J Neurosci*, 20(6):2086–93.
- Traub, R. D., Jefferys, J. G., Miles, R., Whittington, M. A., and Toth, K. (1994). A

- branching dendritic model of a rodent ca3 pyramidal neurone. *J Physiol*, 481 ( Pt 1):79–95.
- Traub, R. D., Schmitz, D., Jefferys, J. G., and Draguhn, A. (1999). High-frequency population oscillations are predicted to occur in hippocampal pyramidal neuronal networks interconnected by axoaxonal gap junctions. *Neuroscience*, 92(2):407–26.
- Traub, R. D., Schmitz, D., Maier, N., Whittington, M. A., and Draguhn, A. (2012). Axonal properties determine somatic firing in a model of in vitro ca1 hippocampal sharp wave/ripples and persistent gamma oscillations. *Eur J Neurosci*, 36(5):2650–60.
- Traub, R. D., Whittington, M. A., Colling, S. B., Buzsaki, G., and Jefferys, J. G. (1996). Analysis of gamma rhythms in the rat hippocampus in vitro and in vivo. *J Physiol*, 493 ( Pt 2):471–84.
- Tsien, R. Y. (1981). A non-disruptive technique for loading calcium buffers and indicators into cells. *Nature*, 290(5806):527–8.
- Valero, M., Averkin, R. G., Fernandez-Lamo, I., Aguilar, J., Lopez-Pigozzi, D., Brotons-Mas, J. R., Cid, E., Tamas, G., and Menendez de la Prida, L. (2017). Mechanisms for selective single-cell reactivation during offline sharp-wave ripples and their distortion by fast ripples. *Neuron*, 94(6):1234–1247 e7.
- Valero, M., Cid, E., Averkin, R. G., Aguilar, J., Sanchez-Aguilera, A., Viney, T. J., Gomez-Dominguez, D., Bellistri, E., and de la Prida, L. M. (2015). Determinants of different deep and superficial ca1 pyramidal cell dynamics during sharp-wave ripples. *Nat Neurosci*, 18(9):1281–90.
- Vandecasteele, M., Varga, V., Berenyi, A., Papp, E., Bartho, P., Venance, L., Freund, T. F., and Buzsaki, G. (2014). Optogenetic activation of septal cholinergic neurons suppresses sharp wave ripples and enhances theta oscillations in the hippocampus. *Proc Natl Acad Sci U S A*, 111(37):13535–40.

- Vanderwolf, C. H. (1969). Hippocampal electrical activity and voluntary movement in the rat. *Electroencephalogr Clin Neurophysiol*, 26(4):407–18.
- Vandesande, F., Dierickx, K., and De Mey, J. (1977). The origin of the vasopressinergic and oxytocinergic fibres of the external region of the median eminence of the rat hypophysis. *Cell Tissue Res*, 180(4):443–52.
- Varga, C., Golshani, P., and Soltesz, I. (2012). Frequency-invariant temporal ordering of interneuronal discharges during hippocampal oscillations in awake mice. *Proc Natl Acad Sci U S A*, 109(40):E2726–34.
- Varga, C., Oijala, M., Lish, J., Szabo, G. G., Bezaire, M., Marchionni, I., Golshani, P., and Soltesz, I. (2014). Functional fission of parvalbumin interneuron classes during fast network events. *Elife*, 3.
- Viereckel, T., Kostic, M., Bahner, F., Draguhn, A., and Both, M. (2013). Effects of the gaba-uptake blocker nnc-711 on spontaneous sharp wave-ripple complexes in mouse hippocampal slices. *Hippocampus*, 23(5):323–9.
- Volpicelli, L. A. and Levey, A. I. (2004). Muscarinic acetylcholine receptor subtypes in cerebral cortex and hippocampus. *Prog Brain Res*, 145:59–66.
- Walz, H., Grewe, J., and Benda, J. (2014). Static frequency tuning accounts for changes in neural synchrony evoked by transient communication signals. *J Neurophysiol*, 112(4):752–65.
- Wang, L. Y., Gan, L., Forsythe, I. D., and Kaczmarek, L. K. (1998). Contribution of the kv3.1 potassium channel to high-frequency firing in mouse auditory neurones. *J Physiol*, 509 ( Pt 1):183–94.
- Wang, X., Zhang, C., Szabo, G., and Sun, Q. Q. (2013). Distribution of camkii $\alpha$  expression in the brain in vivo, studied by camkii $\alpha$ -gfp mice. *Brain Res*, 1518:9–25.
- Wang, Y., Romani, S., Lustig, B., Leonardo, A., and Pastalkova, E. (2015). Theta se-

- quences are essential for internally generated hippocampal firing fields. *Nat Neurosci*, 18(2):282–8.
- Webster, N. J., Ramsden, M., Boyle, J. P., Pearson, H. A., and Peers, C. (2006). Amyloid peptides mediate hypoxic increase of l-type  $ca^{2+}$  channels in central neurones. *Neurobiol Aging*, 27(3):439–45.
- Whittington, M. A., Cunningham, M. O., LeBeau, F. E., Racca, C., and Traub, R. D. (2011). Multiple origins of the cortical gamma rhythm. *Dev Neurobiol*, 71(1):92–106.
- Whittington, M. A., Traub, R. D., and Jefferys, J. G. (1995). Synchronized oscillations in interneuron networks driven by metabotropic glutamate receptor activation. *Nature*, 373(6515):612–5.
- Wilson, M. A. and McNaughton, B. L. (1994). Reactivation of hippocampal ensemble memories during sleep. *Science*, 265(5172):676–9.
- Witter, M. P. (1993). Organization of the entorhinal-hippocampal system: a review of current anatomical data. *Hippocampus*, 3 Spec No:33–44.
- Witter, M. P., Wouterlood, F. G., Naber, P. A., and Van Haeften, T. (2000). Anatomical organization of the parahippocampal-hippocampal network. *Ann N Y Acad Sci*, 911:1–24.
- Womelsdorf, T., Schoffelen, J. M., Oostenveld, R., Singer, W., Desimone, R., Engel, A. K., and Fries, P. (2007). Modulation of neuronal interactions through neuronal synchronization. *Science*, 316(5831):1609–12.
- Xia, N. S., Luo, W. X., Zhang, J., Xie, X. Y., Yang, H. J., Li, S. W., Chen, M., and Ng, M. H. (2002). Bioluminescence of *aequorea macrodactyla*, a common jellyfish species in the east china sea. *Mar Biotechnol (NY)*, 4(2):155–62.
- Xiao, L., Priest, M. F., Nasenbeny, J., Lu, T., and Kozorovitskiy, Y. (2017). Biased oxytocinergic modulation of midbrain dopamine systems. *Neuron*, 95(2):368–384 e5.

- Yang, L., Wang, Z., Wang, B., Justice, N. J., and Zheng, H. (2009). Amyloid precursor protein regulates cav1.2 l-type calcium channel levels and function to influence gabaergic short-term plasticity. *J Neurosci*, 29(50):15660–8.
- Yang, Y., Ogawa, Y., Hedstrom, K. L., and Rasband, M. N. (2007). betaiv spectrin is recruited to axon initial segments and nodes of ranvier by ankyring. *J Cell Biol*, 176(4):509–19.
- Yartsev, M. M. and Ulanovsky, N. (2013). Representation of three-dimensional space in the hippocampus of flying bats. *Science*, 340(6130):367–72.
- Yi, F., DeCan, E., Stoll, K., Marceau, E., Deisseroth, K., and Lawrence, J. J. (2015). Muscarinic excitation of parvalbumin-positive interneurons contributes to the severity of pilocarpine-induced seizures. *Epilepsia*, 56(2):297–309.
- Ylinen, A., Bragin, A., Nadasdy, Z., Jando, G., Szabo, I., Sik, A., and Buzsaki, G. (1995). Sharp wave-associated high-frequency oscillation (200 hz) in the intact hippocampus: network and intracellular mechanisms. *J Neurosci*, 15(1 Pt 1):30–46.
- Yoder, R. M. and Pang, K. C. (2005). Involvement of gabaergic and cholinergic medial septal neurons in hippocampal theta rhythm. *Hippocampus*, 15(3):381–92.
- Yoshida, M., Takayanagi, Y., Inoue, K., Kimura, T., Young, L. J., Onaka, T., and Nishimori, K. (2009). Evidence that oxytocin exerts anxiolytic effects via oxytocin receptor expressed in serotonergic neurons in mice. *J Neurosci*, 29(7):2259–71.
- Zhang, C., Shen, W., and Zhang, G. (2002). N-methyl-d-aspartate receptor and l-type voltage-gated ca(2+) channel antagonists suppress the release of cytochrome c and the expression of procaspase-3 in rat hippocampus after global brain ischemia. *Neurosci Lett*, 328(3):265–8.
- Zhang, X. and Le, W. (2010). Pathological role of hypoxia in alzheimer’s disease. *Exp Neurol*, 223(2):299–303.

Zhang, Z., Zheng, Y., and Daping, C. (2014). Fundamentals of phase-only liquid crystal on silicon (lcos) devices. *Light: Science and Applications*, (3).

Zhu, Y., Stornetta, R. L., and Zhu, J. J. (2004). Chandelier cells control excessive cortical excitation: characteristics of whisker-evoked synaptic responses of layer 2/3 nonpyramidal and pyramidal neurons. *J Neurosci*, 24(22):5101–8.





# List of Publications

- Hefter, D., **Kaiser, M.**, Weyer, SW., Papageorgiou, IE., Both, M., Kann O., Müller, UC., and Draguhn, A. (2016). Amyloid Precursor Protein Protects Neuronal Network Function after Hypoxia via Control of Voltage-Gated Calcium Channels. *J Neurosci*, 36(32):8356-71.
- Maier, P.\*, **Kaiser, M. E.\***, Grinevich, V., Draguhn, A., Both, M. (2016). Differential effects of oxytocin on mouse hippocampal oscillations in vitro. *Eur Journal of Neurosci*, 44(11):2885-2898. \*contributed equally
- Geschwill, P.\*, **Kaiser, M. E.\***, Draguhn, A., and Both, M. (2018). Cellular and Network Mechanisms Underlying the Switch of Hippocampal Oscillatory States. *Submitted and under review*. \*contributed equally
- **Kaiser, M. E.**, Geschwill, P., Thome, C., Engelhardt, M., Sackmann, T., Zuber, N., Schulz, C., Draguhn, A., and Both, M. (2018). Privileged Recruitment of Axon-Carrying Dendrite Cells into Hippocampal Sharp Wave-Ripple Oscillations. *In preparation*